Volume 7, Number 1, Winter 2021

ACERP
Advanced Ceramics Progress

ISSN 2423-7477
e-ISSN 2423-7485

Advanced Ceramics Progress

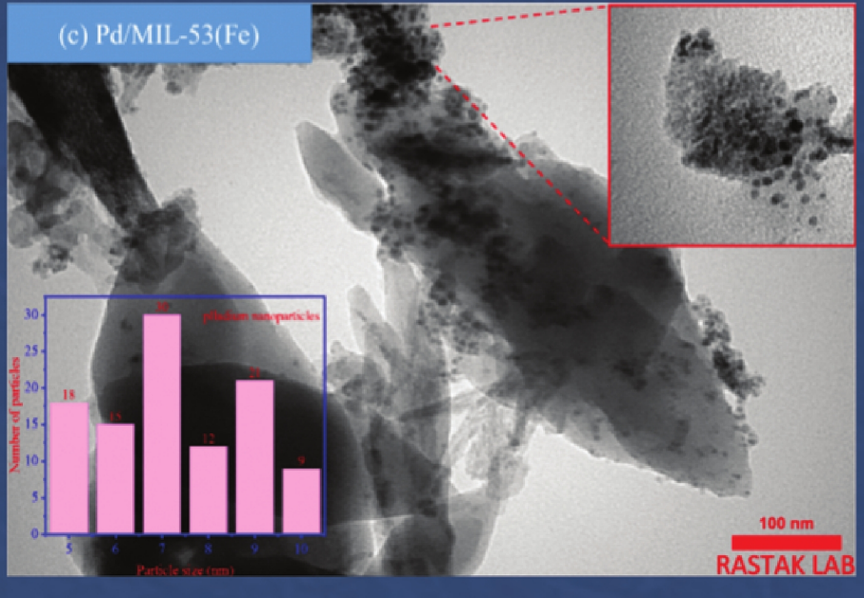

Materials and Energy
Research Center

Iranian Ceramic Society

In The name of God

Advanced Ceramics Progress

DISCLAIMER

The publication of articles in Advanced Ceramics Progress does not imply that the editorial board, editorial advisory board, reviewers or the publisher accept, approve or endorse the data and conclusions of authors.

Advanced **Cer**amics **P**rogress (ISSN 2423-7477) (e-ISSN 2423-7485)
Web Site: www.acerp.ir, E-mail: office@acerp.ir
Tel: +98 (0) 26 36280040-7 ext.: 382, Fax: +98 (0) 26 36201888
Tel:+98 (0)21 88771626-7 ext.: 8931, Fax: +98 (0)21 88773352
Materials and Energy Research Center (MERC); Iranian Ceramic Society (ICERS)

ISSN: 2423-7477; e-ISSN: 2423-7485

Advanced Ceramics Progress: Vol. 7, No. 1, (Winter 2021) 1-51

CONTENTS

P. Kameli **H. Vaezi** **M. H. Ehsani** **Bagher Aslibeiki** **H. Salamati**	Structual, Magnetic, and Transport Properties of $LaMn_{1-x}Cu_xO_3$ (x= 0-0.125) Ceramics	1-10
B. Chameh **M. Moradi Alborzi** **S. Hajati** **F. Alikhani Hessari** **M. A. Kiani**	Synthesis and Characterization of Palladium Impregnated MIL-53(Fe) as Cathode Material of Supercapacitor	11-17
S. Hamidi **M. R. Rahimipour** **M. J. Eshraghi** **H. Esfahani**	Optimization of Heat Treatment Cycles in Sub-atmospheric LiF-NaF-KF Based Fluoride Ion Cleaning for Removing Oxide Layers in Cracks of IN738-LC	18-24
S. Manafi **A. Azizi**	Experimental and Numerical Evaluation of Diffusion Welding of 7075 Aluminum and AZ31 Magnesium Alloys	25-34
J. Arasteh	Microhardness Optimization of Al–TiC Nanocomposite Produced by Mechanical Milling and Heat Treatment	35-45
A. Khiabani **Z. S. Seyedraoufi** **M. Heydarzadeh Sohi**	Heat Treatment of Pulsed Electroplated Nickel Deposited on AA2024 Aluminum	46-51

Advanced Ceramics Progress

Research Article

Journal Homepage: www.acerp.ir

Structual, Magnetic, and Transport Properties of $LaMn_{1-x}Cu_xO_3$ (x= 0-0.125) Ceramics

P. Kameli [a], H. Vaezi [a], M. H. Ehsani [b] *, B. Aslibeiki [c], H. Salamati [a]

[a] *Department of Physics, Isfahan University of Technology, Isfahan, Isfahan, Iran*
[b] *Department of Physics, Semnan University, Semnan, Semnan, Iran*
[c] *Department of Physics, University of Tabriz, Tabriz, East Azerbaijan, Iran*

ARTICLE INFO

Article History:

Received 13 September 2020
Received in revised form 9 November 2020
Accepted 21 November 2020

Keywords:

Manganite Oxides
Doping
Spin Glass
Small Polaron Hopping

ABSTRACT

The present study investigates the structural, magnetic, and electrical properties of non-stoichiometric $LaMn_{1-x}Cu_xO_3$ (x= 0, 0.025, 0.05, 0.075, and 0.125) ceramics. The results of X-ray diffraction refinement indicated that all samples were crystallized in an orthorhombic structure and no apparent crystal structure change was introduced by doping Cu up to x=0.125. The Ferromagnetic (FM) nature revealed by non-stoichiometric $LaMn_{1-x}Cu_xO_{3-\delta}$ was verified through the appearance of Paramagnetic-Ferromagnetic (PM-FM) transition temperatures in AC magnetic susceptibility measurement of the samples. Due to the coexistence of Antiferromagnetic (AFM) and FM phases, all samples contained Re-entrant Spin Glass (RSG) and Cluster Spin Glass (CSG) states. The results showed that FM phase was comparable or even dominant in the doped samples up to x=0.075; however, after doping, AFM phase overcame the FM phase as a result of reduction of double exchange interaction. Temperature dependence of resistivity measurement indicated that upon increasing the Cu-doping level, resistivity decreased, except for the x=0.125 sample, and that metal-insulator transition at low temperatures was detected in the doped samples. Furthermore, changing the magnetic phase in the case of x=0.125 sample from FM (in x=0.075) to AFM dominant phase was accompanied by changing the transport parameters obtained from small polaron hopping models.

https://doi.org/10.30501/acp.2021.233610.1044

1. INTRODUCTION

Doped manganites $RMnO_3$ (R=rare-earth) with perovskite structures and a variety of magnetic and electrical behaviors have considerably attracted the attention of a number of researchers due to their remarkable coupling among freedom degrees of spin, charge, and orbit [1]. Manganese compounds can be applied in magnetic memory devices, sensors, refrigeration, medicine, biology, and photocatalytic activities [1-3].

Among these compounds, stoichiometric $LaMnO_3$ (LMO-$La^{3+}Mn^{3+}O^{2-}{}_3$) is an A-type Antiferromagnetic (AFM) insulator below the Néel temperature (T_N) of 140 K and the Mn^{3+} ions are coupled through a Super-Exchange (SE) interaction [4,5]. Besides the ABO_3-type perovskites, Manganese compounds of composition $AMnO_3$ (Manganite) can be applied in magnetic memory devices, sensors, refrigeration, medicine, biology, and photocatalytic [4-6].

When a divalent A^{2+} ion such as (A= Sr, Ca,) is substituted for La^{3+} in $La_{1-x}A_xMnO_3$ (LAMO), the Mn^{3+}/ Mn^{4+} ratio changes. This mixed-valence of Mn ion allows an electron to hop between them and produce a Ferromagnetic (FM) Double-Exchange (DE) interaction, which also promotes metallic electrical conduction with different compositions, x, [6-8]. The complicated and fascinating magnetic, electrical, and structural properties of LAMO were attributed to strong coupling among spin,

* Corresponding Author Email: ehsani@semnan.ac.ir (M. H. Ehsani)

URL: http://www.acerp.ir/article_127889.html

Please cite this article as: Kameli, P., Vaezi, H., Ehsani, M. H., Aslibeiki, B., Salamati, H., "Structural, Magnetic and Transport Properties of $LaMn_{1-x}O_3$ (x=0-0.125) Ceramics", ***Advanced Ceramics Progress***, Vol. 7, No. 1, (2021), 1-10. https://doi.org/10.30501/acp.2021.233610.1044

charge, orbital degrees of freedom, and lattice vibrations which were mainly explained by DE, Jahn-Teller (JT) distortion, and electron-phonon interactions. Besides the DE mechanism describing the interaction of Mn^{3+} and Mn^{4+} neighboring ions, JT distortion and electron-phonon interactions, phase separation, Griffiths phase, charge, and orbital ordering and their competitions, small polaron, and magnon correlated transport were employed to explain different properties of manganites [4-13]. As a result of a change in two effective parameters, i.e., Mn^{3+}/Mn^{4+} ratio and angle/width of Mn-O-Mn bonds, in A-site doping, interesting magnetic and electrical properties are observed [14-21].

In addition to this kind of doping, the Mn-site doping with magnetic or nonmagnetic ions also offers numerous attractive properties for manganites. Experimental studies on B-site doping in stoichiometric polycrystalline $LaMn_{1-x}B_xO_3$ (LMBO) compound by magnetic cations (B= Fe, Co, Ni, Cr, …) and nonmagnetic cations (B=Zn, Li, Ga, Ti, …) have demonstrated different physical properties, due to the concurrence of different valence states of Mn ions and magnetic interaction between the magnetic substituted ions and Mn ions [22-31]. De Lima et al. [22] investigated the magnetic properties of $LaMn_{1-x}Fe_xO_{3+\delta}$ ($0\leq x \leq 1$) samples and detected some signs of the occurrence of CG in the whole doping range as well as appearance of FM phase and suppression of ferromagnetism while x increased. Sun et al. [23] and Ramos et al. [24] reported that Cr-doping in the LMO samples introduced ferromagnetism and CG behavior. Gong et al. [25] and Tong et al. [26] studied magnetic, electrical, and magneto-transport properties of Zn-doped LMO samples. Focusing on Jahn-Teller effects on FM nature, PM-FM phase, MR behavior, and carrier transport mechanism, they found that Zn-doping could decrease the effects of Jahn-Teller distortion and observed CG behavior. Shana et al. [27] observed an RSG state for Ti-doped LMO samples. Hebert et al. [28] reported the effects of Co, Ni, Zn, Li, and Ga-doping in the LMO samples in detail and showed that establishment of ferromagnetism and enhancement of conductivity in all samples strongly depended on the valence of doping ions and, consequently, the Mn^{3+}/Mn^{4+} ratio.

Knizek et al. [29] studied the structural, electro-magnetic, and catalytic characterization of the $LaMn_{1-x}Cu_xO_{3+\delta}$ (x=0, 0.05, 0.10, 0.25, 0.5, 0.75, 0.90 and 0.95) samples prepared by the solid-state reaction method with different preparation procedures (slowly cooled and quenched samples). Different properties of those samples were reported.

This paper intended to obtain a comprehensive experimental characterization of the intermediated doped $LaMn_{1-x}Cu_xO_{3+\delta}$ (x=0, 0.025, 0.05, 0.075, and 0.125) samples prepared by a simple method, including novel results of AC magnetic susceptibility and resistivity versus temperature measurements.

2. EXPERIMENTAL PROCEDURE

The $LaMn_{1-x}Cu_xO_{3+\delta}$ (x= 0. 0.025, 0.05, 0.075, and 0.125) samples were prepared through a simple synthesis method which was based on grinding the acetate precursors in the presence of citric acid [32]. The synthesis process is briefly summarized in the following: first, manganese acetate, lanthanum acetate, copper acetate, and citric acid powders were mixed by an equal molar ratio of total metal acetates to citric acid. Then, the powders were ground for 2 h and the ground powders were annealed in the air at 600°C for 6 h. Next, the annealed powders were palletized under pressure of 10^5 N/cm^2 and sintered at 1200 °C for 6 h. The resistivity measurements were carried out by the four-probe method using a Leybold closed-cycle refrigerator. The AC susceptibility measurements were performed using a Lake Shore AC Susceptometer (Model 7000). Finally, the X-Ray Diffraction (XRD) patterns of the samples were taken on Philips XPERT X-ray diffractometer.

3. RESULTS AND DISCUSSION

3.1. STRUCTURAL PROPERTIES

Figure 1 shows XRD patterns for all samples. The XRD data were analyzed by Rietveld refinement using the FULLPROF program, the results of which are collected in Table 1. A typical diagram for Rietveld refinement analysis of x=0.025 sample is shown in Figure 1(b), which is indicative of a good agreement between the observed and calculated profiles. According to this analysis, no trace of secondary phase was detectable and the samples had an orthorhombic crystal structure with Pbnm space group.

Based on the data collected in Table 1, in case the x value changed from x=0 to 0.05 (first group), the unit cell volumes of the samples would slightly increase; however, these volumes decreased for x=0.075 and x=0.125 samples (second group).

The obtained results for the first group was already expected. Since the Cu ions with a stable form of Cu^{2+} [32, 33] have larger ionic radii (0.73 Å) than the average ionic radii of Mn (Mn^{3+} = 0.65 Å and Mn^{4+} = 0.53 Å) [27], the substitution of Cu^{2+} would systematically increase the bond length, lattice parameters, and unit cell volumes. However, the uncommon decreasing behavior in the unit cell volume of x=0.075 and x=0.125 samples suggests that some of the substituted Cu ions are in a Cu^{3+} state with a radius of 0.54 Å, which is smaller than that of Mn^{3+} and larger than that of Mn^{4+} [34]. Therefore, Cu^{3+} and Cu^{2+} states may appear in these samples, suggesting that the changes of the unite cell volume and lattice parameters are not regular with Cu content.

A similar phenomenon was observed in $(La,Ba)Cu_{1-x}Mn_xO_3$ and $La_{0.7}Sr_{0.3}Mn_{1-x}Cu_xO_3$ compounds, where Cu^{3+} ions were substituted for the Mn ions sites [35,36].

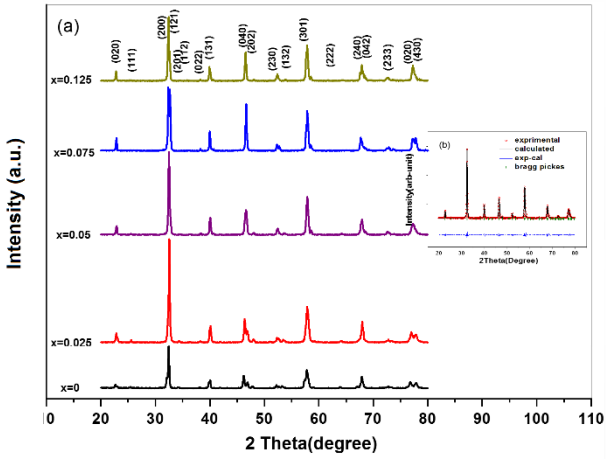

Figure 1. (a) XRD patterns for all samples, (b) Room temperature XRD pattern (red symbol) and Rietveld profile file (black line) for x=0.025 sample

TABLE 1. Lattice parameters (a and c), unit cell volume (V), average crystallite size, and (D) grain size

Sample Name	a (Å)	b (Å)	c (Å)	V (Å^3)
x=0.00	5.521(3)	5.432(6)	7.847(2)	235.376(9)
x=0.025	5.544(7)	5.397(1)	7.365(5)	235.513(1)
x=0.050	5.527(8)	5.450(6)	7.835(9)	235.673(2)
x=0.075	5.557(1)	5.373(6)	7.839(7)	234.100(1)
x=0.125	5.538(3)	5.393(2)	7.833(6)	233.986(1)

3.2. MAGNETIC PROPERTIES

Figures 2- 4(a) show the real (χ') and imaginary (χ'') parts of AC susceptibility for the samples that were measured in the AC field of 10 Oe and frequencies of 40, 111, 333, 666, and 1000 Hz, respectively.

Two peaks in the curves of AC susceptibility of the parent sample were observed upon decreasing the temperature, as shown in Figure 2(a). The sharp peak with a λ-shaped character was also observed at lower temperatures known as the Neel temperature, i.e., T_N, a frequency-independent temperature repeatedly observed for stoichiometric LMO samples between 100 and 140K [4, 5]. The broad peak observed in AC magnetic susceptibility curves might be related to Curie temperature.

While the stoichiometric LMO has AFM nature, non-stoichiometric LMO which easily adopts excess oxygen shows a different magnetic phase diagram [32, 37]. In fact, in the non-stoichiometric compound $LaMnO_{3+\delta}$, excess oxygen changes some of the Mn^{3+} ions to Mn^{4+} ions, thus leading to the charge imbalance in the lattice and, consequently, FM-DE interactions between Mn^{3+} and Mn^{4+} ions. In the magnetic phase diagram of $LaMnO_{3+\delta}$, both FM insulator and FM clusters embedded in an AFM matrix were observed depending on the values of δ [32, 37].

Therefore, the second peak observed in the curves of AC magnetic susceptibility (Fig.2(a)) at higher temperatures could be related to Curie temperature transition (T_C~167K); accordingly, the parent sample was considered non-stoichiometric $LaMnO_{3+\delta}$.

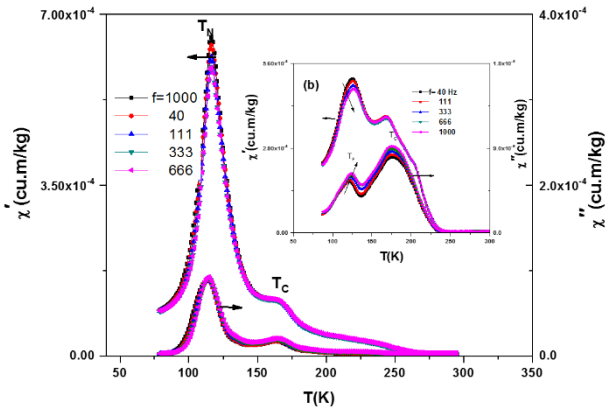

Figure 2. (a) Temperature dependence of left) χ' and right) χ'' for x=0 in a magnetic field of 10 Oe and frequencies of 40, 111, 333, 666, and 1000 Hz, (b) Temperature dependence of left) χ' and right) χ'' for x=0.025 in a magnetic field of 10 Oe and frequencies of 40, 111, 333, 666, and 1000 Hz

Joy et al. compared the Curie temperatures of $LaMnO_{3+\delta}$ compound and regarded them as a function of Mn^{4+} content from the related literature. They found that the Curie temperature of non-stoichiometric $LaMnO_{3+\delta}$ depended on the synthesis method or growth conditions such as calcination/sintering temperatures and could change from 60K to 280K [25]. A ccomparison of the values of Curie temperature (T_C~167K) obtained from the susceptibility magnetic measurement with those of other reports [32] confirmed that δ≤0.11 in the present sample.

Similar to the parent sample, two peaks were observed in the patterns of AC magnetic susceptibility of other samples as well. Figures 2(b)-4(a) show that Curie temperatures T_C become sharper and increase with the Cu content growth. The Cu^{2+} substitution on Mn sites produces the Mn^{4+} ions to maintain the electroneutrality of the lattice. Accordingly, upon increasing the Mn^{4+}/ Mn^{3+} ratio, the local DE between Mn^{3+} and Mn^{4+} would be developed in the Mn^{3+}-O-Mn^{3+} AFM background. Therefore, the peak corresponding to Curie

temperature for x=0.025 to x=0.075 samples (Fig.3 (b)) became considerably sharper. In the case of x=0.075 sample, the proportion of DE within the framework of the Mn^{3+}-O-Mn^{4+} interaction overwhelmed the AFM SE interactions of Mn^{3+}-O-Mn^{3+} and Cu^{2+}-O-Cu^{2+} networks. However, as depicted in Figure 4(a), the pattern of AC susceptibility indicates that while the proportion of DE decreases with further doping of Cu in x=0.125 sample, that of the Cu^{2+}-O-Cu^{2+} or Cu^{3+}-O-Cu^{3+} AFM interactions increases, thus decaying the macroscopic ferromagnetism in this sample. The same behavior was reported by Sun et al. in $LaMn_{1-x}Cu_xO_3$, but for x=0.3 sample [28]. Such difference was observed probably due to the Mn^{4+}/Mn^{3+} ratio in the crystal lattice of samples, which strongly depended on the oxygen stoichiometry [33].

Contrary to what is seen in Figure 2(a), for the first peak at a lower temperature for the parent sample, all the doped samples showed a frequency-dependent peak (T_f). T_f shifted towards higher temperature by increasing the frequency, thus confirming the coexistence and competition between FM and AFM interactions and favoring the formation of a spin/cluster glass states. Similar behavior was also identified by substituting Mn for Fe, Ti, Ga, Cr, and other cations in manganites [22, 38-40]. Such frequency-dependent behavior can be normally related to the existence of Spin-Glass(SG) or CG phases in these samples.

Based on the experimental data obtained from the frequency dependence of freezing temperature, T_f, can be expressed through the conventional Critical Slowing Down (CSD) model [41, 42]:

$$f = f_0\left(\frac{T_f - T_g}{T_g}\right)^{zv} \quad (1)$$

where f_0 is in the range of 10^{9}-$10^{13}s^{-1}$ for SG systems, T_g is the RSG transition temperature, and T_f is the frequency-dependent freezing temperature, at which the maximum relaxation time of the system corresponds to the measured frequency. Parameter zv is a dynamic critical exponent which shows the strength of interactions and varies between 4 and 12 for SG systems.

The Ln-Ln plot of the external frequency (f) versus reduced temperature, $(T_f - T_g)/T_g$, shows an excellent linear dependence, as depicted in Fig. 4(b). The best-fitting values are given in Table 2. The estimated values for x=0.025 and x=0.05 samples were within the realm of three-dimensional spin-glasses [43]. RSG behavior was found in a variety of disordered magnetic materials, in which there was a competition between SG ordering and long-range FM ordering, i.e., in the systems with a majority of FM couplings between the individual spins and a sufficiently large number of AFM couplings, to create substantial frustration. In case of a decrease in the temperature, this system shows a transition from PM to FM phases. Upon further reduction of the temperature, typical SG behavior, commonly called RSG, is observable. By substituting Cu for Mn, the density of the holes (Mn^{4+}) would increase and the DE interaction would be improved. Any increase in the Mn^{4+} and FM phase in AFM matrix would produce spin frustration and cause the occurrence of RSG in x= 0.025 and x= 0.05 samples. In the case of x=0.075, Cu content was sufficient to improve the long-range FM ordering with a CG regime at low temperatures. Therefore, the values given in Table 2 are out of the predicted values for the SG system. Moreover, in the case of x=0.125, AFM ordering is dominant and the estimated zv value is out of the predicted values for SG systems.

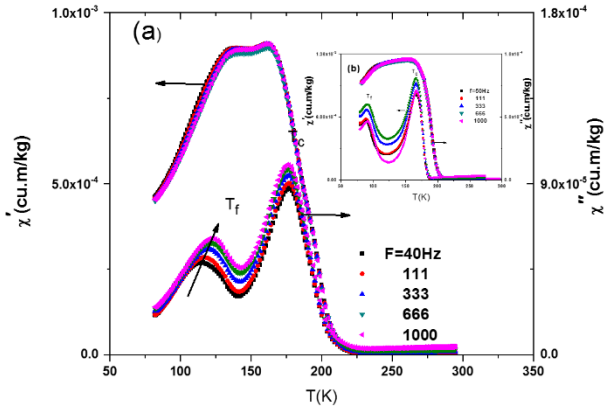

Figure 3. Temperature dependence of left) χ' and right) χ'' for x=0.0.05 in a magnetic field of 10 Oe and frequencies of 40, 111, 333, 666, and 1000 Hz, (b) Temperature dependence of left) χ' and right) χ'' for x=0.075 in a magnetic field of 10 Oe and frequencies of 40, 111, 333, 666, and 1000 Hz

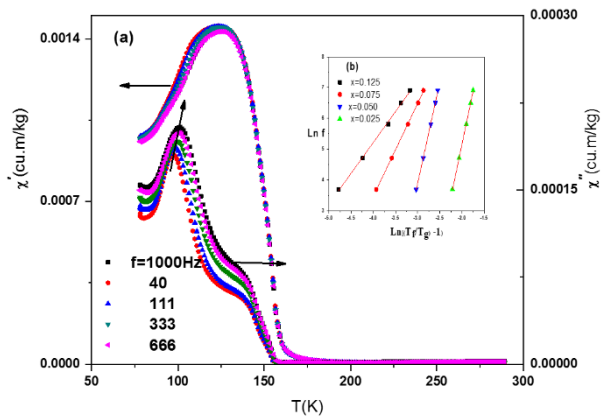

Figure 4. Temperature dependence of left) χ' and right) χ'' for x=0.0.125 in a magnetic field of 10 Oe and frequencies of 40, 111, 333, 666, and 1000 Hz, (b) Ln-Ln plot of the reduced temperature (T_f/T_g -1) versus frequency for all samples

TABLE 2. Parameters obtained from analysis of the experimental data using CSD model

Sample	T_c (K)	Zv	$f_0(s^{-1})$	T_g (K)
x=0	164		-	-
x=0.025	176	6.88	~ 10^{10}	120
x=0.050	177	6.58	~10^9	114
x=0.075	178	3.01	~10^7	93
x=0.125	140	2.00	~10^{10}	93

3.3. ELECTRICAL PROPERTIES

Electrical transport properties of the samples were systematically studied. Figure 5 shows the temperature dependence of resistivity for the samples.

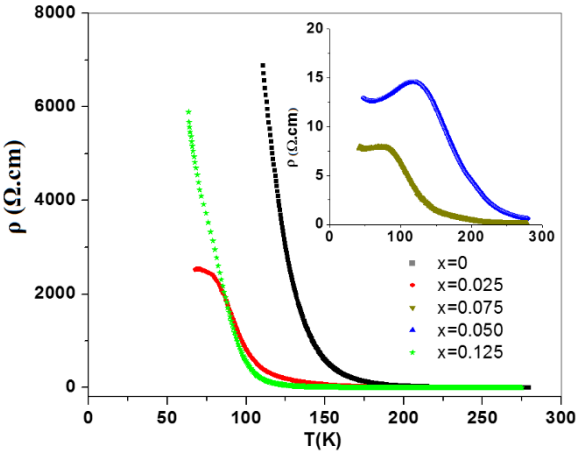

Figure 5. Temperature dependence of resistivity for the samples ρ (Ω.cm)

As observed, the parent sample (x=0) was an insulator in the whole measuring temperature. Upon increasing the doping level, the resistivity of all the samples would decrease and the curves of the temperature dependence of resistivity showed Metal-Insulator (MI) transition, except for x=0.125 sample. The resistivity of x= 0.075 sample was almost the third order of magnitude smaller than the x=0 sample. This kind of behavior can be justified by the percolation model [39]. Of note, there were an FM- DE interaction between Mn^{3+} and Mn^{4+} neighboring ions and an AFM- SE interaction between Mn^{3+} ions in the Perovskite manganites. While the FM interaction caused metallic behavior, the AFM interaction instigated insulating behavior. As mentioned earlier, the parent compound $LaMnO_3$ was the AFM insulator, in which doping of Cu ion in Mn ion site and excess oxygen would lead to enhancement of the Mn^{4+} ions ratio and consequently, the DE interaction and ferromagnetism. Moreover, an increase in the Cu content and excess oxygen would form FM clusters in the AFM matrix. Therefore, short-range ordering in the clusters would gradually increase to long-range ordering. For the un-doped sample, due to the low degree levels of Mn^{4+} ions, the FM clusters were separated and the volume of the FM clusters did not reach the percolation threshold. Therefore, the system exhibited a high-resistance and insulating behavior. As temperature decreased in Cu-doped samples to x=0.075 sample, the FM component increased and a percolation channel was formed due to the high levels of Mn^{4+} ions, hence a decrease in the resistivity and occurrence of the MI transition. In the case of x=0.125 sample, the substituted Cu for Mn sites formed an Mn^{3+}-O-Cu^{2+}/ Cu^{3+}- Mn^{4+} bonds which could create a potential barrier for charge carriers to hop. Therefore, at this level of doping, the MI transition would disappear.

To investigate the transport mechanism that can describe the temperature dependence of the resistivity of samples, the resistivity data of samples in the semiconducting region were selected and fitted by common models, namely Mott's Variable-Range Hopping (VRH) and Mott and Davis's Small Polaron Hopping (SPH) models [44, 45].

In Mott's VRH model, the transport mechanism is described as follows [46]:

$$\rho = \rho_0 exp(\frac{T_0}{T})^{1/4} \quad (2)$$

where T_0 is Mott characteristic temperature which is given by:

$$T_0 = \frac{18}{K_B N(E_f) a^2} \quad (3)$$

where N (E_F) is the Density of States (DOS) near the Fermi level, k_B is Boltzmann's constant, and *a* parameter is the localization length.

The mean hopping distance, $R_h(T)$, and hopping energy, $E_h(T)$, can be obtained at a given temperature T, as expressed in the following equations [47]:

$$R_h(T) = \frac{3}{8} a(\frac{T_0}{T})^{1/4} \quad (4)$$

$$E_h(T) = \frac{1}{4} K_B T^{1/4} T_0^{1/4} \quad (5)$$

The present resistivity data were fitted using Mott's VRH model to evaluate parameters ρ_0 and T_0. Figure 6(a) demonstrates the typical fitting analysis by comparing the experimental data and the model for x=0 and 0.025 samples.

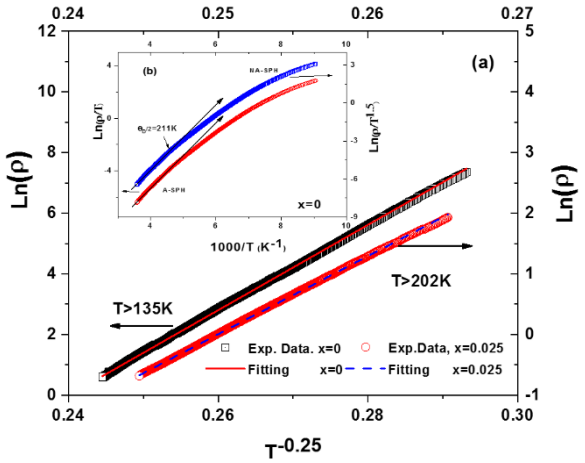

Figure 6. (a) Plot of Ln(ρ) versus $T^{-0.25}$ at different temperature regions (open symbols and lines represent the experimental data and fitting result, respectively, x=0 and x=0.025 samples (b) Plots of Ln (ρ/T) and Ln ($\rho/T^{3/2}$) versus (1/T) for the sample x=0

The plot revealed a good correlation between the data and model in different ranges of temperature, i.e., temperatures more than 135, 202, 217, 200, and 100K for x=0, 0.025, 0.05, 0.075, and 0.125 samples, respectively, suggesting the presence of two different valent transition–metal elements (Mn and Cu) in lattice-affected and electronic properties of a system due to the change in hopping conditions for charge carrier and induced distortion effects.

By considering the obtained values of T_0 from the fitted results, $N(E_F)$, R_h, and E_h were estimated at different temperatures of 100, 150, and, 300K (see Table 3) through taking the localization length of a= 4.5 Å, as reported for such materials [48].

TABLE 3. Values of $N(E_F)$, R_h, and E_h at room temperature

Sample	R^2	ρ_0(Ω.cm)	T_0	$N(E_F)$($eV^{-1}m^{-3}$) $\times10^{24}$	R_h(300K) (Å)	E_h(300K) (meV)
x=0	0.99958	2.12×10^{-15}	3.98×10^{8}	5.84	57.06	218.5
x=0.025	0.99971	1.08×10^{-14}	2.73×10^{8}	8.39	52.16	199.8
x=0.05	0.99936	1.2×10^{-11}	1.02×10^{8}	22	40.75	156.12
x=0.075	0.9940	2.58×10^{-11}	6.02×10^{7}	38	35.71	136.81
x=0.125	0.9963	1.66×10^{-13}	1.52×10^{8}	15	45.08	172.69

According to Table 3, by increasing the Cu-doping level, the density of states at the Fermi level increases, which corresponds to an increase in conductivity. Therefore, substitution of Cu for Mn ion sites could increase the Mn^{4+}/ Mn^{3+} ratio and, in this condition, the charge carriers would better hop between the Mn^{3+} to Mn^{4+} sites through DE mechanism. A decrease in the hopping distance (R_h) and hopping energy (E_h) of charge carrier obtained from the transport model confirmed the improvement of hopping conditions and accordingly, in the parent sample, e_g electrons of Mn^{+3} were more localized and, in the doped samples, the effective DE interaction between Mn^{+3}-Mn^{+4} became stronger.

The data for x=0.125 sample obtained from fitting showed a different behavior from those of other samples. As expected from the magnetic data analysis, in this sample, the formation of Mn^{3+}-O-Cu^{2+}/ Cu^{3+}- Mn^{4+} bonds decreased the connection channel and considerably increased charge carrier hopping distance, thus decreasing conductivity.

Another attempt was also made to confirm the nature of hopping conduction and the strength of electron–phonon interaction. The conduction mechanism for manganites at high temperatures, $T>\theta_D/2$ (θ_D is Debye's temperature) was mainly due to the thermally activated small polarons. The polaronic models are either adiabatic or non-adiabatic approximations. In the adiabatic regime, the nearest neighboring hopping of small polarons (Holstein polarons) leads to mobility with a thermally activated form, in which charge-carrier motion is faster than lattice vibrations. In the non-adiabatic regime, it is the opposite. According to these mechanisms, the temperature dependence of resistivity (ρ) is expressed as follows [48]:

$$\rho = \rho_\alpha T exp(\frac{E_a}{K_B T}) \quad \text{(adiabatic)} \tag{6}$$

$$\rho = \rho_\alpha T^{3/2} exp(\frac{E_a}{K_B T}) \quad \text{(non-adiabatic)} \tag{7}$$

where E_a, ρ_α, and K_B are activation energy, residual resistivities, and Boltzman's constant, respectively.

Conduction can occur in either adiabatic or non-adiabatic models. Therefore, through Equations (6) and (7), the Ln (ρ/T) and Ln ($\rho/T^{3/2}$) versus (1/T) plot was separately drawn for the samples. Figure 7 shows the typically related plots for x=0 and 0.05. Within all temperature ranges of measurements, Debye's temperature for the samples was estimated from the plots of Ln (ρ/T) and Ln ($\rho/T^{3/2}$) versus (1000/T). The value of $\theta_D/2$ was considered to be the deviation point from linearity in the low-temperature region [49-53]. The obtained values of θ_D were calculated as 430, 442, 432,400, and 310K for x=0, 0.025, 0.050, 0.075, and 0.125 samples, respectively, which were close to the previously reported values for similar compounds [52, 53].

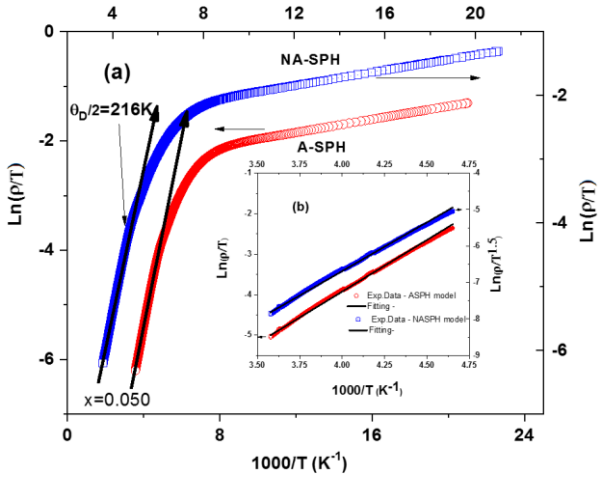

Figure 7. Plots of Ln (ρ/T) and Ln ($\rho/T^{3/2}$) versus (1/T) for the sample x=0. 05 (b) Plots of experimental data of the sample x=0 (with adiabatic small polaron hopping (ASPH) and non-adiabatic small polaron hopping (NASPH) models

The data of the high temperature just above Debye's temperatures ($\theta_D/2$) were selected to study the transport regime and fitted by adiabatic and non-adiabatic models. Figure 8 shows the related plots for x=0 and x=0.05. The obtained parameters are given in Table 4. As observed in the data collected in Table 4, the linear correlation coefficients, R^2, for the samples were very close to 1 and were almost the same for both models. Therefore, it was difficult to identify the nature of the hopping mechanism in this temperature range by this analysis.

In order to find how the carriers hop, i.e., adiabatic or non-adiabatic hopping, in this temperature range, the necessary conditions for using either of these mechanisms should be checked. Holstein's relation can help distinguish the kind of hopping mechanism [49]. It can be suggested that J (polaron bandwidth) can be treated as a perturbation in the corresponding Schrödinger equation. According to Holstein's condition, J should satisfy the inequality $J>\phi$ for adiabatic hopping and $J<\phi$ for non-adiabatic hopping conduction, where ϕ is:

$$\emptyset = \left(\frac{2K_B T E_a}{\pi}\right)^{\frac{1}{4}}\left(\frac{h\nu}{\pi}\right)^{1/2} \quad (8)$$

Moreover, the condition for small-polaron formation is $J<E_a/3$ [49]; otherwise, there will be large polarons.

The value of J can be estimated by approximating the equation for high-temperature jump site [51, 52]:

$$J \cong 0.67 h\nu_{ph}\left(\frac{T}{\theta_D}\right)^{1/4} \quad (9)$$

In this evaluation, ν_{ph} was estimated to be about 10^{13} Hz from the relation $h\nu_{ph}=k_B\theta_D$ (see Table 4) and T=200 and 300 K. Since $J<\phi$ and $J<E_a/3$ for all the samples, it can be concluded that the nan-adiabatic small polaron hopping model was responsible for conduction in all samples in this temperature range.

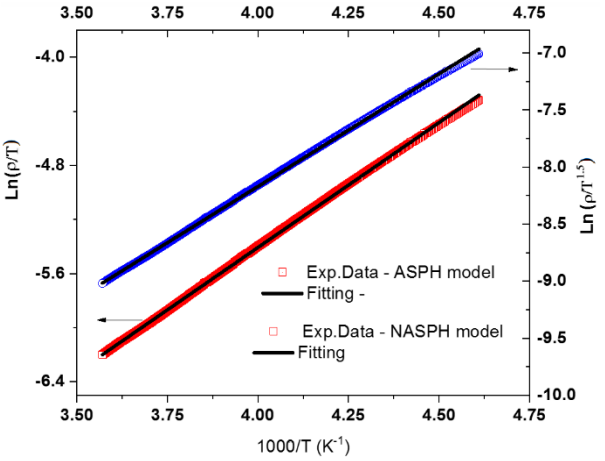

Figure 8. Plots of experimental data of the sample x=0.05 (with adiabatic small polaron hopping (ASPH) and non-adiabatic small polaron hopping (NASPH) models

It is interesting to estimate a few important relevant physical parameters for compounds. The values for small-polaron coupling (γ_p), which is a measure of electron-phonon interaction in these manganites, can be evaluated from the following relation:
$\gamma_p=2E_a/h\nu_{ph}$ [54,55].
In addition, the polaron mass (m_p) and rigid lattice effective mass (m^*) in the manganites were related by the following equation [54]:

$$m_p = \left(\frac{h^2}{8\pi^2 J a_P}\right)\exp(\gamma_P) = m^*\exp(\gamma_P) \quad (10)$$

The calculated values for γ_p and $m_P/m^*=\exp(\gamma_p)$ are collected in Table 4 that shows a drecrease in the γ_p and m_P/m^* values for the doped samples. If the value of γ_p is greater than 4, there are strong electron–phonon (e-ph) interaction in the system; otherwise, the interactions are weak [51, 54].

According to Table 4, the values of the present samples were found to be more than 4, thus confirmeing the strong e-ph interactions in the compounds and ensuring the formation of polarons. Moreover, as the Cu concentration increased, the strengh of the e-ph coupling constant systematically decreased, which resulted in the creation of the Mn^{+4} inos in the doped samples and improvement of DE interaction. The reduction of e-ph coupling stopped in the case of x=0.125 sample. Analysis of the transport properties of the samples showed that distortion of the unit cell causing the JT effect decreased and this effect was suddenly weakened in x=0.125 sample, which could be closely correlated to structural and magnetic analyses.

TABLE 4. Some important estimated parameters related to ADSPH and NADSPH models

Sample	θ_D (K)	$\nu_{Ph}\times10^{-13}$	ADSPH-Model		NADSPH-Model		ϕ(meV)		J (meV)		γ_p	m_p/m
			R^2	E_p(mev)	R^2	E_p(mev)	At T=200K	At T=300K	At T=200K	At T=300K		
x=0	430	0.84	0.9975	220	0.9974	231	23.32	25.8	19.29	21.34	11.9	147.3
x=0.025	442	0.92	0.99911	199	0.99912	210	23.79	26.31	20.94	23.16	10.4	34.2
x=0.050	432	0.90	0.99983	159	0.99982	170	22.24	24.6	20.57	22.76	8.5	5.0
x=0.075	400	0.83	0.9981	138	0.9984	149	20.66	22.85	19.41	21.47	8.0	3.0
x=0.125	310	0.64	0.99989	146	0.99981	155	18.45	20.41	16.01	17.74	11	59.8

4. CONCLUSION

In this paper, the effect of Cu doping on $LaMn_{1-x}Cu_xO_{3+\delta}$ (x= 0-0.125) manganite material was investigated. The results of powder X-ray diffraction indicated that the samples were single-phased and crystallized in an orthorhombic structure with Pbnm space group. Enhancement in the unit cell volumes of the doped samples to x=0.050 was systematical. However, after the maximum of 7.5% substitution of Cu, a decrease in the unit cell volumes was observed. Any uncommon decrease in the unit cell volume of x=0.075 and x=0.125 samples could be a result of the appearance of Cu ions as Cu^{3+} state in this sample. The PM-FM transition temperature, T_c, increased when the Cu content increased. RSG state accompanied by FM transition existed in x= 0.025 and x= 0.05 samples. By substituting Cu for Mn, the density of the holes (Mn^{4+}) increased and the DE interaction was improved. An increase in the DE interaction and FM phase in AFM matrix produced spin frustration and RSG in x= 0.025 and x= 0.05 samples. In the x=0.075 sample, the FM ordering was observed and the magnetic data analysis based on the critical slowing model confirmed the CS state in this sample. After 7.5% doping in the Mn site by Cu, the AFM phase overcame the FM phase due to the reduction of DE interaction. Investigation of the electrical behavior based on VRH and polaronic transport models was performed according to the structural and magnetic measurement analyses.

ACKNOWLEDGEMENT

The authors would like to thank Isfahan University of Technology for supporting this project.

REFERENCES

1. Jin, S., Tiefel, T. H., McCormack, M., Fastnacht, R. A., Ramesh, R., Chen, L. H., "Thousandfold change in resistivity in magnetoresistive La-Ca-Mn-O films", ***Science***, Vol. 264, No. 5157, (1994), 413-415. https://doi.org/10.1126/science.264.5157.413
2. Asamitsu, A., Moritomo, Y., Tomioka, Y., Arima, T., Tokura, Y., "A structural phase transition induced by an external magnetic field", ***Nature***, Vol. 373, No. 6513, (1995), 407-409. https://doi.org/ 10.1038/373407a0
3. Tokura, Y., Ed., ***Colossal Magnetoresistive Oxides***, CRC Press, (2000). https://doi.org/10.1201/9781482287493
4. Töpfer, J., Goodenough, J. B., "Transport and Magnetic Properties of the Perovskites La_{1-y} MnO_3 and $LaMn_{1-z}$ O_3", ***Chemistry of Materials***, Vol. 9, No. 6, (1997), 1467-1474. https://doi.org/10.1021/cm9700211
5. Chandra, S., Biswas, A., Datta, S., Ghosh, B., Siruguri, V., Raychaudhuri, A. K., Phan, M. H., Srikanth, H., "Evidence of a canted magnetic state in self-doped LaMnO3+ δ (δ= 0.04): a magnetocaloric study", ***Journal of Physics: Condensed Matter***, Vol. 24, No. 36, (2012), 366004. https://doi.org/10.1088/0953-8984/24/36/366004
6. Zener, C., "Interaction between the d-shells in the transition metals. II. Ferromagnetic compounds of manganese with perovskite structure", ***Physical Review***, Vol. 82, No. 3, (1951), 403. https://doi.org/10.1103/PhysRev.82.403
7. Anderson, P. W., Hasegawa, H., "Considerations on double exchange", ***Physical Review***, Vol. 100, No. 2, (1955), 675. https://doi.org/10.1103/PhysRev.100.675
8. De Gennes, P. G., "Effects of double exchange in magnetic crystals", ***Physical Review***, Vol. 118, No. 1, (1960), 141. https://doi.org/10.1103/PhysRev.118.141
9. Malavasi, L., Mozzati, M. C., Azzoni, C. B., Chiodelli, G., Flor, G., "Role of oxygen content on the transport and magnetic properties of $La_{1-x}Ca_xMnO_{3+\delta}$ manganites", ***Solid State communications***, Vol. 123, No. 8, (2002), 321-326. https://doi.org/10.1016/S0038-1098(02)00376-9
10. Maguire, E. T., Coats, A. M., Skakle, J. M., West, A. R., "Stoichiometry and defect structure of 'NdMnO$_3$", ***Journal of Materials Chemistry***, Vol. 9, No. 6, (1999), 1337-1346. https://doi.org/10.1039/a900734b
11. Dagotto, E., "Phase Diagrams and Basic Properties of Manganites", In ***Nanoscale Phase Separation and Colossal Magnetoresistance***, Springer Series in Solid-State Sciences, vol

136. Springer, Berlin, Heidelberg. https://doi.org/10.1007/978-3-662-05244-0_3

12. Wollan, E. O., Koehler, W. C., "Neutron diffraction study of the magnetic properties of the series of perovskite-type Compounds [(1− x) La, x Ca] Mn O $_3$", ***Physical Review***, Vol. 100, No. 2, (1955), 545. https://doi.org/10.1103/PhysRev.100.545
13. Kagan, M. Y., Klaptsov, A. V., Brodsky, I. V., Kugel, K. I., Sboychakov, A. O., Rakhmanov, A. L., "Nanoscale phase separation in manganites", ***Journal of Physics A: Mathematical and General***, Vol. 36, No. 35, (2003), 9155. https://doi.org/10.1088/0305-4470/36/35/304
14. Hwang, H. Y., Cheong, S. W., Radaelli, P. G., "Lattice Effects on the Magnetoresistance in Doped $LaMnO_3$", ***Physical Review Letters***, Vol. 75, No. 5, (1995), 914. https://doi.org/10.1103/PhysRevLett.75.914
15. Zarifi, M., Kameli, P., Ehsani, M. H., Ahmadvand, H., Salamati, H., "Effects of rare earth ions substitution on the magnetocaloric and critical behavior of $La_{0.6}A_{0.2}Sr_{0.2}MnO_3$ (A= Pr, Nd, Ce) manganite", ***Journal of Alloys and Compounds***, Vol. 718, (2017), 443-452. https://doi.org/10.1016/j.jallcom.2017.05.196
16. Arabi, A., Fazli, M., Ehsani, M. H., "Tuning the morphology and photocatalytic activity of $La_{0.7}Ca_{0.3}MnO_3$ nanorods via different mineralizer-assisted hydrothermal syntheses", ***Materials Research Bulletin***, Vol. 90, (2017), 205-211. https://doi.org/10.1016/j.materresbull.2017.02.043
17. Zarifi, M., Kameli, P., Ehsani, M. H., Ahmadvand, H., Salamati, H., "Effects of strain on the magnetic and transport properties of the epitaxial $La_{0.5}Ca_{0.5}MnO_3$ thin films", ***Journal of Magnetism and Magnetic Materials***, Vol. 420, (2016), 33-38. https://doi.org/10.1016/j.jmmm.2016.06.081
18. Ehsani, M. H., Raoufi, T., Razavi, F. S., "Impact of Gd ion substitution on the magneto-caloric effect of $La_{0.6-x}Gd_xSr_{0.4}MnO_3$ (x= 0, 0.0125, 0.05, 0.10) manganites", ***Journal of Magnetism and Magnetic Materials***, Vol. 475, (2019), 484-492. https://doi.org/10.1016/j.jmmm.2018.11.131
19. Ehsani, M. H., Raoufi, T., "Effect of Gd substitution on the critical scaling of the ferromagnetic transition of $La_{0.6-x}Gd_xSr_{0.4}MnO_3$ (x= 0, 0.05, 0.1) manganite", ***Journal of Alloys and Compounds***, Vol. 769, (2018), 649-659. https://doi.org/10.1016/j.jallcom.2018.08.022
20. Esmaeili, S., Ehsani, M. H., Fazli, M., "Photo-catalytic activities of $La_{0.7}Ba_{0.3}MnO_3$ nanoparticles", ***Optik***, Vol. 216, (2020), 164812. https://doi.org/10.1016/j.ijleo.2020.164812
21. Esmaeili, S., Ehsani, M. H., Fazli, M., "Structural, optical and photocatalytic properties of $La_{0.7}Ba_{0.3}MnO_3$ nanoparticles prepared by microwave method", ***Chemical Physics***, Vol. 529, (2020), 110576. https://doi.org/10.1016/j.chemphys.2019.110576
22. De Lima, O. F., Coaquira, J. A. H., De Almeida, R. L., De Carvalho, L. B., Malik, S. K., "Magnetic phase evolution in the $LaMn_{1-x}Fe_xO_{3+y}$ system", ***Journal of Applied Physics***, Vol. 105, No. 1, (2009), 013907. https://doi.org/10.1063/1.3054323
23. Sun, Y., Tong, W., Xu, X., Zhang, Y., "'Possible double-exchange interaction between manganese and chromium in $LaMn_{1-x}Cr_xO_3$", ***Physical Review B***, Vol. 63, No. 17, (2001), 174438. https://doi.org/10.1103/PhysRevB.63.174438
24. Ramos, A. Y., Tolentino, H. C., Soares, M. M., Grenier, S., Bunău, O., Joly, Y., Baudelet, F., Wilhelm, F., Rogalev, A., Souza, R. A., Souza-Neto, N. M., "Emergence of ferromagnetism and Jahn-Teller distortion in $LaMn_{1-x}Cr_xO_3$ (x<0.15)", ***Physical Review B***, Vol. 87, No. 22, (2013), 220404. https://doi.org/10.1103/PhysRevB.87.220404
25. Gong, F., Tong, W., Tan, S., Zhang, Y., "Large effect of small Zn doping on the electric and magnetic properties in $LaMn_{1-x}Zn_xO_3$", ***Physical Review B***, Vol. 68, No. 17, (2003), 174410. https://doi.org/10.1103/PhysRevB.68.174410
26. Hu, L., Tong, W., Zhu, H., Zhang, Y., "The effects of Jahn–Teller distortion changes on transport properties in $LaMn_{1-x}Zn_xO_3$", ***Journal of Physics: Condensed Matter***, Vol. 15, No. 12, (2003), 2033. https://doi.org/10.1088/0953-8984/15/12/320
27. Sahana, M., Venimadhav, A., Hegde, M. S., Nenkov, K., Rößler, U. K., Dörr, K., Müller, K. H., "Magnetic properties and specific heat of $LaMn_{1-x}Ti_xO_{3+\delta}$ (0< x≤ 0.2)", ***Journal of Magnetism and Magnetic Materials***, Vol. 260, No. 3, (2003), 361-370. https://doi.org/10.1016/S0304-8853(02)01341-0
28. Hébert, S., Martin, C., Maignan, A., Retoux, R., Hervieu, M., Nguyen, N., Raveau, B., "Induced ferromagnetism in LaMnO 3 by Mn-site substitution: The major role of Mn mixed valency", ***Physical Review B***, Vol. 65, No. 10, (2002), 104420. https://doi.org/10.1103/PhysRevB.65.104420
29. Sun, Y., Xu, X., Tong, W., Zhang, Y., "Double-exchange ferromagnetism and magnetoresistance in $LaMn_{1-x}Cu_xO_3$ (x≤0.3)", ***Applied Physics Letters***, Vol. 77, No. 17, (2000), 2734-2736. https://doi.org/10.1063/1.1320021
30. Michel, C., "Structural, electro-magnetic and catalytic characterisation of the $LaMn_{1-x}Cu_xO_{3-\delta}$ system", ***Journal of Material Chemistry***, Vol. 8, No. 8, (1998), 1815-1819. https://doi.org/10.1039/a801503a
31. Eshraghi, M., Kameli, P., Khalili, F., Ehsani, M. H., Salamati, H., "Structural, magnetic and electrical characterization of the $La_{0.7}Ca_{0.3}Co_{1-x}Mn_xO_3$ (x= 0, 0.7 and 1) compounds prepared by a simple method", ***Journal of Rare Earths***, Vol. 32, No. 10, (2014), 965-972. https://doi.org/10.1016/s1002-0721(14)60170-8
32. Amirzadeh, P., Ahmadvand, H., Kameli, P., Aslibeiki, B., Salamati, H., Gamzatov, A. G., Aliev, A. M., Kamilov, I. K., "Phase separation and direct magnetocaloric effect in $La_{0.5}Ca_{0.5}MnO_3$ manganite", ***Journal of Applied Physics***, Vol. 113, No. 12, (2013), 123904. https://doi.org/10.1063/1.4794179
33. Joy, P. A., Sankar, C. R., Date, S. K., "The origin of ferromagnetism in $LaMnO_{3+\delta}$", ***Journal of Physics: Condensed Matter***, Vol. 14, No. 19, (2002), 4985. https://doi.org/10.1088/0953-8984/14/19/320
34. Zhang, H., Shi, J., Li, Y., Liu, H., Dong, X., Chen, K., Hou, Q., Huang, Y., Ge, X., Zhao, L., Lu, Z., "Local Atomic and Electronic Structure with Magnetism of $La_{0.7}Ca_{0.3}Mn_{1-x}Cu_xO_3$ (x= 0, 0.03, 0.06, 0.1)", ***Journal of Low Temperature Physics***, Vol. 169, No. 1-2, (2012), 77-89. https://doi.org/10.1007/s10909-012-0644-1
35. Shannon, R. D., "Revised effective ionic radii and systematic studies of interatomic distances in halides and chalcogenides", ***Acta Crystallographica Section A: Crystal Physics, Diffraction, Theoretical and General Crystallography***, Vol. 32, No. 5, (1976), 751-767. https://doi.org/10.1107/s0567739476001551
36. Yuan, S. L., Jiang, Y., Li, G., Li, J. Q., Yang, Y. P., Zeng, X. Y., Tang, P., Huang, Z., "Semiconductor-metal transition and magnetoresistance in $La_{(1+x)/3}Ba_{(2-x)/3}Cu_{1-x}Mn_xO_3$", ***Physical Review B***, Vol. 61, No. 5, (2000), 3211. https://doi.org/10.1103/physrevb.61.3211
37. Kim, M. S., Yang, J. B., Medvedeva, J., Yelon, W. B., Parris, P. E., James, W. J., "Electronic structure of $La_{0.7}Sr_{0.3}Mn_{1-x}Cu_xO_3$ (0.0≤ x≤ 0.30)", ***Journal of Physics: Condensed Matter***, Vol. 20, No. 25, (2008), 255228. https://doi.org/10.1088/0953-8984/20/25/255228
38. Töpfer, J., Goodenough, J. B., "$LaMnO_{3+\delta}$ Revisited", ***Journal of Solid State Chemistry***, Vol. 130, No. 1, (1997), 117-128. https://doi.org/10.1006/jssc.1997.7287
39. Aslibeiki, B., Kameli, P., Salamati, H., "Reentrant spin glass behavior in $La_{0.8}Sr_{0.2}Mn_{1-x}Ti_xO_3$ manganites", ***Solid State Communications***, Vol. 149, No. 31-32, (2009), 1274-1277. https://doi.org/10.1016/j.ssc.2009.05.012
40. Pękała, M., Mucha, J., Vertruyen, B., Cloots, R., Ausloos, M., "Effect of Ga doping on magneto-transport properties in colossal magnetoresistive $La_{0.7}Ca_{0.3}Mn_{1-x}Ga_xO_3$ (0< x< 0.1)", ***Journal of***

Magnetism and Magnetic Materials, Vol. 306, No. 2, (2006), 181-190. https://doi.org/10.1016/j.jmmm.2006.02.241

41. Dho, J., Kim, W. S., Hur, N. H., "Reentrant spin glass behavior in Cr-doped perovskite manganite", ***Physical Review Letters***, Vol. 89, No. 2, (2002), 027202. https://doi.org/10.1103/physrevlett.89.027202
42. Srivastava, S. K., Kar, M., Ravi, S., "Ferromagnetic insulating and spin glass behavior in Cr substituted $La_{0.85}Ag_{0.15}MnO_3$ compounds", ***Journal of Physics: Condensed Matter***, Vol. 20, No. 23, (2008), 235201. https://doi.org/10.1088/0953-8984/20/23/235201
43. Viswanathan, M., Kumar, P. A., "Observation of reentrant spin glass behavior in $LaCo_{0.5}Ni_{0.5}O_3$", ***Physical Review B***, Vol. 80, No. 1, (2009), 012410. https://doi.org/10.1103/physrevb.80.012410
44. Mydosh, J. A., ***Spin Glasses: An Experimental Introduction***, Taylor and Francis, (1993). https://doi.org/10.1201/9781482295191
45. Pi, L., Zheng, L., Zhang, Y., "Transport mechanism in polycrystalline $La_{0.825}Sr_{0.175}Mn_{1-x}Cu_xO_3$", ***Physical Review B***, Vol. 61, No. 13, (2000), 8917. https://doi.org/10.1103/physrevb.61.8917
46. Banerjee, A., Pal, S., Chaudhuri, B. K., "Nature of small-polaron hopping conduction and the effect of Cr doping on the transport properties of rare-earth manganite $La_{0.5}Pb_{0.5}Mn_{1-x}Cr_xO_3$", ***The Journal of Chemical Physics***, Vol. 115, No. 3, (2001), 1550-1558. https://doi.org/10.1063/1.1378018
47. Mott, N. F., "Conduction in glasses containing transition metal ions", ***Journal of Non-Crystalline Solids***, Vol. 1, No. 1, (1968), 1-17. https://doi.org/10.1016/0022-3093(68)90002-1
48. Ravi, S., Kar, M., "Study of magneto-resistivity in $La_{1-x}Ag_xMnO_3$ compounds", ***Physica B: Condensed Matter***, Vol. 348, No. 1-4, (2004), 169-176. https://doi.org/10.1016/j.physb.2003.11.087
49. Emin, D., Holstein, T., "Studies of small-polaron motion IV. Adiabatic theory of the Hall effect", ***Annals of Physics***, Vol. 53, No. 3, (1969), 439-520. https://doi.org/10.1016/0003-4916(69)90034-7
50. Holstein, T., "Theory of transport phenomena in an electron-phonon gas", ***Annals of Physics***, Vol. 29, No. 3, (1964), 410-535. https://doi.org/10.1016/0003-4916(64)90008-9
51. Mollah, S., Khan, Z. A., Shukla, D. K., Arshad, M., Kumar, R., Das, A., "Adiabatic small polaron-hopping conduction in $Ln_{0.85}Ca_{0.15}MnO_3$ (Ln= Nd, Pr and Sm) perovskites", ***Journal of Physics and Chemistry of Solids***, Vol. 69, No. 4, (2008), 1023-1028. https://doi.org/10.1016/j.jpcs.2007.11.024
52. Ehsani, M. H., Kameli, P., Ghazi, M. E., "Influence of grain size on the electrical properties of the double-layered $LaSr_2Mn_2O_7$ manganite", ***Journal of Physics and Chemistry of Solids***, Vol. 73, No. 6, (2012), 744-750. https://doi.org/10.1016/j.jpcs.2012.01.020
53. Mansuri, I., Varshney, D., Kaurav, N., Lu, C. L., Kuo, Y. K., "Effects of A-site disorder on magnetic, electrical and thermal properties of $La_{0.5-x}Ln_xCa_{0.5-y}Sr_yMnO_3$ manganites", ***Journal of Magnetism and Magnetic Materials***, Vol. 323, No. 3-4, (2011), 316-323. https://doi.org/10.1016/j.jmmm.2010.09.026
54. Banerjee, A., Pal, S., Rozenberg, E., Chaudhuri, B. K., "Adiabatic and non-adiabatic hopping conduction in La–Pb–Mn–O type system", ***Journal of Alloys and Compounds***, Vol. 326, No. 1-2, (2001), 85-88. https://doi.org/10.1016/s0925-8388(01)01229-4
55. Austin, I. G., Mott, N. F., "Polarons in crystalline and non-crystalline materials", ***Advances in Physics***, Vol. 18, No. 71, (1969), 41-102. https://doi.org/10.1080/00018736900101267

Advanced Ceramics Progress: Vol. 7, No. 1, (Winter 2021) 11-17

Advanced Ceramics Progress

Research Article

Journal Homepage: www.acerp.ir

Synthesis and Characterization of Palladium Impregnated MIL-53(Fe) as Cathode Material of Supercapacitor

B. Chameh [a], M. Moradi [a] *, S. Hajati [a], F. Alikhani Hessari [a], M. A. Kiani [b]

[a] *Department of Semiconductors, Materials and Energy Research Center (MERC), Meshkindasht, Alborz, Iran*

[b] *Chemistry & Chemical Engineering Research Center of Iran, Tehran, Tehran, Iran*

ARTICLE INFO

Article History:

Received 26 September 2020
Received in revised form 19 October 2020
Accepted 29 October 2020

Keywords:

Decoration
Metal Organic Framework
Capacitance
Electrochemistry
Nanoparticle

ABSTRACT

Recently, Metal Organic Frameworks (MOFs) have been widely applied due to their high energy storage capacitance, customizable pore sizes, and open metal sites; however, their application in the form of electrode materials has been restricted due to their poor electrical conductivity. The present study reports the fast synthesis of MIL-53(Fe) and Pd/MIL-53(Fe) using the solvothermal method. To assess the electrochemical potential of materials and better understand the role of palladium in the presence of MOF, the electrodes of materials were constructed and electrochemical performances of both samples were investigated based on cyclic voltammetry in 6 M KOH electrolyte. Due to the existence of Pd in redox reaction and larger surface area, the Pd/MIL-53(Fe) showed greater electrochemical efficiency and higher specific capacitance than MIL-53(Fe). The obtained results also indicated that designing MOF via decoration of noble metal nanoparticle (MOF/noble metal) would find potential applications in the field of supercapacitors and catalysis.

https://doi.org/10.30501/acp.2020.250166.1045

1. INTRODUCTION

Over the past two decades, owing to their unique characteristics, Metal Organic Frameworks (MOFs) have drawn a great deal of attention in a variety of applications [1]. They have been widely used due to their capability to take in chemical and structural modifications through different metals, bridging ligands, and synthesis methods [2,3] and to offer considerable flexibility for tuning topologies, sizes, and pore structures [4–6]. These characteristics ensure their promising candidacy for applications such as gas storage and separations [8], catalyst [9], drug delivery and imaging [10], and conversion and energy storage devices such as fuel cells, batteries, and supercapacitors [11]. However, shuffled orientations are regarded as the main obstacle for these compounds [12]. They have relatively low electrical conductivity owing to the insulating characteristic of the organic linkers and poor overlap between π and d orbitals of the metal ions [13], limiting the effective application of built-in redox centers, hence low power density and capacitance [14,15].

Noble metal-based materials are regarded as ideal additives of electrode materials due to their enhanced chemical and thermal stability of the electrode materials. Moreover, they make feasible the movement of electrons from the electrode/electrolyte interface to the current collectors. Noble metal particles increase the capacitance of the electrical double layer by supplying wider electrochemically active surface areas for adsorption of ions. These metals commonly include a group of platinum (palladium, ruthenium, platinum, iridium, rhodium, osmium), gold, and silver [16]. However, their combination with other sustainable and cheap materials is considered one of the most desirable ways of maximizing material properties and usage due to their

* Corresponding Author Email: 2m.alborzi@gmail.com (M. Moradi)

http://www.acerp.ir/article_128022.html

Please cite this article as: Chameh, B., Moradi, M., Hajati, S., Alikhani Hessari, F., Kiani, M. A., "Synthesis and Characterization of Palladium Impregnated MIL-53(Fe) as Cathode Material of Supercapacitor", ***Advanced Ceramics Progress***, Vol. 7, No. 1, (2021), 11-16. https://doi.org/10.30501/acp.2020.250166.1045

scarcity and high cost [17-22]. The preparation of Pd@MOF-5 (1 wt. % Pd) was described by a solution of [$Pd(acac)_2$] in $CHCl_3$ and subsequent thermal hydrogenolysis of the intermediate material [$Pd(acac)_2$]x@MOF-5 (x 1⁄4 0.074). The authors did not provide information on the sizes of the Pd particles and distribution over the matrix [23]. In another study, Haruta et al. reported Au@MOFs (1–2 wt. percent au) and catalytic characteristics of liquid-phase aerobic alcohol oxidation [24].

In this research, the process of loading Pd nanoparticles on MIL-53(Fe) was carried out by facial hydrothermal method at room temperature. The electrochemical test of cyclic voltammetry on the fabricated electrode with synthesized materials was done the results of which showed improvement in the electrochemical performance of Pd/MIL-53(Fe), mainly due to an increase in the wettability and the specific surface area of MOF by Pd nanoparticles.

2. EXPERIMENTAL PROCEDURE

2.1. Materials

Iron chloride hexahydrate ($FeCl_3 \cdot 6H_2O$), N,N-dimethylformamide (DMF), terephthalic acid (1,4-BDC), hydrofluoric acid 48%, sodium tetrachloropalladate (II), 98% (Na_2PdCl_4), and sodium tetrahydridoborate, >98% ($NaBH_4$) were used without further purification. All chemicals used in this study were of commercially available analytical grade.

2.2. Synthesis of MIL-53(Fe)

MIL-53(Fe) was synthesized through the following procedure. First, $FeCl_3$. $6H_2O$ (10 mmol, 2.7 g), N,N-dimethylformamide (DMF) (50 mL), aqueous HF (10 mmol, 0.2 g), and 1,4-benzenedicarboxylic acid (H_2BDC) (10 mmol, 1.66 g) were mixed and stirred for 30 min; then, the mixture was placed in a Teflon-lined steel autoclave. The mixture was heated in a preheated fan oven at 150 ˚C for three days. Followed by cooling the autoclave to room temperature, MIL-53(Fe)[DMF] powder was recovered by filtration and washed with MeOH to obtain MIL-53(Fe)[MeOH]. MIL-53(Fe) was eventually achieved after MIL-53(Fe) [MeOH] had been washed with water and dried in air overnight [20].

2.3. Synthesis of Pd/MIL-53(Fe)

All the reagents were used without further purification. In this study, 10 mg of Na_2PdCl_4 was dissolved in 10 ml of deionized water to form a clear solution, which was subsequently poured into 10 mL of deionized water containing 200 mg of MIL-53(Fe). After thorough mixing, the resulting solution was stirred for 17 h at room temperature. Finally, 2.5 mg $NaBH_4$ dissolved in 5 ml deionized water was added to the previous mixture and stirred for 3 h. The as-obtained precipitates were then centrifuged and washed with ethanol and water for several times and dried at 70 °C for 24 h.

2.4. Materials characterization

X-Ray Diffraction (XRD, Philips X´pert diffractometer possessing Co Kα radiation, λ = 1.78 Å) was employed to explore the crystal phase of the materials at 40 kV and 30 mA with a 0.04 $^{\circ}s^{-1}$ step size. A pore size and surface area analyzer (Phschina, PHS 1020) were also used to extract the nitrogen adsorption/desorption isotherms at 77 K. Brunauer-Emmett-Teller (BET) theory was employed to determine the primarily specific surface area. The pore size and size distribution of the materials were calculated by the Barrett-Joyner-Halenda (BJH) method. Field Emission Scanning Electron Microscopy (FE-SEM, EDS, Tescan Mira3 Model) and Transmission Electron Microscopy (TEM, Philips EM208S) were employed to characterize materials morphology and chemical composition.

2.5. Electrochemical measurement

Electrochemical studies including Cyclic Voltammetry (CV) and Galvanostatic Charge-Discharge (GCD) were conducted at room temperature using an Origaflex Potentiostat/Galvanostat (OGF 500). The electrochemical measurements were conducted on a three-electrode system in 6 M KOH solution using a saturated calomel and Pt plate as reference and counter electrodes, respectively. In order to prepare working electrode, MIL-53(Fe) and Pd/MIL-53(Fe) were mixed with carbon black and Poly Vinylidine Difluoride (PVDF) at a mass ratio of 75:20:5 in NMP (N-Methyl-2-pyrrolidone) solution. Then, the mixture was homogenized by ultrasonication. After that, resultant slurry was sprayed on a nickel foam substratum with a mass load of ~1 mg/cm^2. The prepared electrodes were dried at 60 °C.

3. RESULTS AND DISCUSSION

The crystal structure of the as-prepared pure MIL-53(Fe) and Pd/MIL-53(Fe) composites is examined with X-ray diffraction (Fig. 1a). The characteristic peaks are at2θ = 10.53, 12.83, 14.61, 20.25, 21.41, 29.47, which confirm the well synthesis of MIL-53(Fe) due to being similar to those reported for standard MIL-53(Fe) [25]. The XRD pattern of Pd/MIL-53(Fe) shows that following the entrance of palladium to the system, the crystal structure of MIL-53(Fe) remains unchanged and peaks at 2θ of 14.61, 21.41, 29.47 decrease in intensity, thus attributing to loading of Pd nanoparticle on the MOF. N_2 adsorption–desorption isotherms of MIL-53(Fe) and Pd/MIL-53(Fe) (Fig. 1b) were employed to apply BET

theory for the determination of their specific surface area. MIL-53(Fe) and Pd/MIL-53(Fe) specific surface areas were found to be 12.8 and 16.4 m^2/g, respectively, showing an increase in the specific surface area of MIL-53(Fe) in the presence of palladium.

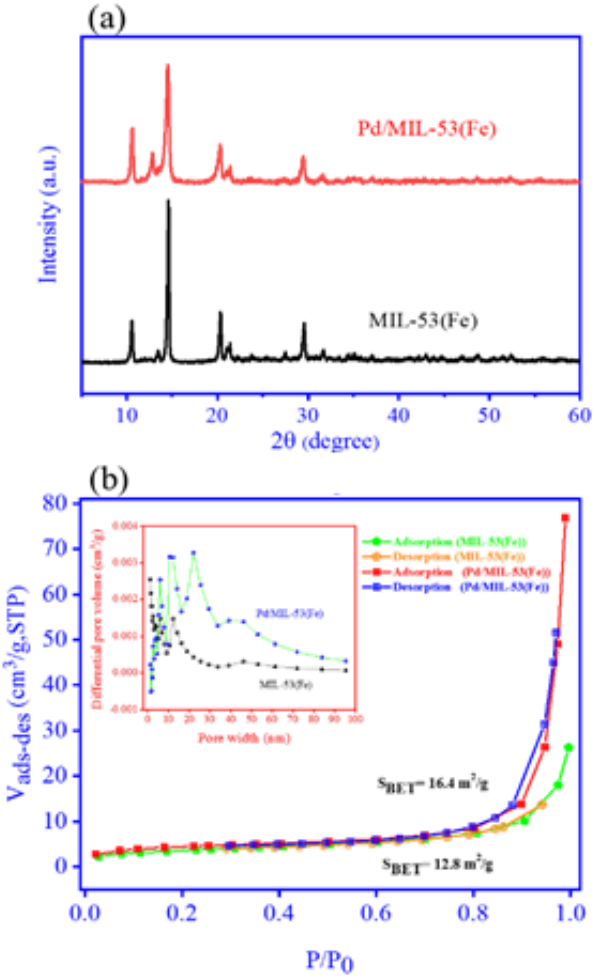

Figure 1. (a) XRD patterns of MIL-53(Fe) and Pd/MIL-53(Fe) and (b) BET isotherms and BJH (inset) of MIL-53(Fe) and Pd/MIL-53(Fe)

As seen in Fig. 1b, the adsorption and desorption branches of MIL-53(Fe) specify the presence of slit-like pores between sheets by sloping and covering a fairly wide range of P/P0 underlying the type-II isotherm with type-H3 hysteresis. The adsorption and desorption branches of Pd/MIL-53(Fe) are parallel and almost vertical corresponding to a hysteresis of type H1, which arises from a material with normal, even pores without interconnecting channels. These findings are in good agreement with the SEM image, demonstrating partly sheets and partly agglomerated particles. In Fig. 1b (inset), the BJH pore size distribution analysis reveals that these two samples have a generally meso-porous structure and only a limited number of pores with a size of less than 1 nm are present. Morphological analyses of as-synthesized materials are performed. Figs. 2a and 2b show SEM images of MIL-53(Fe) and Pd/MIL-53(Fe) composite.

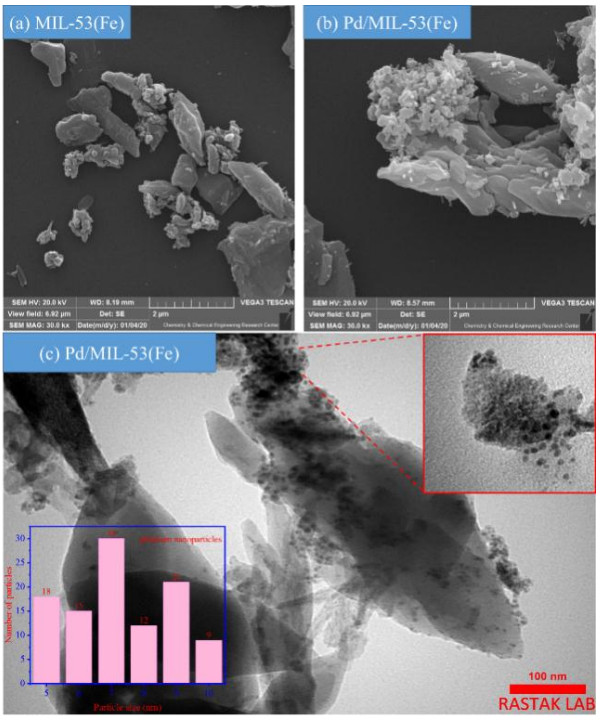

Figure 2. SEM image of (a) MIL-53(Fe), (b) Pd/MIL-53(Fe), and (c) TEM image of Pd/MIL-53(Fe)

As shown in Figs. 2a and 2b, the morphology of both samples is composed of partly sheets, agglomerated nanoparticle, and leaf-like structure with a dimension of 200 nm to 2 µm. For investigating the presence of palladium nanoparticles, the TEM analysis is employed in Figure 2c. According to the nanoparticles of Pd with a size under 20 nm, the MIL-53(Fe) was well decorated. The EDS spectrum of both samples is given in Figs. 3a and 3b.

Figure 3a confirms the XRD analysis and well synthesis of MOFs by elemental analysis. The presence of Cl beside other elements in Pd/MIL-53(Fe) in Fig. 3b might be attributed to the precursor of palladium. The atomic percentage of each element is given in Figures 3a and b. Another characterization was utilized to confirm the TEM image and presence of Pd in Pd/MIL-53(Fe). Atomic absorption spectroscopy confirms the 0.3 % of Pd in Pd/MIL-53(Fe).

The electrochemical performance of as-prepared MIL-53(Fe) and Pd/MIL-53(Fe) was employed to investigate the capacitive behavior of electrode materials with three-electrode cells using CV measurement in 6M KOH solution at room temperature. Fig. 4a and 4b represents the CV curves of MIL-53(Fe) and Pd/MIL-53(Fe) at different scan rates (in the range of 10–200 mV/s) in the −1 to 0 V potential window.

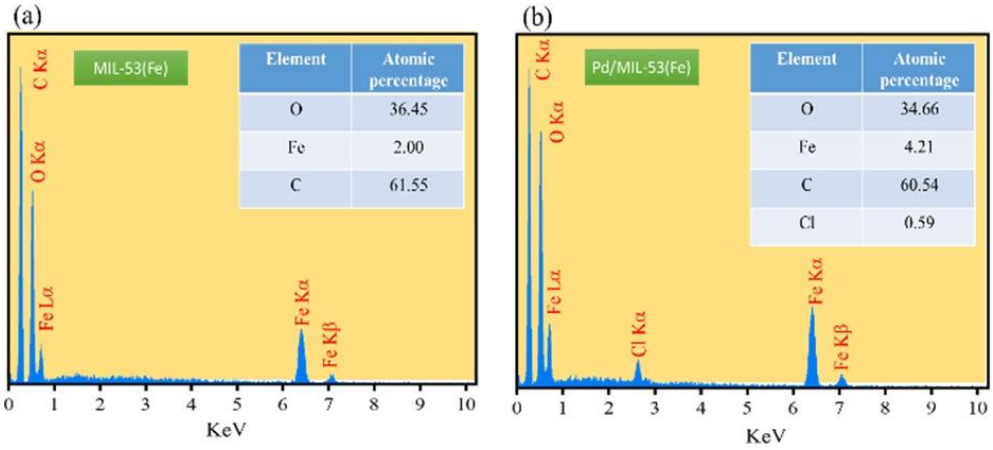

Figure 3. EDS spectrum of (a) MIL-53(Fe) and (b) Pd/MIL-53(Fe)

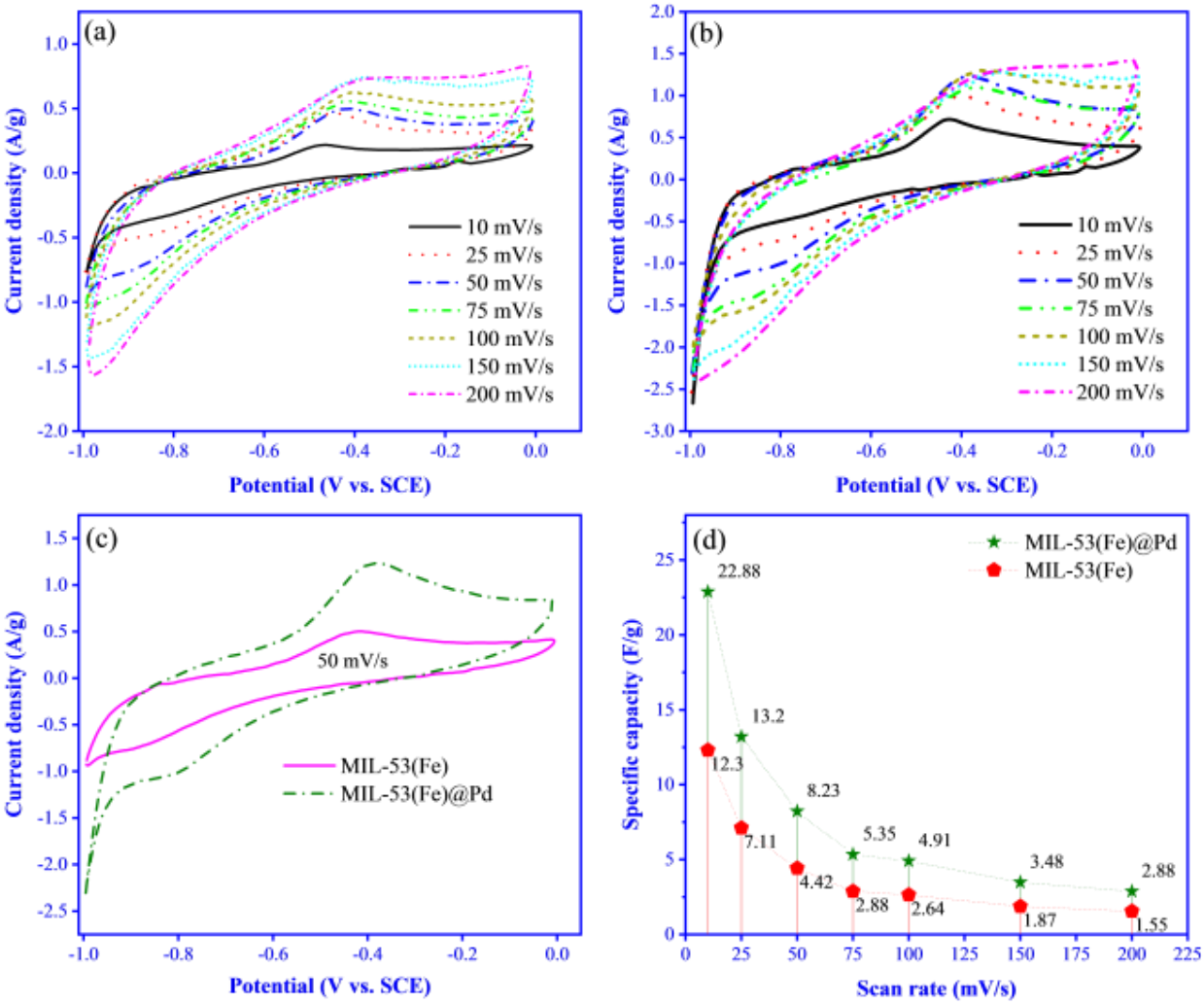

Figure 4. CV curve of (a) MIL-53(Fe) and (b) Pd/MIL-53(Fe) electrodes at different scan rate; (c) CV curve of MIL-53(Fe) and Pd/MIL-53(Fe) electrodes at a scan rate of 50 mV/s; (c) Specific capacitance of electrode materials at different scan rate from 10 to 200 mV/s

In the CV curves, both EDLC and Faradaic redox reactions control the capacitance characteristics. Contribution of EDLC can be inferred in the potential between -1 and -0.6 V from the curve of the CV with a partly rectangular structure. Furthermore, by increasing the scan rate, the cathodic peak shifted to negative potentials and the anodic peak shifted to positive potentials, which confirms that the redox processes take place easier in the nanocomposite samples. The characteristic of the reversible faradic conversion is Fe^{3+}/Fe^{2+} in MIL-53(Fe) and Pd/Pd^{2+} - Fe^{3+}/Fe^{2+} in Pd/MIL-53(Fe). Fig. 4c shows comparative CV curves for MIL-53(Fe) and Pd/MIL-53(Fe) composite electrodes at a scan rate of 50mV/s. CV curve of bare MIL-53(Fe) electrode is much narrower than the composite electrode. Higher capacitance of the composite electrode than MIL-53(Fe) electrode indicates the influence of palladium in composite with its redox reaction on electrochemical performance of MIL-53(Fe). Finally, the specific capacity of both samples according to Equation (1) was calculated and the plot of their specific capacity against scan rate is depicted in Figure 4d. The specific capacitance of the electrode was calculated from the CV curves according to following Equations [5]:

$$C_s = \int_{Va}^{Vc} \frac{IdV}{[(v \times (V_a - V_c) \times m)]} \quad (1)$$

where ∫ IdV denotes the integrated area under the CV plot loop, Cs represents the specific capacitance (F/g), υ corresponds to the scan rate (mV/s), (Va− Vc) shows the potential window (V), and m is the mass of active material. The Pd/MIL-53(Fe) has a specific capacity of 20.88 in 10 mV/s which is close to twice the value of MIL-53(Fe).

Galvanostatic Charge-Discharge (GCD) measurements were carried out at current densities of 0.5 A/g in order to assess the electrochemical performance and capacitance behavior of both electrodes. Figure 5a shows the comparison of GCD curves of MIL-53(Fe) and Pd/MIL-53(Fe) in the potential window between -1 and 0 V at current densities of 0.5 A/g. GCD curves possessed the platforms, showing that the capacitance is mostly governed by EDLC behavior of both samples by steep slope in the discharge section.

In addition, Pd/MIL-53(Fe) has a couple platform that can be related to the pseudocapacitive property that appears with the presence of palladium in composite as reflected in CV curves. The specific capacitance is also calculated through the following equation [5]:

$$C_s = \frac{I \times \Delta t}{m \times \Delta V} \quad (2)$$

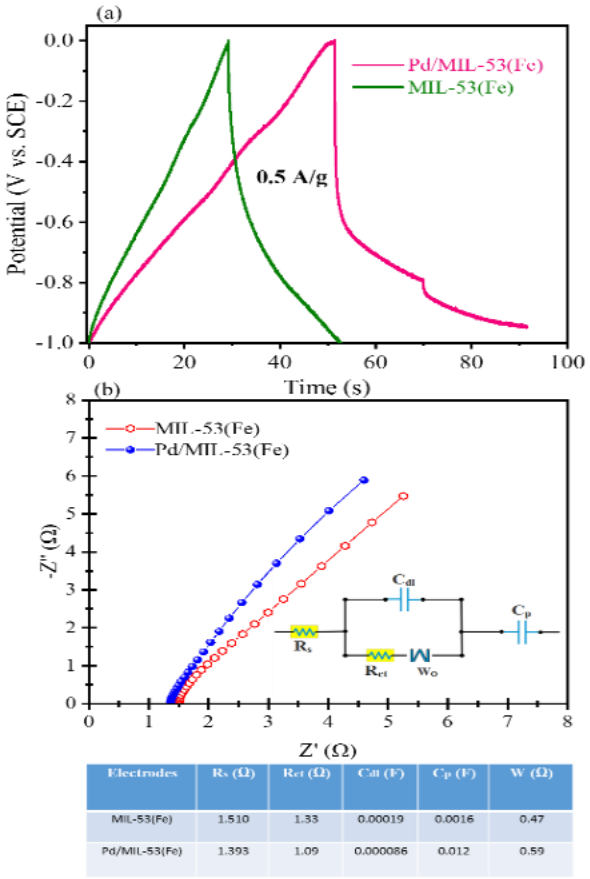

Electrodes	Rs (Ω)	Rct (Ω)	Cdl (F)	Cp (F)	W (Ω)
MIL-53(Fe)	1.510	1.33	0.00019	0.0016	0.47
Pd/MIL-53(Fe)	1.393	1.09	0.000086	0.012	0.59

Figure 5. (a) The comparison GCDs curves of MIL-53(Fe) and Pd/MIL-53(Fe) electrodes at current density of 0.5 A/g; (b) Impedance Nyquist plots at open circuit potential and the Electrical parameters of equivalent circuit

The specific capacity values of 10.1 and 19.9 F/g were achieved for MIL-53(Fe) and Pd/MIL-53(Fe), respectively. Also, the relation between capacitance of both electrodes and different current densities is reported in Fig. 6.

Electrochemical Impedance Spectroscopy (EIS) was employed to study the characteristic frequency response of MIL-53(Fe) and Pd/MIL-53(Fe) to investigate the interfacial kinetics of the electrochemical system. Figure 5b shows the Nyquist plots observed in the frequency range of 0.01 Hz to 100 kHz for samples with fitting circuit and widening semicircle area. The equivalent series resistance (Rs) values for MIL-53(Fe) and Pd/MIL-53(Fe) electrodes were determined at about 1.51 and 1.39 Ω. The diameter of the semicircle was related to the resistance of the charge transfer (Rct) and Pd/MIL-53(Fe) exhibited lower R_{ct} than MIL-53(Fe), which could be due to the good performance of its electron transport. Other values of the EIS fitting parameters are given in

Figure 5b. Pd/MIL-53(Fe) with a higher specific surface and higher conductivity of Pd nanoparticles improved the MOF efficiency by facilitating the diffusion of electrolytes and accelerating the transport of electrons.

The presence of palladium improved the electrochemical efficiency of bare MOFs by increasing the specific surface area and it yielded a larger number of active sites within the pores for quick electrochemical reactions. Also, it promoted the ions or electrons transfer at the electrolyte-electrode interface. Moreover, the presence of Pd in the redox reaction improved the capacitance behavior of the electrode.

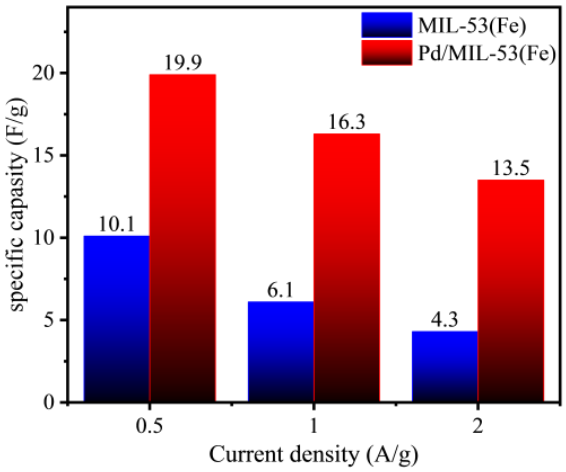

Figure 6. Relation of capacitance with current density

4. Conclusion

In summary, a simple strategy was used for the preparation and design of Pd/MIL-53(Fe) at room temperature. The TEM and Atomic absorption spectroscopy confirmed the loading of nanoparticle of Pd on the MOF. The electrochemical properties strongly depend on the CV cycles. The resulting Pd/MIL-53(Fe) demonstrated improved electrochemical efficiency compared to the bare MOF of MIL-53(Fe) by improving the specific surface area and further redox sites by joining palladium to redox reaction and doubling the specific capacity to 20.88 F/g. This work emphasizes the importance of optimizing the development and design of new materials such as MOFs.

ACKNOWLEDGEMENT

The present study was suported by Materials and Energy Research Center (MERC) through grant No 300647.

REFERENCES

1. Wang, Y. S., Chen, Y. C., Li, J. H., Kung, C. W., "Toward Metal–Organic-Framework-Based Supercapacitors: Room-Temperature Synthesis of Electrically Conducting MOF-Based Nanocomposites Decorated with Redox-Active Manganese", ***European Journal of Inorganic Chemistry***, Vol. 2019, No. 26, (2019), 3036-3044. https://doi.org/10.1002/ejic.201900676
2. Li, B., Wen, H. M., Cui, Y., Zhou, W., Qian, G., Chen, B., "Emerging multifunctional metal–organic framework materials ", ***Advanced Materials***, Vol. 28, No. 40, (2016), 8819-8860. https://doi.org/10.1002/adma.201601133
3. Lu, G., Li, S., Guo, Z., Farha, O. K., Hauser, B. G., Qi, X., Wang, Y., Wang, X., Han, S., Liu, X., DuChene, J. S., "Imparting functionality to a metal–organic framework material by controlled nanoparticle encapsulation", ***Nature Chemistry***, Vol. 4, No. 4, (2012), 310-316. https://doi.org/10.1038/nchem.1272
4. Chameh, B., Moradi, M., Hessari, F. A., "Decoration of metal organic frameworks with Fe_2O_3 for enhancing electrochemical performance of ZIF-(67 and 8) in energy storage application", ***Synthetic Metals***, Vol. 269, (2020), 116540. https://doi.org/10.1016/j.synthmet.2020.116540
5. Chameh, B., Moradi, M., Kaveian, S., "Synthesis of hybrid ZIF-derived binary ZnS/CoS composite as high areal-capacitance supercapacitor", ***Synthetic Metals***, Vol. 260, (2020), 116262. https://doi.org/10.1016/j.synthmet.2019.116262
6. Deng, T., Zhang, W., Arcelus, O., Wang, D., Shi, X., Zhang, X., Carrasco, J., Rojo, T., Zheng, W., "Vertically co-oriented two dimensional metal-organic frameworks for packaging enhanced supercapacitive", ***Communications Chemistry***, Vol. 1, No. 1, (2018), 1-9. https://doi.org/10.1038/s42004-017-0005-8
7. Farha, O. K., Eryazici, I., Jeong, N. C., Hauser, B. G., Wilmer, C. E., Sarjeant, A. A., Snurr, R. Q., Nguyen, S. T., Yazaydin, A. O., Hupp, J. T., "Metal–Organic Framework Materials with Ultrahigh Surface Areas: Is the Sky the Limit?", ***Journal of the American Chemical Society***, Vol. 134, No. 36, (2012), 15016-15021. https://doi.org/10.1021/ja3055639
8. Rodenas, T., Luz, I., Prieto, G., Seoane, B., Miro, H., Corma, A., Kapteijn, F., i Xamena, F. X. L., Gascon, J., "Metal–organic framework nanosheets in polymer composite materials for gas separation", ***Nature Materials***, Vol. 14, No. 1, (2015), 48-55. https://doi.org/10.1038/nmat4113
9. Corma, A., García, H., Llabrés i Xamena, F. X., "Engineering metal organic frameworks for heterogeneous catalysis", ***Chemical reviews***, Vol. 110, No. 8, (2010), 4606-4655. https://doi.org/10.1021/cr9003924
10. Horcajada, P., Chalati, T., Serre, C., Gillet, B., Sebrie, C., Baati, T., Eubank, J. F., Heurtaux, D., Clayette, P., Kreuz, C., Chang, J. S., "Porous metal–organic-framework nanoscale carriers as a potential platform for drug delivery and imaging", ***Nature Materials***, Vol. 9, No. 2, (2010), 172-178. https://doi.org/10.1038/nmat2608
11. Liu, Y. P., Zhao, S. F., Guo, S. X., Bond, A. M., Zhang, J., Zhu, G., Hill, C. L., Geletii, Y. V., "Electrooxidation of Ethanol and Methanol Using the Molecular Catalyst [{Ru4O4(OH)2(H2O)4}(γ-SiW10O36)2]10–", ***Journal of the American Chemical Society***, Vol. 138, No. 8, (2016), 2617-2628. https://doi.org/10.1021/jacs.5b11408
12. Deng, T., Lu, Y., Zhang, W., Sui, M., Shi, X., Wang, D., Zheng, W., "Inverted Design for High-Performance Supercapacitor Via $Co(OH)_2$-Derived Highly Oriented MOF Electrodes", ***Advanced Energy Materials***, Vol. 8, No. 7, (2018), 1702294. https://doi.org/10.1002/aenm.201702294
13. Chui, S. S. Y., Lo, S. M. F., Charmant, J. P., Orpen, A. G., Williams, I. D., "A Chemically Functionalizable Nanoporous Material $[Cu_3(TMA)_2(H_2O)_3]_n$", **Science**, Vol. 283, No. 5405, (1999), 1148-1150. https://doi.org/10.1126/science.283.5405.1148
14. Wang, L., Han, Y., Feng, X., Zhou, J., Qi, P., Wang, B.,"Metal–organic frameworks for energy storage: Batteries and

supercapacitors", ***Coordination Chemistry Reviews***, Vol 307, (2016), 361-381. https://doi.org/10.1016/j.ccr.2015.09.002
15. Hu, J., Wu, X., Zhang, Q., Gao, M., Qiu, H., Huang, K., Feng, S., Wang, T., Yang, Y., Liu, Z., Zhao, B., "Highly active PdNi/RGO/polyoxometalate nanocomposite electrocatalyst for alcohol oxidation", ***Langmuir***, Vol. 34, No. 8, (2018), 2685-2691. https://doi.org/10.1021/acs.langmuir.7b04031
16. Yan, Y., Wang, T., Li, X., Pang, H., Xue, H., "Noble metal-based materials in high-performance supercapacitors", ***Inorganic Chemistry Frontiers***, Vol. 4, No. 1, (2017), 33-51. https://doi.org/10.1039/c6qi00199h
17. Mensing, J. P., Lomas, T., Tuantranont, A.,"Ammonia strengthened graphene/CNT-wrapped polyaniline-nanofiber composites loaded with palladium nanoparticles for coin cell supercapacitors", ***Electrochimica Acta***, Vol. 263, (2018), 17-25. https://doi.org/10.1016/j.electacta.2017.12.193
18. Orooji, Y., Ghanbari, M., Amiri, O., Salavati-Niasari, M.,"Facile fabrication of silver iodide/graphitic carbon nitride nanocomposites by notable photo-catalytic performance through sunlight and antimicrobial activity", ***Journal of Hazardous Materials***, Vol. 389, (2020), 122079. https://doi.org/10.1016/j.jhazmat.2020.122079
19. Ghanbari, M., Salavati-Niasari, M.,"Tl_4CdI_6 nanostructures: facile sonochemical synthesis and photocatalytic activity for removal of organic dyes", ***Inorganic Chemistry***, Vol. 57, No. 18, (2018), 11443-11455. https://doi.org/10.1021/acs.inorgchem.8b01293
20. Karami, M., Ghanbari, M., Amiri, O., Salavati-Niasari, M., "Enhanced antibacterial activity and photocatalytic degradation of organic dyes under visible light using cesium lead iodide perovskite nanostructures prepared by hydrothermal method", ***Separation and Purification Technology***, Vol. 253, (2020), 117526. https://doi.org/10.1016/j.seppur.2020.117526
21. Gholamrezaei, S., Amiri, M., Amiri, O., Salavati-Niasari, M., Moayedi, H., "Ultrasound-accelerated synthesis of uniform $SrMnO_3$ nanoparticles as water-oxidizing catalysts for water splitting systems", ***Ultrasonics Sonochemistry***, Vol. 62, (2020), 104899. https://doi.org/10.1016/j.ultsonch.2019.104899
22. Tian, X. X., Gholamrezaei, S., Amiri, O., Ghanbari, M., Dashtbozorg, A., Salavati-Niasari, M., "Zn_2MnO_4/ZnO nanocomposites: One step sonochemical fabrication and demonstration as a novel catalyst in water splitting reaction", ***Ceramics International***, Vol. 46, No. 16, (2020), 25789-25801. https://doi.org/10.1016/j.ceramint.2020.07.058
23. Sabo, M., Henschel, A., Fröde, H., Klemm, E., Kaskel, S., "Solution infiltration of palladium into MOF-5: synthesis, physisorption and catalytic properties", ***Journal of Materials Chemistry***, Vol. 17, No. 36, (2007), 3827-3832. https://doi.org/10.1039/b706432b
24. Ishida, T., Nagaoka, M., Akita, T., Haruta, M., "Deposition of gold clusters on porous coordination polymers by solid grinding and their catalytic activity in aerobic oxidation of alcohols", ***Chemistry–A European Journal***, Vol. 14, No. 28, (2008), 8456-8460. https://doi.org/10.1002/chem.200800980
25. Zhang, Y., Li, G., Lu, H., Lv, Q., Sun, Z., "Synthesis, characterization and photocatalytic properties of MIL-53 (Fe)–graphene hybrid materials", ***RSC Advances***, Vol. 4, No. 15, (2014), 7594-7600. https://doi.org/10.1039/c3ra46706f

Advanced Ceramics Progress: Vol. 7, No. 1, (Winter 2021) 18-24

Advanced Ceramics Progress

Research Article

Journal Homepage: www.acerp.ir

Optimization of Heat Treatment Cycles in Sub-atmospheric LiF-NaF-KF Based Fluoride Ion Cleaning for Removing Oxide Layers in Cracks of IN738-LC

S. Hamidi [a], M.R. Rahimipour [a], M.J. Eshraghi [b] *, H. Esfahani [c]

[a] *Department of Ceramics, Materials and Energy Research Center (MERC), Meshkindasht, Alborz, Iran*
[b] *Department of Semiconductors, Materials and Energy Research Center (MERC), Meshkin Dasht, Alborz, Iran*
[c] *Department of Materials Engineering, Bu-Ali Sina University, Hamedan, Hamedan, Iran*

ARTICLE INFO

Article History:

Received 4 November 2020
Received in revised form 7 December 2020
Accepted 13 December 2020

Keywords:

Alkaline Fluoride Salts
Cleaning
Micrograph
Oxide Films
Superalloy
Cracks

ABSTRACT

An improved Fluoride Ion Cleaning (FIC) process required for removing all oxide layers by a molten mixture of alkaline fluoride salts under sub-atmospheric pressure was developed and applied to oxide layers on the cracks formed on the surface of Inconel 738-LC samples. This method is directly characterized by filling up the cracks with a molten mixture of alkaline fluoride salts (LiF-NaF-KF) overheated under sub-atmospheric pressure and subsequently, by injecting hot hydrogen gas into the process chamber. The effect of cleaning time on the microstructure of the finished surface was studied in time durations up to 120 min in intervals of 30 min using cross-sectional micrographs and elemental distribution maps. In accordance with the amount of mass loss and microstructural studies during the cleaning process, the optimum cleaning time was suggested to be 90-120 min. Perquisite microstructural outcome shows that in the suggested cleaning condition, all oxide scales in the cracks would be removed without any extra damage to the gamma prime depleted layer, which is a necessary layer for preventing sample oxidation before repair. In this regard, subsequent brazing operations need an oxide-free surface.

https://doi.org/10.30501/ACP.2021.251522.1046

1. INTRODUCTION

Nickel-based superalloys are known for their mechanical strength and high corrosion resistance at high temperatures which would cause fatigue micro-cracks [1,2]. On the contrary, the relatively high-temperature oxidation resistance of these superalloys is due to the formation of dense oxides of Cr_2O_3, TiO_2, Al_2O_3, and $NiCr_2O_4$ spinel [3,4]. To reuse these superalloys, it is necessary to perform an expansive process of removing oxide films formed on the surface, especially those created in the micro-cracks.

Fluoride compounds are widely used as chemical agents for removing ceramic oxide layers due to their high chemical reactivity and electronegativity [5]. There are three common types of Fluoride Ion Cleaning (FIC) methods for removing the oxide films: (i) chrome fluoride-based systems such as CrF_3 and NH_4F + Cr; (ii) fluorocarbon-based systems such as PTFE; and (iii) mixed gas systems such as HF and H_2 [6-8]. In 1991, Kim et al. [9] proposed a variation of the FIC process in which cleaning was performed at sub-atmospheric pressure by injecting HF gas into the process chamber. They showed that upon reducing the chamber pressure to sub-atmospheric levels before HF injection, deep penetration of the reductant gases into the cracks would increase that results in the oxide film removal. In 2006, Miglietti et al. [10] used the thermal decomposition of Poly Tetra Fluoro Ethylene (PTFE) grease in the atmosphere in order to clean the superalloy oxides. They detected concentrated

* Corresponding Author Email: eshr56@gmail.com (M. J. Eshraghi)

http://www.acerp.ir/article_128023.html

Please cite this article as: Hamidi, S., Rahimipour, M. R., Eshraghi, M. J., Esfahani, H., "Optimization of Heat Treatment Cycles in Sub-atmospheric LiF-NaF-KF Based Fluoride Ion Cleaning for Removing Oxide Layers in Cracks of IN738-LC", ***Advanced Ceramics Progress***, Vol. 7, No. 1, (2021), 18-25. https://doi.org/10.30501/ACP.2021.251522.1046

oxygen in the specimen surface after the cleaning process. According to their study, the gas-based method enjoys several benefits including precise process controllability and risk assessment with regard to hazardous HF gas; however, its disadvantages such as process complexity and high instrument costs give industries and researchers the incentive to look for safer and less expensive methods.

Therefore, the development of the promoted methods with less complexity and hazards than gas-based methods for removing oxides from the narrow cracks is still desirable. The proposed method in this research comprises a combination of processes for both solid- and gas-based methods. To this end, the present study proposes a new method by implementing the following three stages: (i) filling up the cracks with alkaline fluoride salts after the cleaning process in a clean environment, (ii) heating up the process in a clean chamber in sub-atmospheric pressure up to the melting point of alkaline fluoride salts, and (iii) injecting hydrogen at atmospheric pressure. The proposed method for cleaning cracks in this study is a combination of pressure reduction and molten fluorine salt in addition to hydrogen injection in the chamber during the process. Among the advantages of such a method are the safety and environmentally friendliness of alkaline fluoride salts in comparison to HF gas used in the usual FIC process. Reducing the temperature during the process is also beneficial since high temperature would cause damage to the gamma prime depletion layer and structural disorder [11]. Therefore, using salts at a low melting point facilitates the remaining alloy composition and phases during the process that is done in reducing the atmosphere. In order to achieve a low melting point, low viscosity, and low volatility salts, the ternary systems of alkaline fluoride salts were taken. According to the literature [12-14], the eutectic mixture of three fluoride salts (29.3 % LiF-11.6 % NaF- 59.1 % KF (wt. %)) at a melting point of 454˚C was chosen, being well suited for the temperature range for the proposed desired method.

The novlty of this research lies in its usage of a less hazardous solid fluoride source used in the vacuum chamber. As mentioned earlier, performing the process with a reduced pressure could improve the penetration of the molten fluorine salt into the cracks and help remove oxides in the depth of cracks. In addition, introducing hydrogen which is a reducing agent and acts as an activator for fluorine salt to produce hydrogen fluoride gas at the local positions is another key factor associated with the proposed method. To the best of the authors' knowledge, there has been no report on injecting hydrogen gas to a vacuum chamber to simultaneously perform the FIC process via molten fluoride salts. Another benefit of this method is that using fluoride salts on the local oxide scales leaves other parts unattacked. However, the flow of hydrogen in the chamber removes the reaction byproducts and allows newly generated hydrogen fluoride to act on the remaining oxide. As mentioned earlier, the FIC process was completed in Stage (iii) and for optimization, the experimental condition in Stages (i) and (ii) was fixed; however, the effects of soaking time in Stage (iii) on removing oxides from the cracks were systematically investigated using cross-sectional micrographs and elemental distribution maps.

2. MATERIALS AND METHODS

2.1. Sample and Crack Preparation

The chemical composition of the selected alloy (IN-738LC) is reported in Table 1. Specimens were prepared in a plate with dimensions of 10 mm × 10 mm × 4 mm. Microcracks were formed by an NC wire Electro-Discharge Machining (EDM). The surfaces of the samples were polished using 600 up to 2000 grades of SiC paper and subsequently, sonicated in acetone for 15 minutes to clean the surface from SiC polishing contamination. According to our previous study on oxidation kinetics [14], the oxidation at 950 °C over 160 hours does not tend to form an oxide layer with a much higher thickness on top of Ni-based superalloy. Therefore, the oxide layers were formed by holding samples at 950 °C in the ambient atmosphere for 160 hours.

TABLE 1. Chemical composition of superalloy used in this study

Elemental	Ni	Cr	Co	Ti	Al
wt. %	Base	15	9.5	3.6	3.5
Elemental	W	Mo	Ta	Nb	C
wt. %	3.2	1.7	1.5	1.0	0.1

2.2. Cleaning procedure

The cleaning procedure begins in Stage (i) in which the samples are embedded in a 4g mixture of alkaline fluoride salts as a chemical reactant. This salt comprises LiF (Merck No.: 232-152, purity ≥ 99.99 %), NaF (Merck No.: 231-667-8, purity ≥ 99.5 %), and KF (Merck No.: 232-151-5, purity ≥ 99.0 %) at ratios of 29.3, 11.6, and 59.1 (wt. %), respectively. This ratio has been chosen as FLiNaK for its low melting temperature [15].

Stage (ii) begins by inserting the sample in the reactor and reducing the pressure of the reactor to 3×10^{-3} mbar, while simultaneously increasing the reactor temperature up to 500 °C. In this stage, the alkaline salt is melted and encapsulated in the sample and it fills the cracks. While the reactor is enriched by F- atoms during heat treatment, there is high affinity to other elements that could be formed [16]. Finally, heat treatment continues upon increasing the reactor temperature up to 950 °C and

increasing the reactor pressure up to the atmosphere by injecting hydrogen gas. After finishing the dedicated thermo-chemical regime, the furnace is cooled down to room temperature in a hydrogen atmosphere.

To investigate the effectiveness of the aforementioned procedure in the quality of surface and crack cleaning, samples were analyzed after 30, 90, 60, and 120 min of heat treatment. The samples removed from the furnace were immersed in 0.5 M sulfuric acid for 20 min to wash out the reaction products and by-products from the cracks. The parameters used in Stages (ii) and (iii) are presented in Table 2.

TABLE 2. Time schedule cleaning cycle

Stage	Temperature (°C)	Heating Rate (°C.h^{-1})	Time (min)
(ii)	25-500	600	47.5
(iii)	500-700	150	80
(iii)	700-950	300	30
(iii)	950	-	30,60,90,120

2.3. Characterization

The mass change of the samples after cleaning was measured using a high-precision balance with the accuracy of ± 0.01 milligrams at 23 ± 2 ˚C. The cross-section of the sample was electrolytically polished with a 12 mL H_3PO_4, 47 ml H_2SO_4, and 16ml CrO_3 solution by applying 3V polarization for 3 s [14]. The phases formed on the surface were analyzed before and after oxidation by X-ray diffractometry (Siemens Model; D500 using Cu-kα radiation). X'pert HighScore Plus software (2.2b) was used to identify these phases. The concentration profiles across the cracks before and after cleaning procedures were examined by Energy Dispersive X-ray Spectrometry (EDS) using spot scan mode in FESEM (model T-scan by 15 kV accelerating voltage). To study the micrographs ImageJ, 1.38x NIH USA was employed.

3. RESULTS AND DISCUSSION

3.1. Characterization of oxide film

Figure 1 presents the X-ray diffraction patterns of samples before and after oxidation at 950 ˚C for 160 h. The XRD pattern of the oxidized sample shows that in the oxide layers, not only single oxide phases such as Al_2O_3 (standard JCPDS card 00-004-0875) Cr_2O_3 (standard JCPDS card 00-038-1479) and a small amount of TiO_2 (standard JCPDS card 01-072-1148) were formed, but also complex oxides such as $NiAl_2O_4$ (standard JCPDS card 00-010-0339) and $NiCr_2O_4$ (standard JCPDS card 00-023-1271) were presented [14].

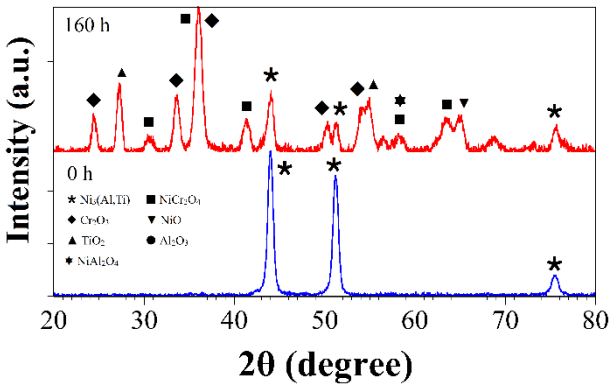

Figure 1. X-ray diffraction patterns of IN-738LC (a) before and (b) after oxidation in air at 950°C for 160 h

Figure 2 shows the microstructural and elemental maps of a typical crack in a sample oxidized at 950 ˚C for 160 h. The fine dot-like feature at the interior depth is attributed to the gamma prime phase [17,18]. This morphology is different in the region near the surface due to the rearrangement of alloy elements during oxidation. The decomposition of gamma prime occurred due to the outward diffusion of Ti and Al to the surface and their reaction with oxygen to form selective oxidation. Furthermore, elemental maps indicate migration of Al, Cr, and Ti alloy elements from different depths and concentrations in the region near the surface. Each element concentrated at a specific distance from the surface can be observed in the regular formation of oxide components during oxidation.

According to the overlay elemental map analysis of the layers, the outer layer mainly consists of TiO_2, Al_2O_3, and small amount of NiO, and the inner layer is composed of Cr_2O_3. However, $NiCr_2O_4$ spinel phase is formed between the outer and inner layers, i.e., the middle layer. Al maps with EDS analysis confirm the formation of Al_2O_3 as the innermost layer because of the higher tendency of aluminum to react with oxygen rather than other elements of the alloy [19, 20].

A relatively thick area is also located between the substrate and internal layers attributed to the gamma prime depleted zone. By extending the oxidation time, elements such as Ni, Cr, and Ti would continue to migrate from these regions to the outer layer to form oxide compounds.

3.2. Cleaning the oxide from the surface of the crack

Figure 3 shows the cross-section micrographs from the cracks of the oxidized samples obtained by an optical microscope and the samples were cleaned for 90 min in the modified FIC process. According to this micrograph,

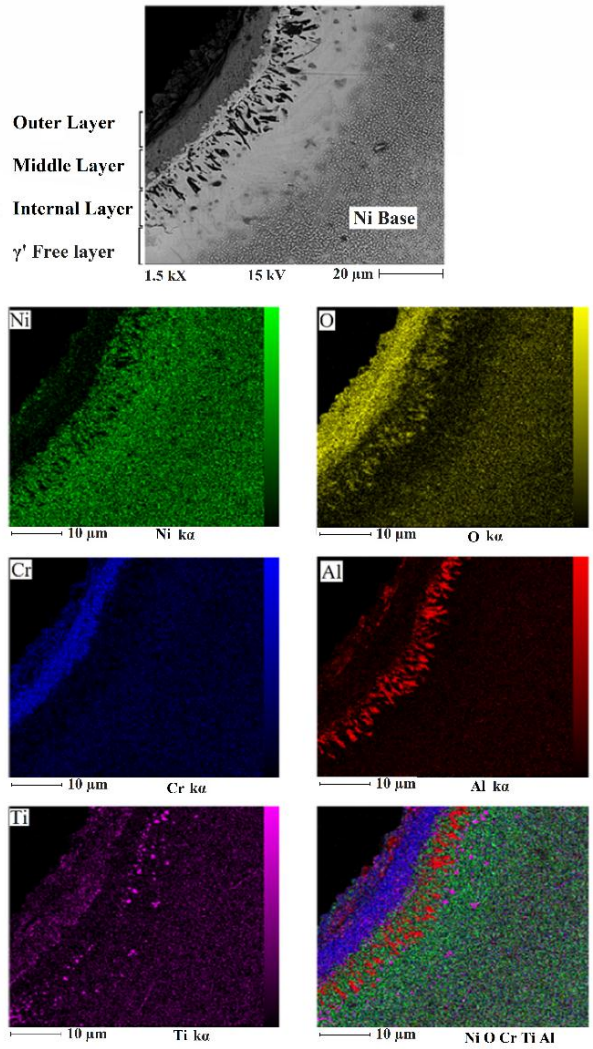

Figure 2. Elemental distribution map of a typical crack in a sample oxidized at 950 ˚C for 160 h

the alkaline fluoride salts were removed from the crack surface after completion of stage (iii) of the FIC process. The obtained results showed that alkaline salt could be melted, encapsulated in the microcracks during the Stage (ii), and then, the cleaning condition would suffice to gasify the alkaline fluoride salts during the Stage (iii). A distinct white layer observed in both samples shows the gamma prime depleted area; however, there is a major difference between the locations of this layer in the cleaned and oxidized samples. Although the gamma prime depleted area for the oxidized sample is placed under the oxidized region, as shown in Figure 2, for the cleaned sample, it is located on the surface. The 90 min FIC process can clean the oxide films and retain a metallic surface without any ceramic phases. However, applying the process for increased duration may expose the sample to more attacks which would result in degradation of the base alloy. Therefore, calculation of the mass loss of the sample during the cleaning process and cross-sectional imaging of surface area play significant roles in determining the optimum duration of the FIC process.

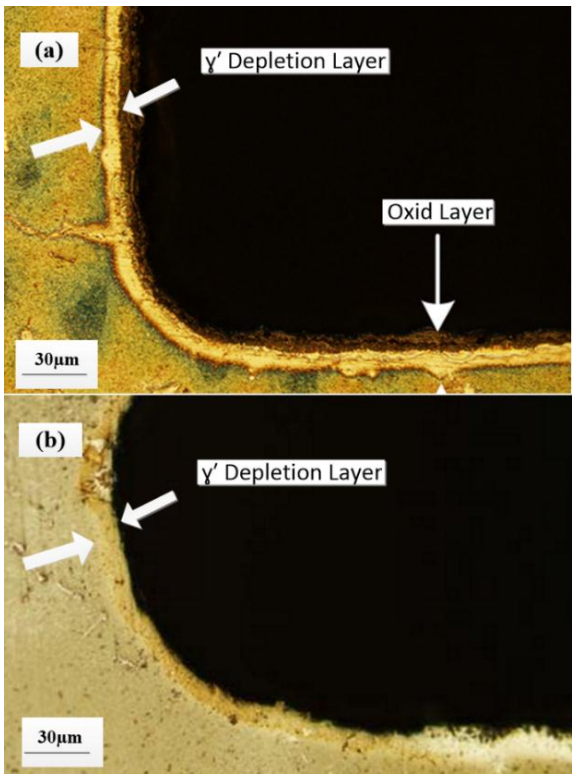

Figure 3. Optical micrographs of (a) sample oxidized for 160 h and (b) sample oxidized and cleaned for 90 min by modified FIC process

After removing the oxide films from the surface, the total mass of the sample is expected to be reduced. Figure 4 shows the mass loss per surface area of IN738 LC during the FIC cleaning process or different durations of 30, 60, 90, and 120 min. According to the mass grain duration and 160 h of oxidation [14] as well as Figure 4, the amount of mass loss increased upon increase in the process duration, indicating the removal of oxide films from the surface and corrosion of the substrate. Since the molten salt would possibly diffuse into the metallic area and degrade alloy elements (Al, Ti) causing damage to the base superalloy, it is necessary to study the cross-sectional image of cleaned samples at various cleaning times to determine the optimum progress of the process.

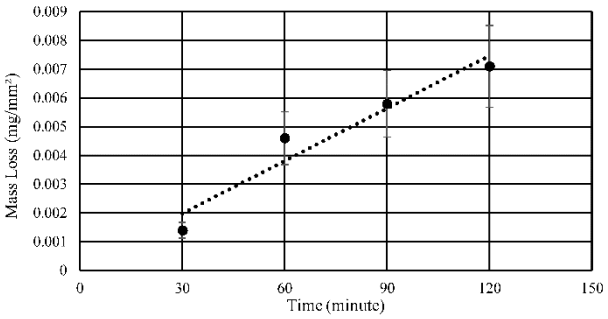

Figure 4. Mass loss per surface area of IN738 LC during FIC cleaning process at 950 °C

The cross-sectional images of a cleaned crack presented in Figure 5 provide significant information on morphology changes during the cleaning process. Figure 5a shows a backscattered electron micrograph of the sample cleaned by the FIC process for 30 min. According to this figure, the FIC process for 30 minutes was not enough to completely remove oxide films; therefore, Cr_2O_3 and Al_2O_3 rich layers corresponding to the middle and internal layers still remained on the surface. According to Figure 5b, increasing the cleaning time to 60 minutes would remove most of the Cr_2O_3 layers. In addition, the number of the dark spots corresponding to Al_2O_3 in the internal layer was reduced to indicate the ability of the salts to diffuse into the sub-layer and clean some of the oxide layers. Most of oxide layers on the surface sample were removed by the process after about 90 minutes with a retaining gamma prime depleted area on top of the samples under the oxide layer (Figure 5c), implying that during the cleaning of the oxides, Ti and Al diffuse outward from the volume into the surface and finally react with the HF, thus deepening the gamma prime depleted area. This depletion promotes the removal of such strong oxide formers near the surface that could boost prevention of oxidation at a stage between cleaning and repairing [21], thus increasing the bonding strength during the repairing process. Increasing the cleaning process up to 120 min would not only remove the entire oxide layer but also clean the gamma prime depleted area (Figure 5d), mainly due to the fact that in the absence of the oxide layer, depleted gamma prime could easily react with salt. It can be concluded that the optimum condition for recovering the samples typically oxidized at 950 ºC for 160 h could be performed at 950 ºC by soaking in H_2 gas in a time period of 90 to 120 min.

As discussed earlier, at the final stage of the FIC process, the alloying elements may diffuse outward and react with HF, and this behavior gains significance while recognizing the optimum conditions for obtaining the desired surface. According to results, in the process of cleaning the samples for 90 minutes by the modified FIC process, the elemental depletion was likely to occur. Figure 6 shows the elemental distribution maps for Ni, Al, Ti, Cr, and O within the region near the surface of the crack cleaned by 90 minutes in the modified FIC process. The elemental map also depicts a uniform distribution for Cr, Al, and Ni.

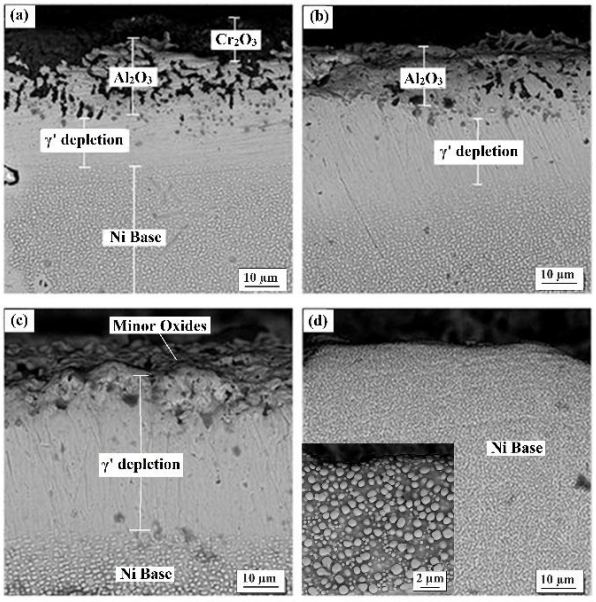

Figure 5. Cross-sectional SEM micrographs of typical crack cleaned by FIC process at 950 ℃ at different times: (a) 30, (b) 60, (c) 90, and (d) 120 min

3.3. Mechanism

The mechanism for the mentioned cleaning procedure, which is a combination of several methods, could be described as follows: In the second stage, fluoride salts reacted with oxide films on the surface at 500 ºC [22]. The salts indirectly reacted with oxide films step by step. In the beginning, Alkaline salts reacted with the remaining H_2O in a pack of salts to form the HF, as shown in the following [23]:

$$LiF_{(l)} + H_2O_{(g)} = Li_2O_{(g)} + 6LiF_{(g)} \quad (1)$$

Then, HF reacted, as shown in Eq. 2, with oxide film to form volatile fluoride elements (e.g. for Al_2O_3). The main residues of HF and surface metal oxides reacted are AlF_3 (g), CrF_3 (s), TiF_4 (g), and H_2O (g) [24]. The resultant H_2O may react again with the remainig salts to form more HF reducer agents [25,26].

$$6HF_{(g)} + Al_2O_{3(s)} = 2ALF_{3(g)} + H_2O_{(g)} \quad (2)$$

Reducing the reactor pressure to sub-atmospheric pressure would make Eq. 1 accelerate in accordance with

the Levine's principle [27]. Therefore, this stage should be performed at a pressure reduced to approximately 1 to 3×10^{-3} mbar. Furthermore, sub-atmospheric pressures forced the gaseous products out of the cracks and were replaced by new HF gas [28]. Therefore, from the thermodynamic point of view, the cleaning process would be accomplished at Stage (ii), in contrast to the kinetic view, suggesting that the cleaning reaction of each oxide could be completed at different times [29].
Stage (iii): To complete the cleaning reactions, H_2 gas was injected into the reactor until the reactor pressure would reach 1013 mbar. The temperature of the reactor was simultaneously increased up to 950 ºC. The injected H_2 gas reacted with the remaining alkaline salts and volatile fluoride element to form an HF cleaning agent, as shown in the following reactions [30]:

$$H_{2(g)} + LiF_{(l)} = HF_{(g)} + LiH_{(g)} \quad (3)$$

$$^3/_2\, H_{2(g)} + AlF_{3(g)} = Al_{(l)} + 3HF_{(g)} \quad (4)$$

The produced HF gas induced and accelerated the Reaction (2), especially for Cr_2O_3 and TiO_2 [26]. Prolonged heating time would result in the reaction of oxides with HF, thus converting them to their volatile fluorides and evaporating the volatile fluorides. In addition, prolonged heating would result in the diffusion of metal alloy elements outwards and surface depletion by HF reactions with strong oxide formers drawn onto the surface by diffusion.

4. CONCLUSION

The process of the modified fluoride ion cleaning using FLiNaK (29.3%LiF-11.6%NaF-59.1%KF (wt. %)) alkaline salt in sub-atmospheric pressures was investigated in this study in order to effectively remove oxides on the artificial cracks of oxidized Inconel samples. In the modified process, FLiNak was directly plugged into the cracks in the powder form before processing. This method was a combination of methods, i.e., pressure reduction and molten fluorine salt in addition to hydrogen injection in the chamber during the process. The study of the effect of FIC process duration from 30 to 120 minutes at 30-minute intervals showed that the cleaning conditions set as 950 ºC, 90-120 min under H_2 gas were suitable for removing all oxide films, even from the cracks without causing any damage to the base alloy. Increasing the process time to more than 90 minutes would result in corrosion of the base superalloy. The results of the analysis revealed that in an optimum cleaning condition, all oxide films were removed from the surface of the cracks and also, alloy elemental depleted area was not observed on the final surface. No evidence on the inter-granular attack was observed.

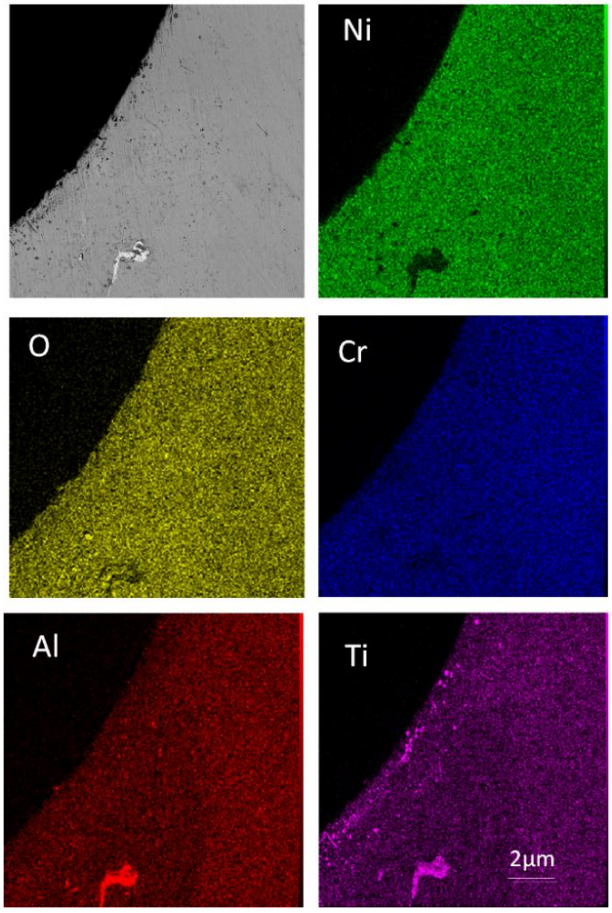

Figure 6. Elemental distribution maps of Ni, Cr, O, Ti, and Al within the region near the surface of a crack cleaned by 90 min FIC process

ACKNOWLEDGEMNET

The authors are grateful to Material and Energy Research Center (MERC) for partial financial support.

REFERENCES

1. Tao, P., Li, H., Huang, B., Hu, Q., Gong, S., Xu, Q., "The crystal growth, intercellular spacing and microsegregation of selective laser melted Inconel 718 superalloy", ***Vacuum***, Vol. 159, (2019), 382-390. https://doi.org/10.1016/j.vacuum.2018.10.074
2. Naderi, M., Farvizi, M., Shirvani, K., Rahimipour, M. R., "Cyclic oxidation behavior of uncoated and aluminum-rich nickel aluminide coated Rene-80 superalloy", ***Advanced Ceramics Progress***, Vol. 4, No. 3-4, (2018), 1-7. https://doi.org/10.30501/acp.2018.92925
3. Xiao, J., Prud'Homme, N., Li, N., Ji, V., "Influence of humidity on high temperature oxidation of Inconel 600 alloy: Oxide layers

and residual stress study", ***Applied Surface Science***, Vol. 284, (2013), 446-452. https://doi.org/10.1016/j.apsusc.2013.07.117
4. Osoba, L. O., Oladoye, A. M., Ogbonna, V. E., "Corrosion evaluation of superalloys Haynes 282 and Inconel 718 in Hydrochloric acid", ***Journal of Alloys and Compounds***, Vol. 804, (2019), 376-384. https://doi.org/10.1016/j.jallcom.2019.06.196
5. Seal, S., Kuiry, S. C., Bracho, L. A., "Studies on the surface chemistry of oxide films formed on IN-738LC superalloy at elevated temperatures in dry air", ***Oxidation of Metals***, Vol. 56, No. 5, (2001), 583-603. https://doi.org/10.1023/a:1012569803467
6. Stankowski, A., "Advanced thermochemical cleaning procedures for structural braze repair techniques", ***In Turbo Expo: Power for Land, Sea, and Air***, Vol. 36088, (2002), 1181-1195. https://doi.org/10.1115/gt2002-30535
7. Tarancon III, G., Midwest Inorganics LLC, "***Method for the Preparation of Anhydrous Hydrogen Halides, Inorganic Substances and/or inorganic Hydrides by Using as Reactants Inorganic Halides and reducing Agents***", U.S. Patent 8,834,830, (2014). https://patents.google.com/patent/US8834830B2/en
8. Wang, H., Liu, S., Li, B., Zhao, Z., "Characterization and removal of oxygen ions in LiF-NaF-KF melt by electrochemical methods", ***Journal of Fluorine Chemistry***, Vol. 175, (2015), 28-31. https://doi.org/10.1016/j.jfluchem.2015.01.018
9. Kim, M. T., Chang, S. Y., Oh, O. Y., Won, J. B., "Fluoride ion cleaning of gas turbine components using PTFE grease", ***Surface and Coatings Technology***, Vol. 200, No. 24, (2006), 6740-6748. https://doi.org/10.1016/j.surfcoat.2005.10.012
10. Miglietti, W., Blum, F., "Advantages of fluoride ion cleaning at sub-atmospheric pressure", ***Engineering Failure Analysis***, Vol, 5, No. 2, (1998), 149-169. https://doi.org/10.1016/s1350-6307(98)00013-2
11. Sangeeta, D., General Electric Co, "***Method for Cleaning Cracks and Surfaces of Airfoils***", U.S. Patent 5,685,917, (1997). https://patents.google.com/patent/US5685917
12. Yin, H., Zhang, P., An, X., Cheng, J., Li, X., Wu, S., Wu, X., Liu, W., Xie, L., "Thermodynamic modeling of LiF-NaF-KF-CrF_3 system", ***Journal of Fluorine Chemistry***, Vol. 209, (2018), 6-13. https://doi.org/10.1016/j.jfluchem.2018.02.005
13. Nicolaus, M., Möhwald, K., Maier, H. J., "Regeneration of high pressure turbine blades. Development of a hybrid brazing and aluminizing process by means of thermal spraying", ***Procedia CIRP***, Vol. 59, (2017), 72-76. https://doi.org/10.1016/j.procir.2016.09.041
14. Hamidi, S., Rahimipour, M. R., Eshraghi, M. J., Hadavi, S. M. M., Esfahani, H., "Kinetics and Microstructural Investigation of High-Temperature Oxidation of IN-738LC Super Alloy", ***Journal of Materials Engineering and Performance***, Vol. 26, No. 2, (2017), 563-570. https://doi.org/10.1007/s11665-016-2487-4
15. Wendt, H., Reuhl, K., Schwarz, V., "Cathodic deposition of refractory intermetallic compounds from flinak-melts—I. Voltammetric investigation of Ti, Zr, B, TiB_2 and ZrB_2", ***Electrochimica Acta***, Vol. 37, No. 2, (1992), 237-244. https://doi.org/10.1016/0013-4686(92)85009-a
16. Ouyang, F. Y., Chang, C. H., You, B. C., Yeh, T. K., Kai, J. J., "Effect of moisture on corrosion of Ni-based alloys in molten alkali fluoride FLiNaK salt environments", ***Journal of Nuclear Materials***, Vol. 437, No. 1-3, (2013), 201-207. https://doi.org/10.1016/j.jnucmat.2013.02.021
17. Esmaeili, H., Mirsalehi, S. E., Farzadi, A., "Vacuum TLP bonding of Inconel 617 superalloy using Ni-Cr-Si-Fe-B filler metal: metallurgical structure and mechanical properties", ***Vacuum***, Vol. 152, (2018), 305-311. https://doi.org/10.1016/j.vacuum.2018.03.048
18. Singh, A. R. P., Nag, S., Hwang, J. Y., Viswanathan, G. B., Tiley, J., Srinivasan, R., Fraser, H. L., Banerjee, R., "Influence of cooling rate on the development of multiple generations of γ′ precipitates in a commercial nickel base superalloy", ***Materials Characterization***, Vol. 62, No. 9, (2018), 878-886. https://doi.org/10.1016/j.matchar.2011.06.002
19. Shahbazi, M., Tayebifard, S. A., Razavi, M., "Effect of Ni content on the reaction behaviors and microstructure of TiB_2-TiC/Ni cermets synthesized by MASHS", ***Advanced Ceramics Progress***, Vol. 2, No. 2, (2016), 22-26. https://doi.org/10.30501/acp.2016.70020
20. Zheng, L., Zhang, M., Dong, J., "Oxidation behavior and mechanism of powder metallurgy Rene95 nickel based superalloy between 800 and 1000 C", ***Applied Surface Science***, Vol. 256, No. 24, (2010), 7510-7515. https://doi.org/10.1016/j.apsusc.2010.05.098
21. Doolabi, D. S., Rahimipour, M. R., Alizadeh, M., Pouladi, S., Hadavi, S. M. M., Vaezi, M. R., "Effect of high vacuum heat treatment on microstructure and cyclic oxidation resistance of HVOF-CoNiCrAlY coatings", ***Vacuum***, Vol. 135, (2017), 22-33. https://doi.org/10.1016/j.vacuum.2016.10.014
22. Janz, G. J., Tomkins, R. P. T., "***Physical Properties Data Compilations Relevant to Energy Storage. IV. Molten Salts: Data on Additional Single and Multi-Component Salt Systems***", National Standard Reference Data System, National Bureau of Standards Report NSRDS-NBS 61 Part IV, U.S. Government Printing Office, Washington D.C., (1981). https://nvlpubs.nist.gov/nistpubs/Legacy/NSRDS/nbsnsrds61p4.pdf
23. Ye, X. X., Ai, H., Guo, Z., Huang, H., Jiang, L., Wang, J., Li, Z., Zhou, X., "The high-temperature corrosion of Hastelloy N alloy (UNS N10003) in molten fluoride salts analysed by STXM, XAS, XRD, SEM, EPMA, TEM/EDS", ***Corrosion Science***, Vol. 106, (2016), 249-259. https://doi.org/10.1016/j.corsci.2016.02.010
24. Mantkowski, T. E., General Electric Co, "***Fluoride Ion Cleaning Method***", U.S. Patent 8,206,488, (2012). https://patents.google.com/patent/US8206488B2/en
25. Fritscher, K., "Life and FCT failure of yttria-and ceria-stabilized EBPVD TBC systems on Ni-base substrates", ***Oxidation of Metals***, Vol. 91, No. 1, (2019), 131-157. https://doi.org/10.1007/s11085-018-9870-5
26. Williams, D. F., "***Assessment of Candidate Molten Salt Coolants for the NGNP/NHI Heat-Transfer Loop***", (No. ORNL/TM-2006/69). Oak Ridge National Lab.(ORNL), Oak Ridge, TN (United States), (2006). https://doi.org/10.2172/1360677
27. Acrivos, J., "Physical chemistry, Third Edition (Levine, Ira N.)", ***Journal of Chemical Education***, Vol. 65, No. 12, (1988), A335. https://doi.org/10.1021/ed065pA335.3
28. Fukada, S., Morisaki, A., "Hydrogen permeability through a mixed molten salt of LiF, NaF and KF (Flinak) as a heat-transfer fluid", ***Journal of Nuclear Materials***, Vol. 358, No. 2-3, (2006), 235-242. https://doi.org/10.1016/j.jnucmat.2006.07.011
29. Cruchley, S., Evans, H. E., Taylor, M. P., Hardy, M. C., Stekovic, S., "Chromia layer growth on a Ni-based superalloy: Sub-parabolic kinetics and the role of titanium", ***Corrosion Science***, Vol. 75, (2013), 58-66. https://doi.org/10.1016/j.corsci.2013.05.016
30. Kool, L. B., Ritter, A. M., Cretegny, L., Pezzutti, M. D., Beitz, S. W., General Electric Co, "***Method for Removing Oxide from Cracks in Turbine Components***", U.S. Patent 7,125,457, (2006). https://patents.google.com/patent/US7125457B2/en

Advanced Ceramics Progress: Vol. 7, No. 1, (Winter 2021) 25-34

Advanced Ceramics Progress

Research Article

Journal Homepage: www.acerp.ir

Experimental and Numerical Evaluation of Diffusion Welding of 7075 Aluminum and AZ31 Magnesium Alloys

S. Manafi [a] *, A. Azizi [b]

[a] *Department of Materials Engineering, Shahrood Branch, Islamic Azad University, Shahrood, Semnan, Iran*

[b] *Department of Mechanical Engineering, Faculty of Engineering, Ilam University, Ilam, Ilam, Iran*

ARTICLE INFO

Article History:

Received 14 November 2020
Received in revised form 03 January 2021
Accepted 31 January 2021

Keywords:

Diffusion Welding
Aluminum Alloy
Magnesium Alloy
Microstructure
FEM
Effective Stress

ABSTRACT

In the present study, AZ31 magnesium alloy was bonded to 7075 aluminum alloy at different temperatures (393, 402, 412, and 421 °C) and diffrent holding times (25, 60, and 120 min) through diffusion bonding. Moreover, axial loads of 12, 29, 38, and 80 MPa accompanied by vacuum condition were employed during the bonding. The experimental and numerical results of the successful joints confirmed the existence of different reactive layers in diffusion zones and formation of the predicted intermetallic compounds. Findings showed that by applying a pressure of 29 MPa at different temperatures of 402, 412, and 421 °C, Interfacial Transition Zone (ITZ) with thicknesses of 21.26, 21.96, and 22.60 µm, respectively, was formed. Further, the maximum amount of the bond strength (30 MPa), resulting from the proper coalescence of metal surfaces, was obtained at 402 °C. Although the hardness of ITZ was found to be greater than that of the base metals, it could increase even more mainly as a result of an increase in the bonding temperature. Moreover, the results of simulation, using DEFORM-3D software, indicated that the ITZ had different mechanical properties from base metals and that by analyzing the effective stress, the Mg alloy specimen was more deformed than Al alloy during the joining process.

https://doi.org/10.30501/ACP.2021.257290.1051

1. INTRODUCTION

It is in the earth crust that one can aboundantly find aluminum and magnesium. In this regard, magnesium (Mg) and aluminum (Al) alloys, in view of their great advantages, namely machinability, good damping properties, low density, dimensional stability, and low cost, attracted great attention in the academic research and industrial applications [1, 2]. Structural components made from Mg and Al alloys are significant industrial materials empolyed in the aerospace and transportation.

Diffusion welding is a solid-state welding process resulting from the application of heat and pressure. In this respect, solid-state diffusion and coalescence phenomenon usually occur in a controlled atmosphere with sufficient time. The process temperature usually ranges from the melting temperatures of 0.5 to 0.8 and accordingly, little plastic deformation occurs during the process [2]. Due to the formation of fewer unwanted phases in the welding zone, this welding method is of considerable significance compared to traditional welding methods [3, 4]. Some fusion welding defects such as cracking, segregation, and distortion can be avoided using diffusion bonding technology [5]. The most significant effect of the process on designing and manufacturing the industrial parts is clearly observed due to its ability of bonding both similar and dissimilar materials [6].

Welding of dissimilar materials, such as Mg and Al alloys, would result in reducing the wieght and achieving high efficiency in terms of production by substituting Mg and Al alloys for steels [7]. Nevertheless, in order to easily join the alloys, the diffusion bonding process can be employed to make a suitable and strong bonding among them [8, 9].

* Corresponding Author Email: ali_manafi2005@yahoo.com (S. Manafi)

http://www.acerp.ir/article_127892.html

Please cite this article as: Manafi, S., Azizi, A., "Experimental and Numerical Evaluation of Diffusion Welding of 7075 Aluminum and AZ31 Magnesium Alloys", ***Advanced Ceramics Progress***, Vol. 7, No. 1, (2021), 25-34. https://doi.org/10.30501/ACP.2021.257290.1051

A limited number of research studies have been conducted on modeling the diffusion welding process so far. For instance, Samanta, et al. [10] studied the atomistic simulation of diffusion bonding of dissimilar materials (Al/Cu). In this respect, a numerical approach was proposed in which molecular dynamics were combined with hierarchical calculations to predict the thickness of the diffusion layer. In another study, thermal analysis of copper-aluminum welding was performed using the finite element approach. It was stated that the thermal expansion created during the process would cause thermal residual stress in the joint area [11]. In another attempt, the thermal residual stress in the welding zone was investigated during Al/Mg diffusion bonding, the results of which revealed that the residual stress droped sharply just a short distance from the bonding interface [12].

Generally, a great deal of recent attention has been drawn to the direct application of the diffusion welding process of dissimilar materials, in which an interlayer was not employed, the plastic deformation was minimized, and joint strength increased [13]. Although 7075 aluminum alloy is widely used in advanced industries, less effort has been made to investigate the Al 7075/MgAZ31 diffusion welding in the literature. The simulation of the diffusion welding process can be used as a convenient solution to better understand the process at a lower cost and less time. To this end, the present study aimed to investigate the bonding of 7075 aluminum and AZ31 magnesium alloys using the diffusion welding process at adequate presure, temperature, and holding time in the absence of an interlayer. Moreover, the microstructural and mechanical properties were utilized to investigate the property of the joint. In the following, Al7075/MgAZ31 diffusion welding simulation is developed and discussed. This study can be further referred to as an experimental reference and simulation for dissimilar Al7075/MgAZ31 welding.

2. EXPERIMENTAL PROCEDURES

Square-shaped specimens (13mm × 13mm) with a thickness of 5 mm were machined from magnesium (AZ31B) and aluminum (AA7075T6) alloys. Chemical analysis of raw materials is presented in Table 1.

TABLE 1. Chemical composition of base metals (wt. %)

Alloy Type	Al	Zn	Mn	Cr	Cu	Fe	Ti	Si	Mg
AZ31	3.17	1.1	0.2	-	0.03	0.004	-	0.15	Bal.
Al 7075	Bal.	5.6	0.15	0.2	1.5	0.45	0.03	0.15	2.6

In this respect, to generate the surface roughness, sandpaper number 600# for magnesium and number 1500# for aluminum was used. To remove the impurity before testing the surface, the samples were ultrasonically cleaned in an acetone bath for 15 minutes. Then, the process continued through ethanol 96 and then, the samples were dryed using the flow of warm air. Moreover, an induction furnace (10 °C/min) was utilized to heat up the specimens to the degree of the bonding temperature; to this end, the required pressure was simultaneously used. Accordingly, Hot Press KHP-200 furnace with the ability to create 1×10^{-3} torr vacuum was used (Figure 1). The maximum applied temperature was 1700 °C, and the dimensions of the chamber were $200\times200\times150$ mm^3. This furnace allows pressure and temperature to be simultaneously applied while creating a vacuum in the chamber. Pressure was applied by 2 hydraulic jaws embedded inside th chamber. The diameter of the upper jaw, made of hot working steel H13, of the press was 100 mm. Moreover, in order not to increase the temperature of the jaws to more than 100 °C, a cooling system was installed inside them. However, the minimum force that the press could apply was 500 kg. The furnace heating system was equipped with graphite elements, covered with a layer of compressed graphite fibers to prevent heat loss inside the furnace. Due to the significant effect of the temperature on both process and obtained results, the accuracy of the actual temperature shown by the furnace indicator was verified and calibrated using a reference thermometer (TES-1306 thermometer with K-Type thermocouple input with the acuarcy of ±3 °C). In case the lower bonding temperature was taken, no bonding between Mg and Al alloys occured due to the inadequate temperature that caused atom difussion. Of note, a decrease in the bonding presure was caused by high bonding temperature released from melting the Mg alloy. Therefore, selecting the appropriate process temperature is of significance, which is usually selected in the eutectic temperature range [8]. The proper conducted bonding times were 60 and 120 min. In case of the applied low pressure, an insufficient contact was established between the roughness of the surfaces of the samples. As a result, the chance of diffusion would be reduced. Moreover, in the presence of high pressure, the plastic deformation of the samples would occur. According to the results and experimental findings, the operational 29 MPa pressure was selected, yielding the best welding results. As the bonding was completed and just before its removal from the chamber, the samples were cooled down. A Scanning Electron Microscope (SEM) equipped with EDS/EPMA and VEGA//TESCAN-LMU was employed to study the microstructure and chemical analysis of the welding diffusion layer. It was placed in a solution containing 1/4 ml acetic acid (CH_3COOH), 0.6 g picric acid ($C_6H_3N_3O_7$), 10 ml ethanol (C_2H_6O), and distilled water (H_2O), in which the magnesium side was immersed for 15 s, thus being etched. However, Keller's solution was

used for etching the aluminum side. Moreover, ASTM: D1002-10 standard was used to perform shear strength test. Samples with the cross-sectional area of 10×10 mm^2 were cut by wirecut machine. Figure 2 shows the fixture used for shearing experiments. It is made of cold-rolled steel (S.P.K. 110) with hardness of 700 HV (HRC 60). Further, SANTAM STM-50 apparatus with the loading rate of 0.5 mm/min was utilized to apply the shearing force.

Figure 1. Diffusion bonding apparatues

Figure 2. Fixture designed for shearing test

Microhardness tests were performed by Vickers tester with an applied load of 50 g and a load duration of 20 s at intervals of 50 µm perpendicular to the joint. The hardness of Al 7075-T6 and Mg AZ31-O base metals was 130 and 48 HV, respectively.

3. RESULTS AND DISSCUSSION

Different specific results were obtained for welds performed at different temperatures, times, and pressures. However, the specimens welded in inappropriate conditions did not make full bonding. Figures 3 (a-b) show that the welds performed at 38 MPa pressure and 120 min holding time and those at 80 MPa pressure and 25 min holding time, respectively, at the constant temperaturee of 393 °C, cannot make a complete joint. The Mg side was largely deformed due to the higher melting point and greater strength of A1. Furthermore, as observed in Figure 1c, due to the insufficient pressure and holding time, welding did not occur and diffusion zone was not formed. Accordingly, increasing the temperature up to 402, 412, and 421 °C and selecting the appropriate holding time (60 min) and pressure (29 MPa) would raise the possibility of diffusion of atoms and full bonding (Figure 4). The rsults from previous studies showed that the surface roughness of the contact area was an effective factor in the bonding process [14-18]. Since the surfaces are not smooth, an initial contact is witnessed between the aspirities of surfaces.

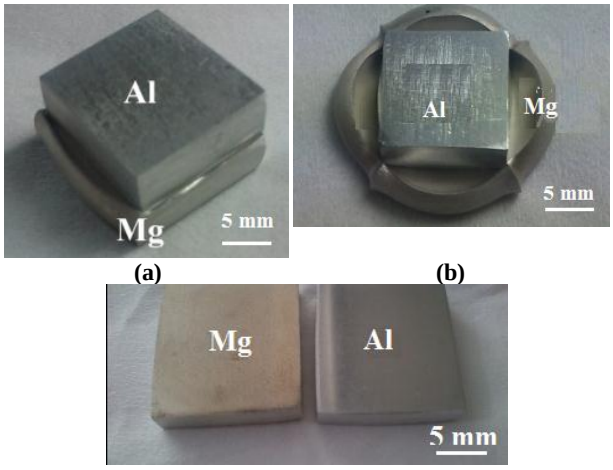

Figure 3. Unsuccessful welding with their welding conditions, a) T=393 °C, HT=120 min, P=38 MPa; b) T=393 °C, HT=25min, P=80 MPa; and c) T=402 °C, HT=30 min, P=12 MPa

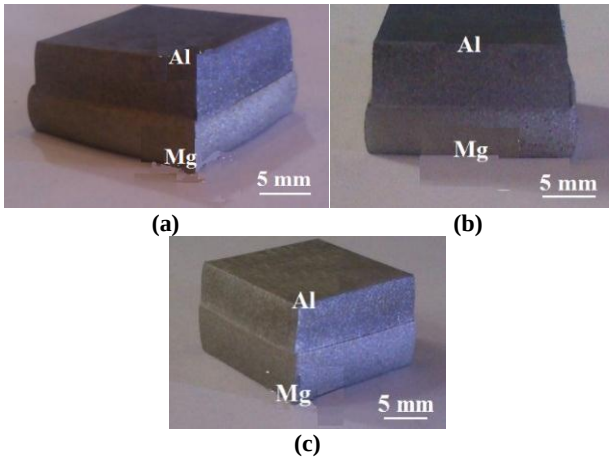

Figure 4. Successful welding with their welding conditions, a) T=402 °C, HT=60 min, P=29 MPa; b) T=412 °C, HT=60 min, P=29 MPa; and c) T=421 °C, HT=60 min, P=29 MPa

Then, an increase was observed in the contact surface of the two pieces brought about by plastic deformation and slip of roughness. Of note, at various temperatures, deformation increments and diffusion phenomenon can lead to elimination of boundaries in the interface. Finally, the filled interspaces can be observed [15]. Process temperature affects the diffusion of atoms and consequently, influences the structure of the bonding zone. Therefore, can be regarded as an effective parameter in the welding process [19, 20]. Moreover, in diffusions between two dissimilar materials, atoms with a higher diffusion coefficient diffuse faster than those with a lower diffusion coefficient [21]. The diffusion coefficients of aluminum and magnesium are equal to 1.89×10^{-12} and 2.29×10^{-12} m^2/s, respectively [9]. Therefore, more atoms diffuse across the Mg side to the Al side. This causes an imbalance in the diffusion flux and, as a result, creats voides in the bonding area. These voides, created due to the differences in the diffusion coefficient of the dissimilar materials are called Kirkendall voides, frequently referred to in the studies conducted by previous researchers [19, 21]. In a majority of the research papers investigating the dissimilar diffusion bonding, the existence of these voids was proved in the magnesium side [22]. However, in this study, Kirkendall voids were not observed through examining SEM images of the bonding zone. The difference in the diffusion coefficient of the two dissimilar materials is known as an influential parameter in the formation of the Kirkendall void, which itself depends on time and temperature. Generally, it can be concluded that the greater the difference in the diffusion coefficient, the greater the probability of the formation of Kirkendall void. Figure 5 shows the three distinct regions at the joints, performed at 402°C and 421 °C for holding time of 60 minutes. These three regions are Mg transition region (zone A), middle diffusion region (zone B), and Al transition region (zone C), respectively. The thickness of the ITZ was 21.26 µm at 402 °C, 21.96 µm at 412 °C, and 22.60 µm at 421 °C, respectively. It can be concluded that only a 19 °C increase in the temperature would lead to a 6 increase in the thickness of the ITZ. When the temperature increased, more atoms would be diffused across the interface. Hence the ITZ layer would be more thickened (Figure 6).

All samples were examined through area and linear EDS analysis. Furthermore, with the help of binary Al–Mg phase diagram, an attempt was made to determine the phases formed in the welding area (Figure 7 [23]). Figure 8 shows the linear EDS analysis of layers A, B, and C of the ITZ layer of the welded specimen at 402 °C. By examining the concentration of the elements, through both EDS analysis (Table 2) and Al-Mg binary phase diagram, it can be concluded that the layer formed on the magnesium side (layer A) comprises $Al_{12}Mg_{17}$ (γ). This phase has a BCC crystal structure with the hardness of 4.35 nHV [14]. The middle diffusion layer is a

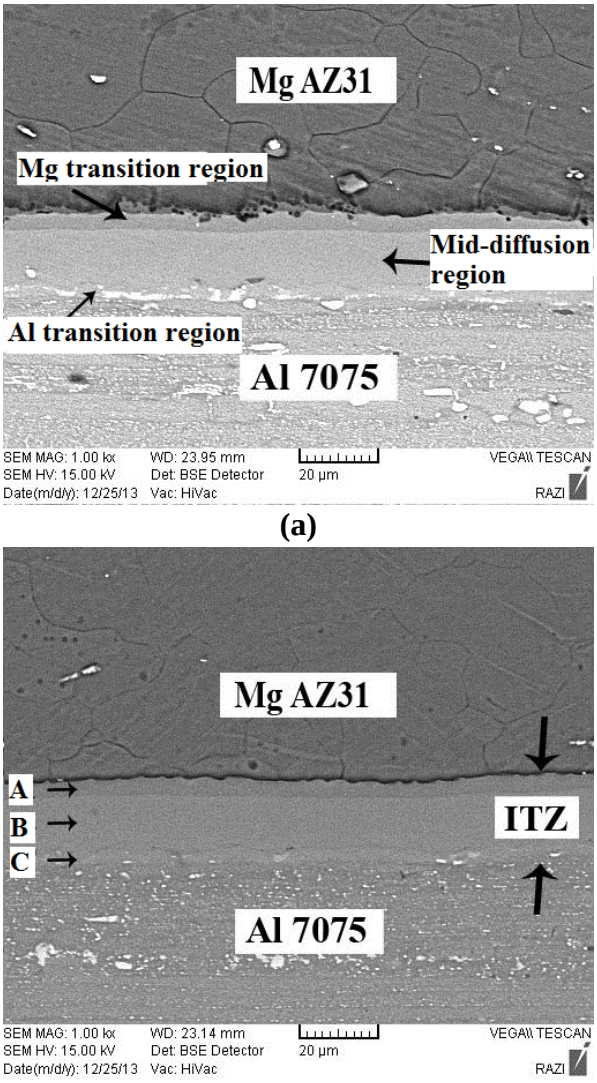

Figure 5. SEM image of interface bonding at P=29MPa, HT=60Min and **a)**T=402°C, **b)** T=421°C

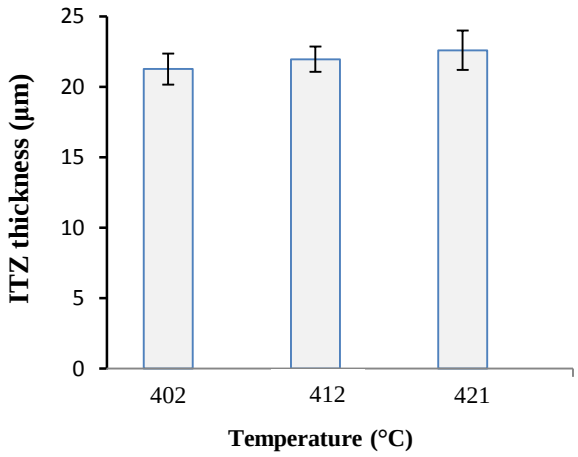

Figure 6. Effect of welding temperature on ITZ thickness

combination of phases γ and β (Al_3Mg_2), and the value for phase β on the aluminum side is greater than that on the other side. The β phase with FCC structure has the hardness of 4.4 nHV [14]. In case the diffusion welding is at its starting point, Mg and Al atoms start diffusing into the contact layer. In the next step, Al and Mg atoms diffuse into different zones and their values increase in the bonded layer. Then, a reaction occurs between them and a combination layer consisting of Al and Mg is formed. Further, as the temperature increases, the Al in Mg/MgAl interface begins to diffuse to the Mg side, the reaction $17Mg+12Al \rightarrow Mg_{17}Al_{12}$ occurs. and $Mg_{17}Al_{12}$ is formed. As mentioned earlier, the amount of Mg in the MgAl/Al interface layer increases; and as a resutl of its diffusion through the Al side, the reaction $2Mg+3Al \rightarrow Al_3Mg_2$ occurs and the Mg_2Al_3 phase is formed. Finally, as the process continues, there is no change in the phases and only the thickness of the ITZ layer gradually increases [9, 24]. In case of more heating, eutectic reactions $Al_{12}Mg_{17} + Mg \rightarrow L$ and $Al_3Mg_2 + Al \rightarrow L$ occur at eutectic temperature 437 °C and 450 °C, respectively. Diffusion welding is a solid-state bonding process in which the weld metal is not usually melted. To reveal the liquid formation, micrographic images can be employed to detect dendritic structures, indicating the solidification microstructure [25]. Since the operating temperatures are lower than the eutectic temperature, the liquation does not occur at the bonding zone and the intermetallic layers formed at the joint interface can be attributed to solid-state inter-diffusion of Al and Mg during diffusion bonding. It should be noted that further melting should be avoided; otherwise, it would reduce the applied pressure during the diffusion welding and then, the metal with low melting temperature would be deformed.

In the solid state processes, the formation rate of the intermetallic compunds is affacted by the rate of diffusion, which also depends on parameters such as process temperature, grain size, and other metallurgical characteristics. To form these phases, the two sides first diffuse each other and, then, a supersaturated solid solution is formed.

As the amount of elements in the solution increases, nucleation begins and intermetallic phases are formed. Then, these compounds grow longitudinally along the bonding line. In the next step, the next intermetallic compounds are formed and grown. It can be concluded that the compounds with the highest amount of an element and higher diffusion coefficient would nucleate first. Therefore, γ-$Al_{12}Mg_{17}$ is formed first [14]. In this process, the Mg diffusion activation energy in Al is lower than Al in Mg, hence Mg diffuses faster. Since the γ-$Al_{12}Mg_{17}$ phase is rich in Mg, it is formed earlier than the β-Al_3Mg_2 phase [9].

As Figure 9 illustrates, in the case of examining the diffusion element map obtained from the EDS analyses, the presence of Zn is observed in the intermetallic bonding. Furthermore, investigation of elemental maps clarifies that the Zn diffusion area in the welding joint is massed in the Al side of the joints (Figure 10). The Zn distribution also reveals an accumulated precipitate zone at the Al_3Mg_2 aluminum alloy interface. The extraordinary growth of the Zn concentration in this zone was already expected due to the diffusion of Al in the intermetallic compounds; consequently, the formation of $MgZn_2$ precipitates occurs.

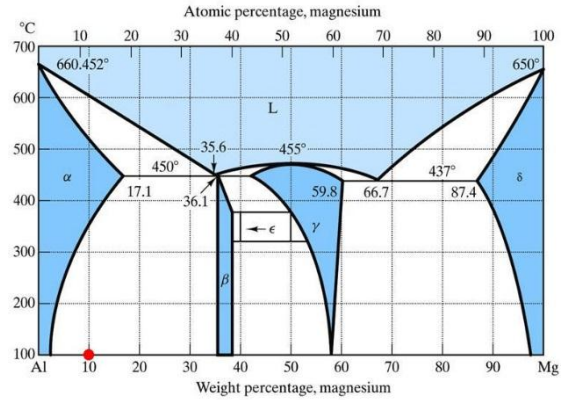

Figure 7. Binary Al-Mg phase diagram [23]

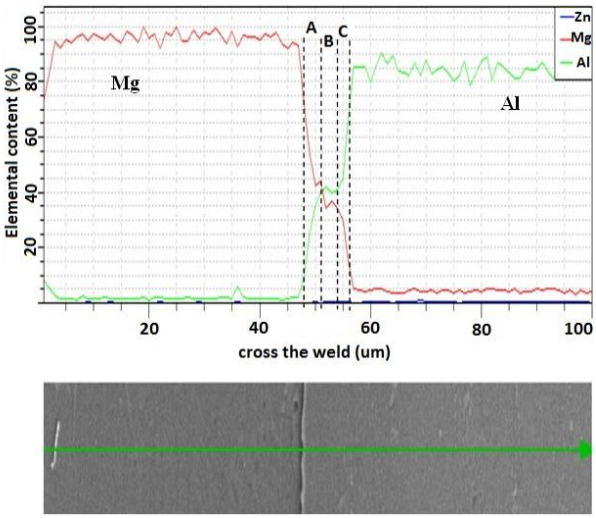

Figure 8. EDS line scan across the bonding interface as indicated by line for the specimen welded at 402 °C, P=29 MPa, and HT=60 min

TABLE 2. Basic elemental percentage in different joint zones of Figure 4b according to point analysis

	Mg (wt. %)	Al (wt. %)	Zn (wt. %)	Cu (wt. %)
A	53.76	46.13	-	-
B	36.79	60.00	3.21	
C	22.41	73.73	2.11	1.75

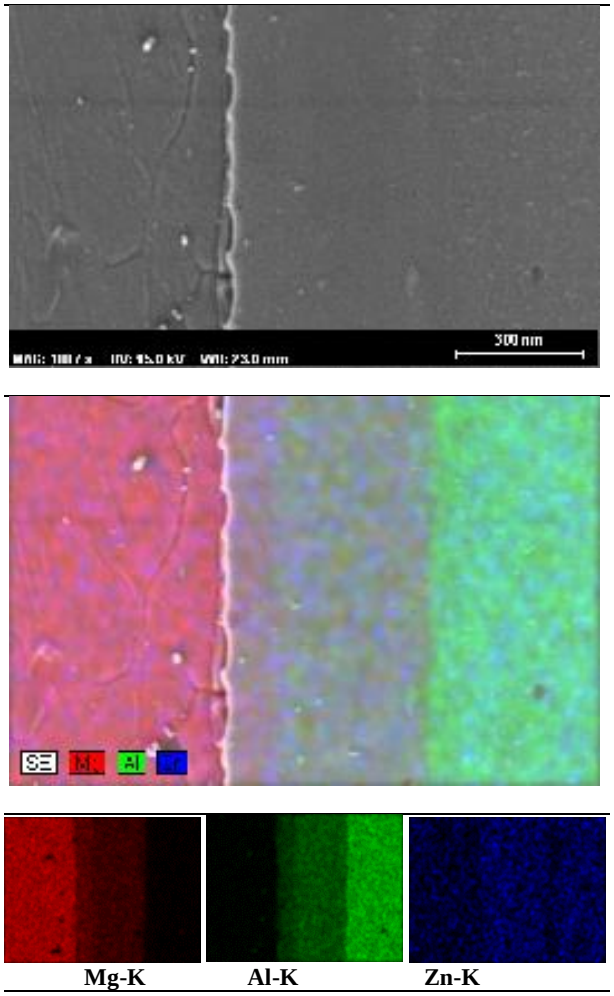

Figure 9. Element map obtained from the EDS analyses for the specimen diffusion welded at 421 °C for 60 min

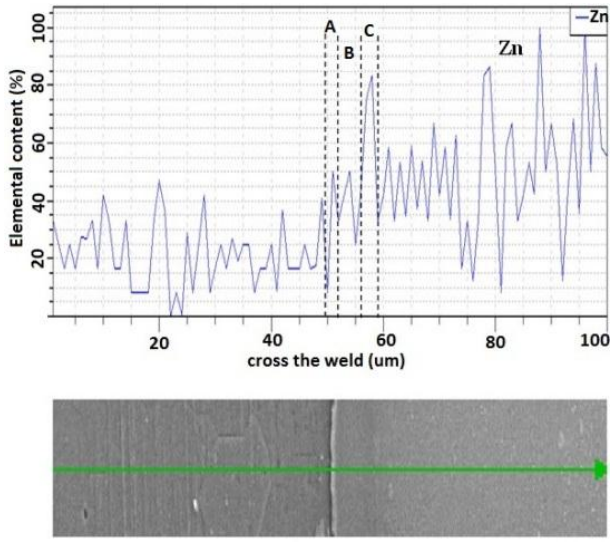

Figure 10. EDS line scan for Zn element across the bonding interface as indicated by line for the specimen welded at 421 °C, P=29 MPa and HT=60 min

Micro-hardness experiment was applied to investigate the hardness characteristics of the joint zone. The Vickers hardness on the Mg side is approximately equal to 40 HV, which increases sharply in the interface zone and then, is reduced to 60 HV on the Al side (Figure 11). Of note, increasing the temperature would lead to an increase in the microhardness in the reaction zone; however, it has no significant effect on the microhardness of base metals. In this sense, the maximum hardness in the interface reaches 90 HV and 70 HV at process temperatures of 421 °C and 402 °C, respectively. Accordingly, reduction in the amount of brittle intermetallic component formation at lower temperatures should be taken into account. Due to the presence of α-phase, the hardness of the reaction layer at 402 °C approaches the hardness of the aluminum base metal.

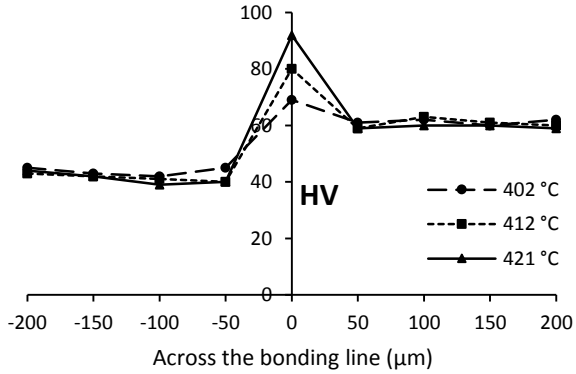

Figure 11. Effect of temperature on microhardness across the bonding line

Figure 12 shows the changes in the shear strength of welded specimens at different process temperatures. The results showed that the maximum shear stress was equal to 30 MPa at the temperature of 402 °C. In addition, at 421 °C, it reached 20 MPa. At 402 °C, the plastic deformation of the surface roughness would result in better contact of the surfaces, thus reducing the brittleness due to the formation of intermetallic phases [26]. Therefore, the bond shear strength would be considerably improved. On the contarary, by increasing the temperature to 421 °C, the amount of brittle compounds would basically increase and accordingly, the positive effect of better contact of surfaces at high temperatures would be eliminated, thus reducing the shear strength [26].

In order to simulate and investigate the effect of process parameters, diffusion welding of 7075 aluminum alloy and AZ31 magnesium alloy was simulated using Deform-3D FEM software. DEFORM-3D is capable of simulating three-dimensional material flow during the forming processes without the cost and delay of shop trials. To this end, the tetrahedral mesh type with 0.7 mm element size opted for the meshing process, and the area near to the bonding would yiled a quite fine mesh with an

element size of 0.3 mm. Furthermore, the friction coefficient was chosen to be 0.25, as suggested by DEFORM-3D software for diffusion welding process (Figure 13).

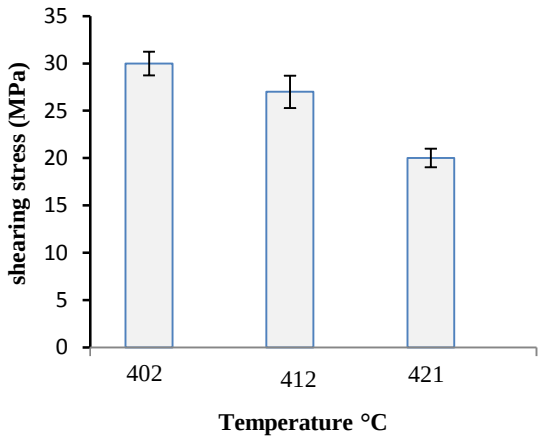

Figure 12. Effect of temperature on the welding shear strength

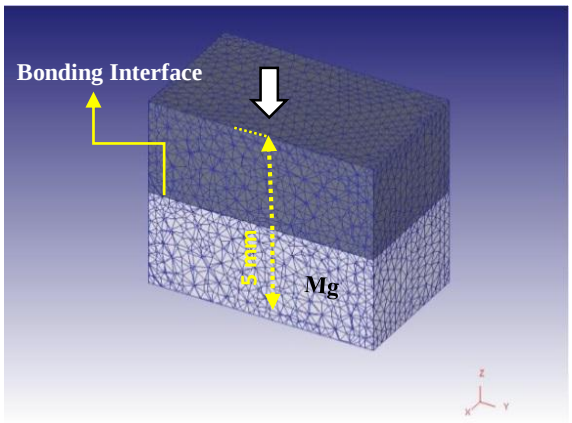

Figure 13. The initial billet meshed finite element model

Table 3 reported the thermo-mechanical properties of the used material in this study which was taken from ASTM Standards. Since the diffusion welding process is a thermo-mechanical process, the Young's module of the materials changes during the process. Table 4 reports the amounts of Young's module of 7075 aluminum alloy and AZ31 magnesium alloy at different temperatures.

TABLE 3. Mechanical and thermal properties used in this research

Parameters	Poisson Ratio	Thermal Conductivity (W/mK)	Heat Capacity (J/g°C)	Thermal E xpansion (m/m°C)
Al7075	0.33	130	0.960	23×10^{-6}
AZ31	0.35	96	1.020	25×10^{-6}

TABLE 4. Young's module variations of MgAZ31 and Al7075 at different temperatures

Temperature (°C)	Young's modulus (GPa)	
	MgAZ31	Al7075
100	38	68
150	32	65
200	29.8	63
250	28.9	59
450	25.9	48

The required data in this study were extracted from the experimental studies previously conducted by other researchers [27, 28]. In the next step, the extracted data of the plastic behavior (flow stress curve) of 7075 aluminum alloy and AZ31 magnesium alloy in different strain rates and temperatures were entered in DEFORM-3D software.

The effective von Mises stress was employed to determine whether or not the sample would yield the desired result during the complex loading. In this case, it can also be called the effective stress. The effective stress distribution in the deformed sample is inhomogeneous and varies based on the process temperature. The amount of effective stress close to the core of the AZ31 magnesium specimen was maximum. The highest effective stresses were 9.1, 8.8, and 7.5. MPa for temperatures at 421, 412, and 402 °C, respectively. Of note, the value for the effective stress in the 7075 aluminum, compare to the AZ31 magnesium specimen, was quite low, mainly due to the fact that Young's module of AZ31 magnesium between 402 to 421 °C was approximately two times lower than that of 7075 aluminum.

Given that the point tracing approach was employed as shown in the sectional view (Figure 13), the variation of the effective stress of 7075 aluminum and AZ31 magnesium was recored. The value for the effective stress according to the distance from the bonding interface in both materials was measured and reported in Figure 14. As observed, during the diffusion welding process, by increasing the temperature, the effective stress would gain higher values and the amount of the effective stress of AZ31 magnesium would be remarkably larger than that of 7075 aluminum. The change of effective stress across the 7075 aluminum specimen is illustrated in Figure 14a. In case the distance from the bonding interface increased, the effective stress would significantlly decrease. Moreover, Figure 14b depicts the effective stress across the bonding interface on the AZ31 magnesium side. In a distance almost equal to 0.5 mm from the bonding interface, the graph incrementally increased and then, by increasing the distance from the bonding interface, the effective stress would gradually decrease. Diffusion of Al atoms into Mg

would change the frictional force in the interface layer and cause an increase and decrease in effective stress, respectively. Therefore, changes in the range and amount of effective stress can be used as an indicator for diffusion monitoring of atoms in the welding process. As the intensity of these changes increased, more diffusion would occur and the thickness of the interface layer would be greater.

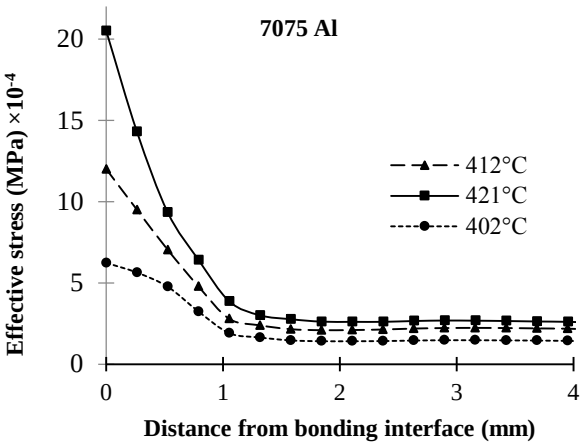

(a)

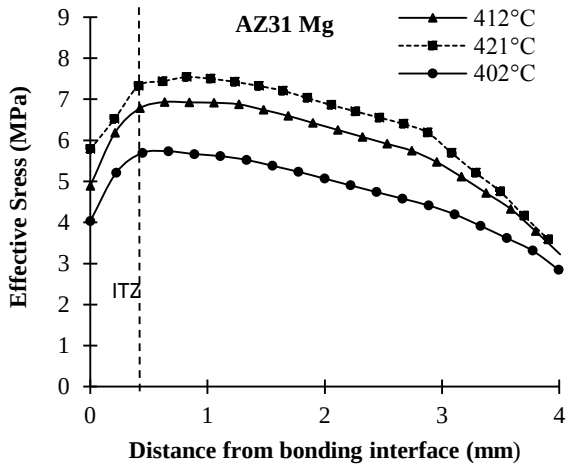

(b)

Figure 14. Effective stress according to distance from the bonding interface a- Al ; b- Mg

An experiment was performed to validate the simulation results. The diffusion welding experiment was performed at the temperature of 402 °C. The forming force was simulated during the welding process. Figure 15 shows a comparison between the welding force and hydraulic press arm stroke for the simulated and trial results. The results indicated a good agreement between the experimental results and the simulation. However, at the beginning and end of arm stroke, significant differences were observed between the simulated and experimental results. By considering the load–stroke curve, the amount of press tonnage used fot performing the diffusion welding process can be determined.

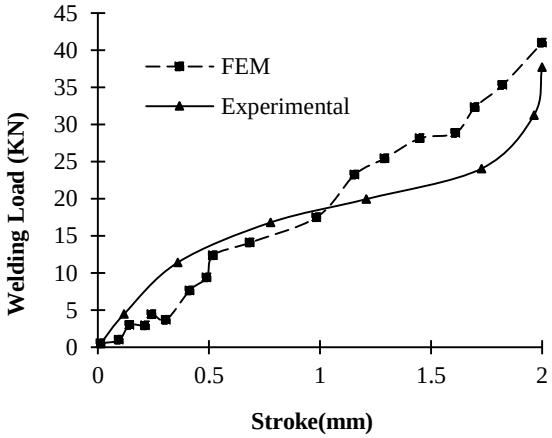

Figure 15. Comparison between the simulated and experimental load of diffusion welding process at T=402 °C

4. CONCLUSION

The present study aimed to investigate the diffusion bonding of 7075 aluminum and AZ31 magnesium alloys. To this end, the effect of different conditions such as temperature, holding time, and applied pressure during the welding process was evaluated. The results from experiments and simulations indicated that:

- Due to the insufficient temperature, pressure, and holding time for the diffusion, the bonding performed at 38 MPa and 120 min as well as at 80 MPa and 25 min could not make a full bonding (while the process temperature was kept constant at 393 °C). However, by applying the pressure, temperature, and holding time equal to 12 MPa, 402 °C, and 30 min, respectively, a complete connection was not obtained and in most areas, proper diffusion did not occur.
- As the temperature increased from 402 °C to 421 °C, more atoms diffused, resulting in a 6 increase in the thickness of the ITZ layer.
- A careful examination of the weld microstructure revealed that the formed layer from the magnesium side toward the aluminum side was composed of γ ($Al_{12}Mg_{17}$), a mixture of γ and β (Al_3Mg_2), and a mixture of γ and β with higher weight percent of β, respectively.
- On the Al side of the joints, Zn in the weld interface was denser. The significant increase in the Zn concentration in this region was due to the diffusion

of aluminum into the intermetallic phases as well as the formation of $MgZn_2$ precipitates.

- The shear strength of joints performed at 402 °C and 421 °C was 30 MPa and 20 MPa, respectively, indicating the considerable effect of increasing the process temperature on the formation of more intermetallic compounds, thus reducing the shear strength. In addition, due to the formation of more brittle phases at high temperatures, the hardness of the ITZ increased by increasing the temperature. In this regard, the maximum hardness of 90 HV was obtained during the experiments caried out at 421 °C.
- The results derived by FEM simulation were in good agreement with the experimental trials. By recording the effective stress, important information about the thermo-mechanical affected zone and thickness of the interface layer can be obatined. In other words, through the effective stress simulation, significant measures were taken in monitoring the diffusion welding process.

ACKNOWLEDGEMENTS

The assistance given by Dr. Y. Alizadeh and Mr Mehraban in Strength Materials and Structural Quality Control Research Laboratory, Mechanical Engineering Department, Amirkabir University of Technology is acknowledged.

REFERENCES

1. Mahendran, G., Balasubramanian, V., Senthilvelan, T., "Developing diffusion bonding windows for joining AZ31B magnesium–AA2024 aluminium alloys", ***Materials & Design***, Vol. 30, No. 4, (2009), 1240-1244. https://doi.org/10.1016/j.matdes.2008.06.015
2. Sun, D. Q., Gu, X. Y., Liu, W. H., "Transient liquid phase bonding of magnesium alloy (Mg–3Al–1Zn) using aluminium interlayer", ***Materials Science and Engineering: A***, Vol. 391, No.1-2, (2005), 29-33. https://doi.org/10.1016/j.msea.2004.06.008
3. Aydın, K., Kaya, Y., Kahraman, N., "Experimental study of diffusion welding/bonding of titanium to copper", ***Materials & Design***, Vol. 37, (2012), 356-368. https://doi.org/10.1016/j.matdes.2012.01.026
4. Guo, Y., Qiao, G., Jian, W., Zhi, X., "Microstructure and tensile behavior of Cu-Al multi-layered composites prepared by plasma activated sintering", ***Materials Science and Engineering: A***, Vol. 527, No. 20, (2010), 5234-5240. https://doi.org/10.1016/j.msea.2010.04.080
5. Nami, H., Halvaee, A., Adgi, H., Hadian, A., "Microstructure and mechanical properties of diffusion bonded Al/Mg_2Si metal matrix in situ composite", ***Materials & Design***, Vol. 31, No. 8, (2010), 3908-3914. https://doi.org/10.1016/j.matdes.2010.03.007
6. Hadian, R., Emamy, M., Varahram, N., Nemati, N., "The effect of Li on the tensile properties of cast Al–Mg_2Si metal matrix composite", ***Materials Science and Engineering: A***, Vol. 490, No. 1-2, (2008), 250-257. https://doi.org/10.1016/j.msea.2008.01.039
7. Somekawa, H., Watanabe, H., Mukai, T., Higashi, K., "Low temperature diffusion bonding in a superplastic AZ31 magnesium alloy", ***Scripta Materialia***, Vol. 48, No. 9, (2003), 1249-1254. https://doi.org/10.1016/S1359-6462(03)00054-X
8. Fernandus, M. J., Senthilkumar, T., Balasubramanian, V., "Developing Temperature–Time and Pressure–Time diagrams for diffusion bonding AZ80 magnesium and AA6061 aluminium alloys", ***Materials & Design***, Vol. 32, No. 3, (2011), 1651-1656. https://doi.org/10.1016/j.matdes.2010.10.011
9. Jafarian, M., Khodabandeh, A., Manafi, S., "Evaluation of diffusion welding of 6061 aluminum and AZ31 magnesium alloys without using an interlayer", ***Materials & Design (1980-2015)***, Vol. 65, (2015), 160-64. https://doi.org/10.1016/j.matdes.2014.09.020
10. Samanta, A., Xiao, S., Shen, N., Li, J., Ding, H., "Atomistic simulation of diffusion bonding of dissimilar materials undergoing ultrasonic welding", ***The International Journal of Advanced Manufacturing Technology***, Vol. 103, No. 1, (2019), 879-890. https://doi.org/10.1007/s00170-019-03582-9
11. Kumar, S. S., Ravisankar, B., Sheriff, M. A., Silvister, M. J., "Thermal Analysis of Dissimilar Materials Diffusion Bonding Using Finite Element Method", In ***Materials Science Forum***, Vol. 969, (2019), 858-863. Trans Tech Publications Ltd. https://doi.org/10.4028/www.scientific.net/MSF.969.858
12. Ding, Y., Ju, D., "Finite Element Analysis of Residual Stress in the Diffusion Zone of Mg/Al Alloys", ***Advances in Materials Science and Engineering***, Vol. 2018, (2018), 1-8. https://doi.org/10.1155/2018/1209849
13. Mahendran, G., Balasubramanian, V., Senthilvelan, T., "Mechanical and metallurgical properties of diffusion bonded AA2024 Al and AZ31B Mg", ***Advances in Materials Research: AMR***, Vol. 1, No. 2, (2012), 147-160. https://doi.org/10.12989/amr.2012.1.2.147
14. Zhang, M. X., Huang, H., Spencer, K., Shi, Y. N., "Nanomechanics of Mg–Al intermetallic compounds", ***Surface and Coatings Technology***, Vol. 204, No. 14, (2010), 2118-2122. https://doi.org/10.1016/j.surfcoat.2009.11.031
15. Zuruzi, A. S., Li, H., Dong, G., "Effects of surface roughness on the diffusion bonding of Al alloy 6061 in air", ***Materials Science and Engineering: A***, Vol. 270, No. 2, (1999), 244-248. https://doi.org/10.1016/S0921-5093(99)00188-4
16. Derby, B., Wallach, E. R., "Theoretical model for diffusion bonding", ***Metal Science***, Vol. 16, No. 1, (1982), 49-56. https://doi.org/10.1179/030634582790427028
17. Derby, B., Wallach, E. R., "Diffusion bonding: development of theoretical model", ***Metal Science***, Vol. 18, No. 9, (1984), 427-431. https://doi.org/10.1179/030634584790419809
18. Elzey, D. M., Wadley, H. N. G., "Modeling the densification of metal matrix composite monotape", ***Acta Metallurgica et Materialia***, Vol. 41, No. 8, (1993), 2297-2316. https://doi.org/10.1016/0956-7151(93)90312-G
19. Zhang, J., Shen, Q., Luo, G., Li, M., Zhang, L., "Microstructure and bonding strength of diffusion welding of Mo/Cu joints with Ni interlayer", ***Materials & Design***, Vol. 39, (2012), 81-86. https://doi.org/10.1016/j.matdes.2012.02.032
20. Mofid, M. A., Loryaei, E., "Investigating microstructural evolution at the interface of friction stir weld and diffusion bond of Al and Mg alloys", ***Journal of Materials Research and Technology***, Vol. 8, No. 5, (2019), 3872-3877. https://doi.org/10.1016/j.jmrt.2019.06.049
21. Srinivasan, D., Subramanian, P. R., "Kirkendall porosity during thermal treatment of Mo–Cu nanomultilayers", ***Materials Science and Engineering: A***, Vol. 459, No. 1-2, (2007), 145-150. https://doi.org/10.1016/j.msea.2007.01.037
22. Gao, M., Mei, S., Li, X., Zeng, X., "Characterization and formation mechanism of laser-welded Mg and Al alloys using Ti interlayer", ***Scripta Materialia***, Vol. 67, No. 2, (2012), 193-196. https://doi.org/10.1016/j.scriptamat.2012.04.015

23. Liu, L., Ren, D., "A novel weld-bonding hybrid process for joining Mg alloy and Al alloy", ***Materials & Design***, Vol. 32, No. 7, (2011), 3730-3735. https://doi.org/10.1016/j.matdes.2011.03.050
24. Wang, J., Yajiang, L., Wanqun, H., "Interface microstructure and diffusion kinetics in diffusion bonded Mg/Al joint", ***Reaction Kinetics and Catalysis Letters***, Vol. 95, No. 1, (2008), 71-79. https://doi.org/10.1007/s11144-008-5259-9
25. Firouzdor, V., Kou, S., "Formation of Liquid and Intermetallics in Al-to-Mg Friction Stir Welding", ***Metallurgical and Materials Transactions A***, Vol. 41, No. 12, (2010), 3238-3251. https://doi.org/10.1007/s11661-010-0366-4
26. Mahendran, G., Balasubramanian, V., Senthilvelan, T., "Influences of diffusion bonding process parameters on bond characteristics of Mg-Cu dissimilar joints", ***Transactions of Nonferrous Metals Society of China***, Vol. 20, No. 6, (2010), 997-1005. https://doi.org/10.1016/S1003-6326(09)60248-X
27. Li, Y., Wu, Z., "Microstructural Characteristics and Mechanical Properties of 2205/AZ31B Laminates Fabricated by Explosive Welding", ***Metal***, Vol. 7, No. 4, (2017), 125. https://doi.org/10.3390/met7040125
28. Mei, R., Bao, L., Cai, B., Li, C., Liu, X., "Piecewise modeling of flow stress of 7075-T6 aluminum alloy in hot deformation", ***Materials Transactions***, Vol. 57, No. 7, (2016), 1147-1155. https://doi.org/10.2320/matertrans.M2015465

Advanced Ceramics Progress: Vol. 7, No. 1, (Winter 2021) 35-45

Advanced Ceramics Progress

Research Article

Journal Homepage: www.acerp.ir

Microhardness Optimization of Al–TiC Nanocomposite Produced by Mechanical Milling and Heat Treatment

J. Arasteh [a] *

[a] *Department of Materials Science and Engineering, Shahid Bahonar university of Kerman, Kerman, Kerman, Iran*

ARTICLE INFO

Article History:

Received 31 December 2020
Received in revised form 19 March 2021
Accepted 17 April 2021

Keywords:

Al–4%TiC
X-ray Diffraction
Milling Parameters
Taguchi Method

ABSTRACT

In this study, the Al–TiC nanocomposite was produced by the mechanical milling and sintering process. Also, the optimization of the milling parameters was performed by the Taguchi method. The X-ray diffraction analysis, scanning electron microscopy, and microhardness test were used to analyze the phase characterization, microstructure, and mechanical properties of the Al–4% TiC nanocomposite. At first, the milling speed, milling time, and ball to powder weight ratio were considered as the input data, and the microhardness was considered as the output value of the Minitab software. According to the design of the experiment, 27 experiments must be performed, which were reduced to 9 by the Taguchi method. After the milling, the powders were subjected to the cold pressing and subsequent sintering at 450 °C. The microhardness results showed that the Al–4% TiC nanocomposite was formed with a maximum microhardness of 271 HV. Furthermore, a proper model was proposed and the results indicated that there was a good agreement between the experimental and predicted microhardness.

https://doi.org/10.30501/ACP.2021.265197.1052

1. INTRODUCTION

Composite materials have been known as superior materials for more than thirty years. In this regard, the application of composite materials has been continuously growing; therefore, many requirements in the various industries, including the space industry, reactor manufacturing, construction, and transportation, cannot be satisfied by the conventional materials and need to change the properties of the materials extensively [1]. Among the composites, Particle-reinforced metal matrix composites (MMCs) are attractive and well-known materials in which hard and brittle particle reinforcements, usually ceramic, are introduced into a ductile metallic matrix [2]. A further improvement of mechanical properties can be achieved by decreasing the grain size to the nanometer scale [3]. Adding reinforcement particles to the aluminum alloys matrix, produces so-called nanocomposites, which is promising approach in order to enhance mechanical properties of the aluminum alloys [1]. These nanocomposites are considered a group of materials with excellent properties such as high strength to weight ratio, low coefficient of thermal expansion, and good wear resistance [4, 5]. Al-based composites are mostly made by distributing the ceramic particles, including SiC, Al_2O_3, TiB_2, or AlWC in the Al matrix [6-9]. Aluminum has excellent properties such as lightweight and ease of machining [10]. Al–TiC composites are one of the most important Al matrix composites with better mechanical properties than the pure Al. Titanium carbide is the appropriate reinforcement due to the high wear resistance, low thermal expansion coefficient, suitable plasticity, and good wettability to improve the properties of Al-based composites [11].

Al matrix composite production techniques in the solid-state such as mechanical milling and sintering process, have received much attention due to differences in the melting point of Al and ceramic particles [7, 12-14]. One of the most exciting advantages of mechanical milling is producing nanocrystalline structures [15]. The scientific research community highly values

* Corresponding Author Email: javadaraste68@gmail.com (J. Arasteh)

http://www.acerp.ir/article_129319.html

Please cite this article as: Arasteh, J., "Microhardness Optimization of Al–TiC Nanocomposite Produced by Mechanical Milling and Heat Treatment", ***Advanced Ceramics Progress***, Vol. 7, No. 1, (2021), 35-45. https://doi.org/10.30501/ACP.2021.265197.1052

nanocrystalline materials due to their high hardness strength and better physical, mechanical and chemical properties compared to coarse-grained materials [16]. Besides, simple equipment of milling process [17], no requirement to the high temperatures [18], and uniform dispersion of reinforcement phase particles in the matrix [19] were included to benefits from the mechanical milling technique. The studies have shown that the properties of the composites produced by mechanical milling are influenced by the microstructure, crystallite size, and morphology so that, these factors are affected by the milling conditions [20, 21]. For examlpe, Azimi and et al. synthesized Al7075-TiC nanocomposite by MA followed by hot pressing. Microstructure of obtained powders was characterized in different milling time. Furthermore, the influence of fabrication parameters including milling time, hot pressing temperature and pressure was evaluated on the mechanical properties. Improved sintering and mechanical properties was achieved by increasing hot pressing temperature and pressure; while rising temperature over 400 °C resulted in reduced hardness due to severe grain growth during hot pressing. More interestingly, influence of milling time on the mechanical properties is strongly depended on the hot pressing pressure value. Furthermore, tensile strength of ~725 MPa was obtained by consolidation under optimal parameters [22]. In another work, Feijoo and et al. produced a composite with a fine-grained AA6005A matrix and 3 vol% nanoparticles of TiC by hot extrusion and T6 heat treatment of high-pressure gas-atomised and mechanically milled powders. The nanocomposites showed remarkably higher hardness, Young's modulus, yield, and ultimate strengths at room temperature than the extruded profiles of unreinforced milled AA6005A powders obtained through refinement of the Al alloy grain structure and a strong particle–matrix bonding, although with a drop in their ductility [23]. Salem and et al showed that addition of TiC nanostructured powder to the AA2124 alloy nanopowder resulted in increase of 130% in compressive strength compared to that produced for the microscale one. Nanopowder of Al alloys produced by mechanical milling reinforced with 10 wt. % TiC is recommended for products suitable for high wear and erosion resistance applications [24].

Therefore, it is necessary to study the milling parameters and examine the effects of the milling parameters on the final product to achieve the optimal conditions. The purpose of experimental design is to identify the parameters influencing the process and determine their optimal values. Experimental design techniques can determine the variables that have the most effect on the output data. In addition, the input variables can be controlled, and the effect of uncontrollable parameters on the response variable can be minimized. Analysis of the results in the experimental design technique is performed by variance analysis (ANOVA). Taguchi method is one of the essential experimental design techniques based on variance analysis [25]. Taguchi method has advantages such as fewer experiments, less cost and time of testing, the ability to study the interactions, perform experiments in parallel, and predict the optimal response. In general, this method reduces the number of required tests for optimization and increases the results' accuracy.

Multiple pieces of research have been recently conducted on the production of Al-based composites by mechanical milling and sintering methods; however, no research has been conducted on optimizing the milling conditions for the production of Al–TiC composites with maximum microhardness by the Taguchi method. In the present study, the design of the experiment was performed by the Taguchi method, and the milling process was performed according to the conditions obtained from the experimental design. In composite fabrication by the milling process, the ball to powder weight ratio is usually between 10 and 30, milling speed is usually between 200 to 400 rpm, and milling time is usually between 10 to 50 hours. In this regard, the values and levels of input data were selected. The parameters of the ball to powder weight ratio (BPR), milling time, and milling speed were considered input data, and the microhardness of the composite was introduced as output data. Furthermore, the most influential parameter was identified and a good proposed model was introduced to predict the microhardness of aluminum-based nanocomposite. The microhardness obtained by the proposed model were compared with the experimental data. Besides, structural characteristics, including phase identification, crystallite size, lattice parameter, internal strain, microstructure, and morphology Al–4% TiC nanocomposite were investigated.

2. MATERIALS AND METHODS

In this study, Al powder (purity of 99.9%, Merck) and TiC powder (purity of 99.9%, Merck) were used as raw materials to produce Al–4% TiC composite. It should be noted that the composition of the Al-4% TiC nanocomposite is expressed by weight percentage. The mechanical milling process was performed in a high energy planetary ball mill. The Al and TiC powders were milled within a hardened steel vial along with hardened steel balls of 10 mm in diameter under a high-purity argon atmosphere. Stearic acid in the amount of 2 wt. % was chosen as a process control agent to avoid cold welding and agglomeration of powder particles. The milling experiments were stopped after each 30 min of working for 15 min to prevent an excessive temperature in the vial. It should be noted MA process was performed at room temperature and dry medium. Usage of cup and balls with the same chemical composition of precursor was the most proposing approach for reducing the

contamination of milling components. Unfortunately, due to the variety of selected systems in MA, it is impossible to make cups and balls from all of the above compounds. An alternative to reduce the impurities was to mill the powder mixture within the range of the studied composition before the start of the main tests. Accordingly, before the data collection step the mixture of each test was milled for 5 h to minimize the variation the chemical composition. The effects of different milling parameters, including the BPR, rotation speed, and milling time on the microhardness of Al–TiC nanocomposite, were studied. In composite fabrication by the milling process, the ball to powder weight ratio is usually between 10 and 30 (The ball to powder weight ratio shows the ratio of the balls' weight to the powders), milling speed is usually between 200 to 400 rpm, and milling time is usually between 10 to 50 hours. In this regard, the values and levels of input data were selected [26-31]. The BPR levels were selected 10, 20, and 30, and the rotation speed of 200, 300, and 400 rpm, and the milling time of 10, 30, and 50 h were considered input data. Before the data collection step, the mixture of each test was milled for 5 hours to minimize the variation of the chemical composition [16]. According to the previous research on the composite fabrication by the milling process, the ball to powder weight ratio is usually between 10 to 30, milling speed between 200 to 400, and milling time for composite preparation is usually between 10 to 50 hours. The levels of parameters have also been selected based on previous works. In this research, three factors with three levels indicated 27 experiments are required to be done according to full factorial design. Taguchi technique was used to design the experiment, which reduced the number of experiments and optimized the milling parameters. According to the experimental design based on the Taguchi technique, nine experiments can be replaced with 27 experiments (Table 1). Moreover, the statistical analysis of variance (ANOVA) was used to determine the effect of the input parameters. The levels of the input data which were chosen for the experiment are shown in Table 1. Finally, the empirical results were compared with the theoretical results obtained from the experimental design.

X-ray diffraction analysis (XRD) was used to investigate the structural changes, phase identification, and determination of the crystallite size, internal strain, and lattice parameter during the MA process. The XRD was performed using an X-ray diffractometer (Cu-Kα radiation and wavelength = 0.154 nm). In this study, the Rietveld method was used to calculate the crystallite size, internal strain, and lattice parameter. In this method, the refining process is performed on the X-ray scattering pattern and continues until the errors are reduced. In other words, the best fit is obtained [32]. It should be noted that the Rietveld analysis was performed using MAUD software [33]. The morphology and shape of the milled powders were studied by scanning electron microscope (SEM, cam scan mv2300). Particle size analyzer (Zetasizer, ZEN3600) was used to determine the powders' particle size. Also, the particle size values were reported as an interval. For microhardness measurement, the milled powders were compressed into a cylindrical shape with a dimension of 1 cm in diameter and a thickness of 0.5 cm. It should be noted that the powder particles were compressed at room temperature and a pressure of 12 tons. The heat treatment was then carried out on the pressed specimens up to 450 °C for 30 min under the argon gas atmosphere. Then, the samples were pressed again at 400 °C after sintering. The surfaces of the specimens were first polished, and the Vickers microhardness test was performed based on the ASTM E 348-89 standard by the microhardness tester (Strues Duramin 20). microhardness measurement was performed with a load of 97.8 mN for 5 seconds. The reported microhardness is an average of 5 times the microhardness of each sample. Also, the Archimedes method was used to measure the density of the samples according to the ASTM, C-373 standard [34].

TABLE 1. The Experiment number proposed by Taguchi method

Experiment number	Ball to powder weight ratio	Rotation speed (rpm)	Milling time (h)
1	10	10	200
2	10	30	300
3	10	50	400
4	20	10	300
5	20	30	400
6	20	50	200
7	30	10	400
8	30	30	200
9	30	50	300

3. RESULTS AND DISCUSSION

Fig. 1 shows the XRD patterns of Al–TiC composite powders at different milling conditions. As is evident, Al–4% TiC composite samples include Al and TiC peaks. It was observed that the peak width was increased; however, the peak intensity was decreased due to the milling process, indicating a decrease in the crystallite size and enhancement of the lattice strain in the crystal structure [35]. The powder particles are severely deformed due to the impact of balls during milling [36]. Hence, the work hardening occurred on the powder

particles. On the other hand, after the milling process, the dislocations were regularly arranged, which caused to form the sub-boundaries in the crystal structure. Continuing the milling process and enhancing the dislocation density in the sub-boundaries led to rotating these boundaries and transforming sub-boundaries into the main boundaries [37].

In this research, Bragg's law was used to estimate the Al lattice parameter [38]. The Al lattice parameter at different milling conditions was shown in fig. 2. As can be seen, there is no noticeable change in the Al lattice parameter owing to the milling process and have a constant trend. The lack of displacement of the Al peaks to the left or right indicates that the TiC was not dissolved in the Al lattice, and the TiC particles were distributed in the Al matrix, which led to applying the local strain in the Al lattice and increased the dislocation density.

The changes in the crystallite size and internal strain of Al–4% TiC composite powders at different milling conditions are shown in Fig. 3.

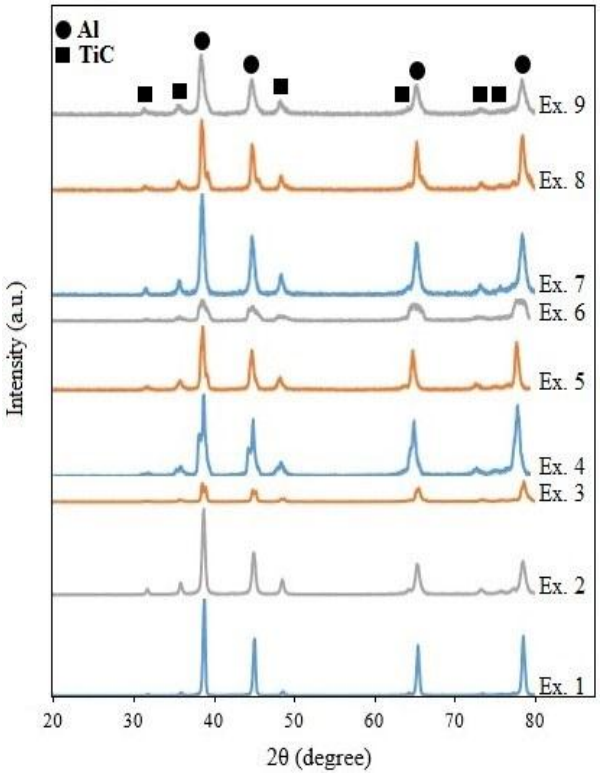

Figure 1. XRD patterns of Al–4% TiC powders milled at different milling conditions

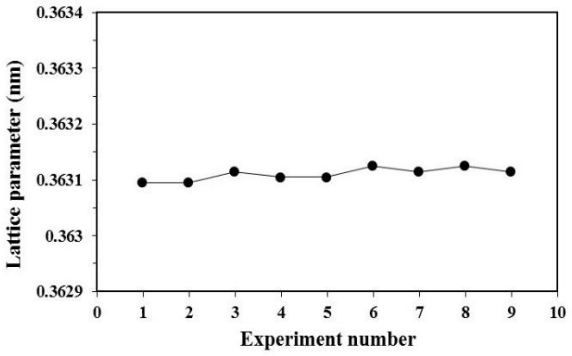

Figure 2. Al lattice parameter changes versus milling condition

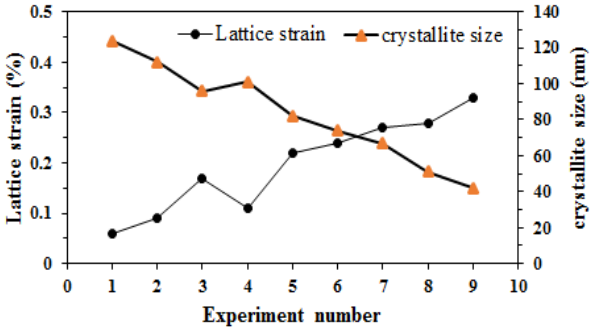

Figure 3. Crystallite size and lattice strain changes of Al at various milling conditions

As shown in this Figure, the crystallite size at each experiment varies according to the milling conditions. Furthermore, at a constant value of the ball to powder ratio, the crystallite size decreased by increasing the milling time and rotation speed. As can be seen, the maximum reduction in the crystallite size is related to experiment number 9 with a ball to powder ratio of 30, a milling time of 50 h, and a rotation speed of 300 rpm. In contrast, the largest crystallite size is associated with experiment number 1 with the lowest milling time. The crystallite size change depended on the plastic deformation and the recovery and recrystallization process [39]. In other words, plastic deformation caused to decrease in the crystallite size; however, the recovery and recrystallization increased the crystallite size. In the present study, the crystallite size of all composite samples decreased after the milling process. The crystallite size range was 42 nm to 124 nm, indicating that the milling process is a proper technique to produce Al–TiC nanocomposite powders. As shown in Fig. 3, the minimum crystallite size of 42 nm is related to experiment number 9 with a ball to powder ratio of 30, a

rotation speed of 300 rpm, and the milling time of 50 h. Furthermore, the maximum crystallite size of 124 nm corresponds to experiment number 1 with the lowest rotation speed of 200 rpm, the milling time of 10 h, and the ball to powder ratio of 10. Since the milling time, the ball to powder ratio, and rotation speed were increased, the lattice defects, internal strain, and the stored energy were increased [40], reducing the crystallite size. The milling significantly increased the strain after the milling process. As can be seen, the strain range of the crystal structure was from 0.06% to 0.33%, which the largest strain was corresponding to experiment number 9.

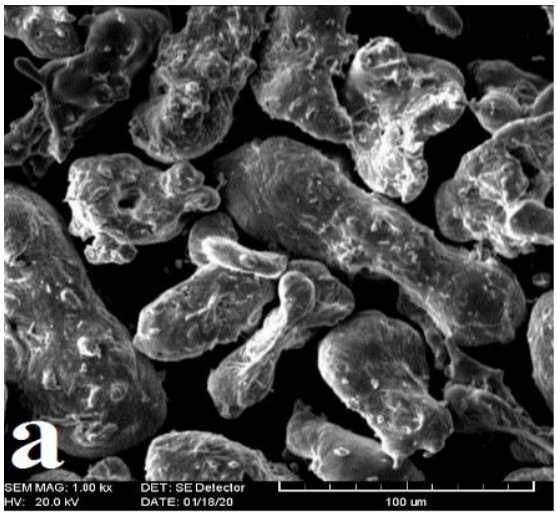

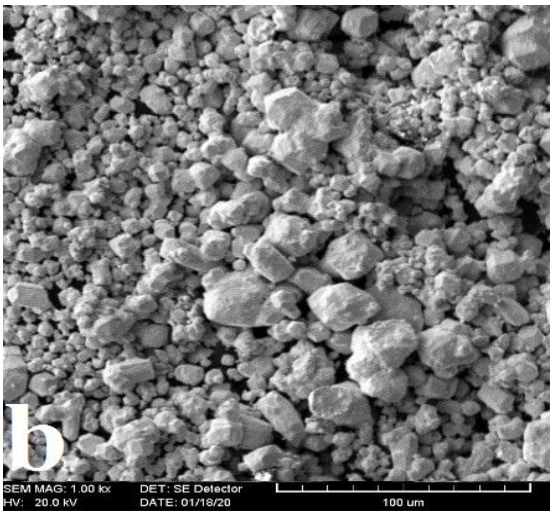

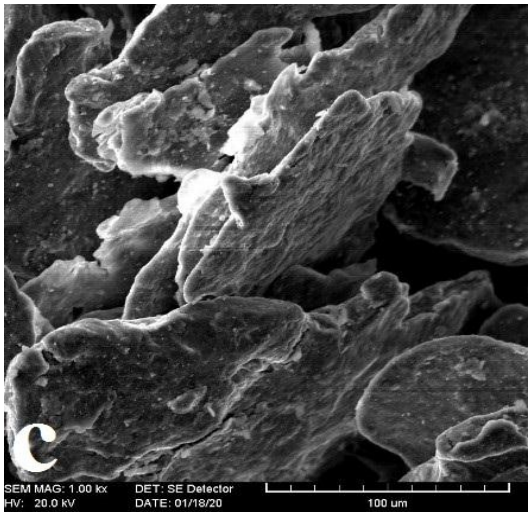

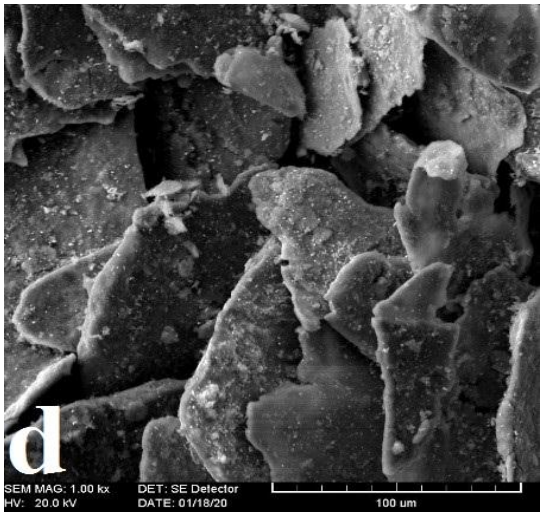

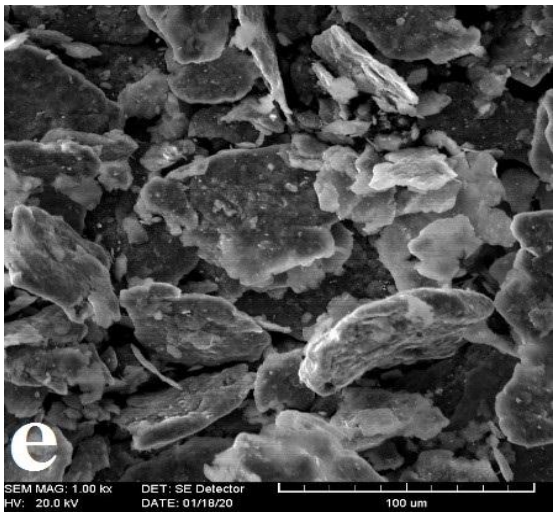

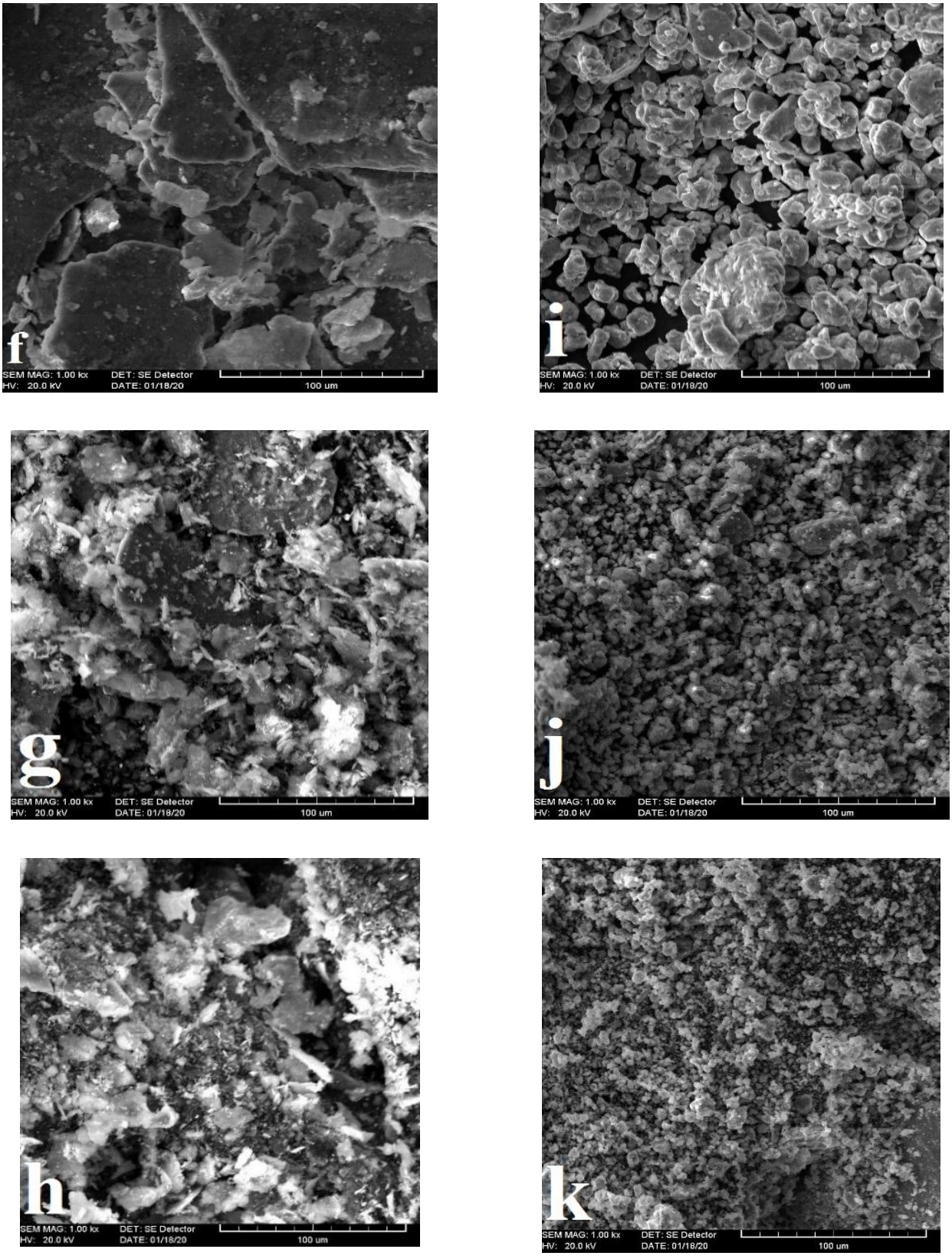

Figure 4. SEM images of Al–4% TiC powders at different milling conditions

Fig. 4 shows the SEM images of the pure Al, TiC, and Al–TiC composite powder particles at different milling conditions. Due to the low value of dislocation density at the beginning of the milling process, the particles were soft and high energy was applied to the powder particles during the MA process. This high energy increased plastic deformation in particles, and powder morphology was shaped as lamellar. In fact, a microforging mechanism caused to overspread the powder particles. Then, cold welding and mechanical joining between the powder particles occurred due to the impacts by the balls. As the milling time increased, dislocation density increased which caused to increase the work hardening of powders. Also, SPD led to form the sessile dislocations and resultantly changed to a mircocrack generation resource. The outcome of these parameters increased the fracture of powder particles and the particle size decreased. In other words, the powder particle fracture phenomenon dominated cold welding and particles size decreased. Finally, the powder particles reached the spherical state and are dispersed more orderly. In fact, the lamella thicknesses decreased due to the continuous deformation, and also, the number of the lamella in one particle increased. Therefore, the diffusion distances decreased. On the other hand, the temperature of powder particles could locally increase due to the energy transfer of the balls. Consequently, the reduction in diffusion distance, the local temperature rise, and the increment of the lattice defects resulted in more diffusion of atoms [37]. As shown in Fig. 4 (a), Al powder particles have an irregular shape and a particle size of 18-130 µm while TiC powders are spherical shape with a particle size of about 1.8-26 µm (Fig. 4 (b)). The powder particles related to experiment number 1 have the largest particle size of about 88-132 µm, thick plate-shaped particles (Fig. 4 (c)). Al powder particles were very soft before milling, and on the other hand, the low energy of milling led to overspread the powder particles. In other words, applied strain due to the milling process caused the powder particles were pressed, and wide particles were cold welding to each other, and finally, the particle size was increased. According to the low energy at experiment number 1 (speed=200, BPR=10, and time=10), the particle size was enhanced compared to the particle size of pure Al. At experiment number 2, the size of the plate-shaped particles was obtained to be about 15-108 µm (Fig. 4 (d)). Also, after experiment number 3, the thickness of the plate-shaped particles was lower than that of experiment number 2, and the particles were irregularly distributed with a size of 3-64 µm (Fig. 4 (e)). The size of plate-shaped particles related to experiment number 4 was found to be 1-100 µm approximately (Fig. 4 (f)).

In experiment number 5, the morphology of powder particles was the combination of plate shape, fine needle, and quasi-spherical with a particle size of 0.5-65 µm (Fig. 4 (g)). In the mechanical milling process, two phenomena of cold welding and fracture occur between powder particles, so that cold welding led to coarsening of the powders while fracture caused to reduction the particle size. The occurrence of these phenomena depended on the properties of powders and the milling. If the powders are brittle, the fracture overcomes the cold welding, and the powders become smaller as the milling time increased, while cold welding is a dominant phenomenon in the soft powders at the beginning of milling. Of course, at longer milling times, the powders get work hardening, leading to powders' fracture and particle size reduction. TiC powder particles were brittle and fractured due to the severe strain during the milling process. Therefore, the reinforcement particles were placed among the Al matrix, which led to work hardening of Al powder particles and reducing the particle size of composite powders. At experiment number 6 (Fig. 4 (h)), the irregular distribution of fine and coarse particles was seen at the particle size range of 0.5-49 µm. As observed in Fig. 4 (i), the particle size was reduced to about 1-39 µm, and the morphology of particles is fine plate-shaped and equiaxed. At experiment numbers 8 and 9, the particles were spherical and regularly distributed with particle sizes about 0.2-59 µm (Fig. 4 (j) and Fig. 4 (k)), indicating that the fracture is a dominant mechanism at this step of milling.

The microhardness values of nanocomposite specimens are shown in Fig. 5. As observed, the microhardness of Al–4% TiC nanocomposite related to experiment number 9 is equal to about 271 HV, which is the maximum microhardness value, and the lowest microhardness is corresponding to experiment number 1 with a value of 221 HV. As the BPR, rotation speed, and milling time were increased, the consolidation behavior of nanocomposite specimens noticeably improved, leading to increased microhardness. It should be noted that the main strengthening mechanisms are the work hardening owing to hard TiC particles within the Al matrix. Also, the lack of dislocation motion during plastic deformation and crystallite refinement can significantly increase the microhardness. It should be noted that the microhardness is affected by the parameters of the ball to powder ratio, milling speed, and milling time and the microhardness does not depend only on the milling speed. Therefore, it can be concluded that the change in microhardness was dependent on the three parameters includes the ball to powder ratio, milling time, and milling speed. The density of the nanocomposites was close to about 94%-98% of the theoretical density. Then, the porosity of the samples was determined by density of sintered sample and theoretical density. The result showed that the porosity of the samples was in the range of 0.02%-0.06%. It should be noted that the theoretical density was determined by the mixtures law.

Fig. 6 shows the results of the microhardness value obtained from the experimental measurement and the data predicted by the Taguchi method. As can be seen,

there is good compatibility between the experimental data and the predicted data. So, it can be concluded that the linear regression model can predict the response parameters. The results of variance analysis related to the microhardness values are presented in Table 2. It should be noted the coefficient of A, B, and C indicate the BPR, the milling time, and the rotation speed, respectively. Also, some statistical data obtained from variance analysis are given in Table 3.

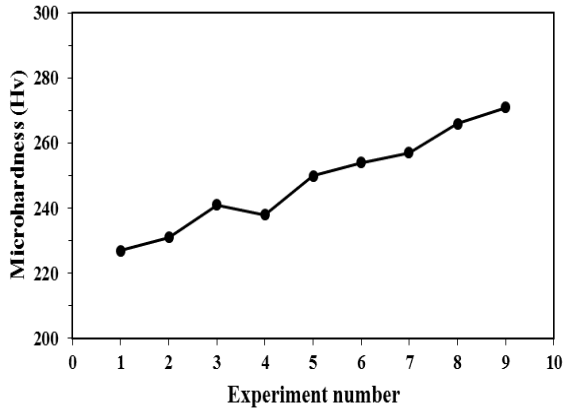

Figure 5. Vickers microhardness values of Al–4% TiC nanocomposites after various milling conditions

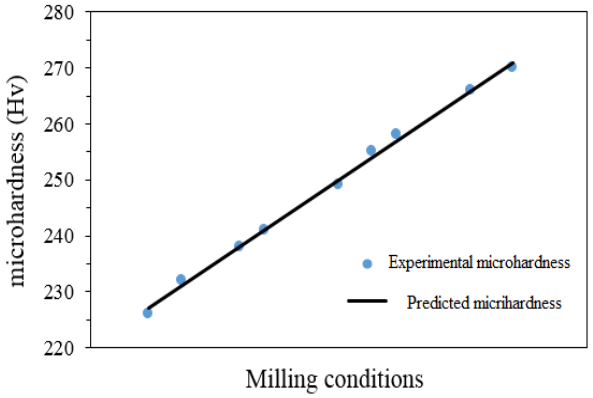

Figure 6. The microhardness values obtained from experimental measurement and Taguchi method

The compatibility of the proposed model and the experimental data is determined by the correlation coefficient (R^2) so that the high value of R^2 (98.7) indicated the good compatibility between the experimental data and the predicted data. The relationship between the process response and the variables number of K in the experiment design is as follows:

$$Y = b_0 \sum_{i=1}^{k} b_i x_i + \varepsilon \quad (1)$$

TABLE 2. The values of Sum of square, Degree of free, Mean square, F-value, and P-value calculated by variance analysis for validation of the proposed model

Source	Sum of square	Degree of free	Mean square	F-value	P-value
Model	1904	3	615	105.4	0.01
A	2242.7	2	1123.6	28.8	0.003
B	448.2	1	472.6	148.5	0.019
C	0.3	1	0.3	99.4	0.03
Error	21	5	5		
Total	1886	8			

TABLE 3. The values of R-parameters estimated by variance analysis

Pred. R-Squared	Adj. R-Squared	R-Squared
95.7%	97.8%	98.7%

Where Y is the process response, b_i is the model parameters, and ε is the error value. The model coefficients are calculated by the Minitab software. The values of model coefficients indicated the effect of the variable on the process response. According to the model coefficients, the ball to powder ratio has the most significant effect on the microhardness value. The effect of milling parameters on the microhardness of Al–4% TiC nanocomposites are shown in Fig. 7. As can be seen, this diagram illustrates the levels of input parameters that have created the maximum and minimum values of microhardness.

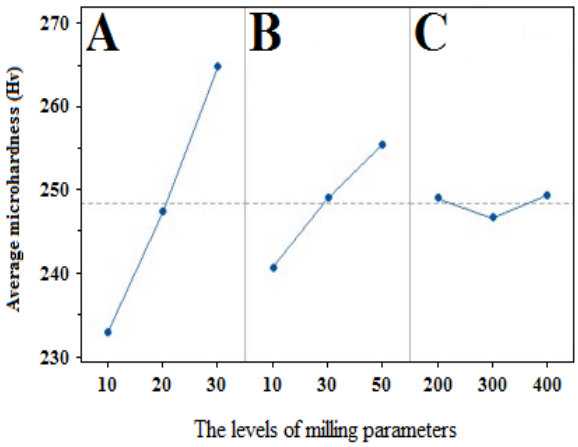

Figure 7. The effect plot of the milling parameters on the microhardness of Al–4% TiC composites

As previously discussed, nine experiments were designed to investigate the effect of milling parameters on the mechanical properties of the Al–4% TiC composites. The P-value in the variance analysis is the smallest level of confidence that leads to the rejection or acceptance of the proposed model. In this research, the P-value was less than 0.05 (95% confidence level), indicating that the proposed model was meaningful and can predict the microhardness values of Al–4% TiC composites. Adj-R^2 (97.8) indicated that 3% of the response changes could not be described with the model. Also, Pred-R^2 indicated a 95% probability of predicting new observations, which had good compatibility with Adj-R^2. The degree of compatibility between the experimental results and prediction results is shown in Fig. 6. As can be seen, there is good compatibility among the prediction data and experimental values. The value of error indicates the deviation of the predicted microhardness from the experimental microhardness. According to the results of this study, it is observed that the predicted and experimental microhardness are consistent. The value of model coefficients indicated the effect degree of the variables on the response. A positive sign of the coefficient indicated a positive effect, and a negative sign indicated an upside-down effect. Based on the coefficients, the proposed model based on the intended variables is as follows:

$$\text{Hardness} = 199.34 + 1.574\ A + 0.332\ B + 0.0015\ C \quad (2)$$

It is observed that the parameters of the ball to powder ratio (A), milling time (B), and milling speed (C) have a positive effect on the hardness. In other words, all three main variables of milling have a meaningful effect on the response.

The diagram of the effect of milling parameters on the microhardness of composites is shown in fig. 7. As can be seen, the highest microhardness of the composites is obtained in the ball to powder ratio of 30, milling time of 50 h, and a milling speed of 400 rpm. Based on these results, it can be expected that the obtained model can predict the microhardness of the composites at other milling conditions with high accuracy, and also experimental design can reduce the time and cost of Al–4% TiC nanocomposite production. The microhardness may be increased by increasing the ball to powder ratio, milling speed, and milling time. However, based on the present conditions, the microhardness was determined, and the result was optimized.

4. CONCLUSION

In this study, Al–4% TiC nanocomposite powders were produced by the mechanical milling process. Furthermore, sintering treatment at the temperature of 450 °C was used for the consolidation of the powder mixtures. Subsequently, based on the experimental design, various conditions of the milling process, including the BPR of 10:1, 20:1, and 30:1, speeds of 200, 300, and 400 rpm, and milling time of 10, 30, and 50 h were considered the input data to finding the maximum microhardness. According to the experimental design, nine experiments were designed by the Taguchi method at certain milling parameters. The results showed that the mechanical milling led to form the Al–4% TiC nanocomposite with a maximum microhardness of about 271 HV. Furthermore, there was good compatibility between the experimental microhardness values and the predicted results by the proposed model by Minitab software. According to the predicted model, the highest microhardness was obtained in the BPR of 30: 1, the milling time of 50 h, and the speed of 400 rpm. In addition, SEM observation indicated that the morphology, particle size, and distribution of powder particles could significantly affect the mechanical properties of the Al–4% TiC nanocomposite so that the maximum microhardness occurred at experiment number 9, which at this condition, the particles were spherical shape and regularly distributed with particle size about 0.2-59 µm. Also, it can be concluded that the properties of the composites were changed because the test conditions of the milling process are different. In general, the mechanical properties of the composite are due to the change in powder morphology, particle size, lattice strain, and crystallite size.

ACKNOWLEDGEMENTS

The author would like to acknowledge the Department of Materials Science and Engineering, Shahid Bahonar university of Kerman for their contribution to this study.

REFERENCES

1. Taghian Dehaghani, M., Ahmadian, M., “Fracture Mechanism of CoCrMo Porous Nanocomposite Prepared by Powder Metallurgy Route”, ***International Journal of Engineering***, Vol. 31, No. 1, (2018), 19-24. https://doi.org/10.5829/ije.2018.31.01a.03
2. Ameri Ekhtiarabadi, T., Zandrahimi, M., Ebrahimifar, H., “The Impact of Current Density of Electroplating on Microstructure and Mechanical Properties of Ni-ZrO_2-TiO_2 Composite Coating”, ***Advanced Ceramics Progress***, Vol. 6, No. 1, (2020), 22-29. https://doi.org/10.30501/acp.2020.105929
3. Nahvi, S. M., “Effect of Carbide Particle Size on the Microstructure, Mechanical properties, and Wear Behavior of HVOF-sprayed WC-17% Co Coatings”, ***Advanced Ceramics Progress***, Vol. 6, No. 3, (2020), 1-14. https://doi.org/10.30501/acp.2020.227010.1033
4. Khoshhal, R., “The Effect of Raw Material Ratios on the Fe-TiC/Al_2O_3 Composite Formation Mechanism”, ***Advanced***

Ceramics Progress, Vol. 3, No. 2, (2017), 25-30. https://doi.org/10.30501/acp.2017.90749

5. Mortazavi, A., Razavi, M., Ebadzadeh, T., Sedaghat Ahangari Hossein Zadeh, A., "Effect of Milling Time on the Crystallite Size and Microstructure of Al_2O_3/Mo Nanocomposite", ***Advanced Ceramics Progress***, Vol. 2, No. 3, (2016), 12-16. https://doi.org/10.30501/acp.2016.70025
6. Sasani, N., Houshyar Sadeghian, M., Khadivi, H., Golestanipour, M., "A Novel, Simple and Cost Effective Al A356/Al_2O_3 Nano-composite Manufacturing Route with Uniform Distribution of Nanoparticles", ***International Journal of Engineering***, Vol. 28, No. 9, (2015), 1320-1327. https://doi.org/10.5829/idosi.ije.2015.28.09c.09
7. Kaushik, N., Singhal, S., "Experimental Investigations on Microstructural and Mechanical Behavior of Friction Stir Welded Aluminum Matrix Composite", ***International Journal of Engineering***, Vol. 32, No. 1, (2019), 162-170. https://doi.org/10.5829/ije.2019.32.01a.21
8. Mitra, R., Chiou, W. A., Fine, M. E., Weertman, J. R., "Interfaces in as-extruded XD Al/TiC and Al/TiB_2 metal matrix composites", ***Journal of Materials Research***, Vol. 8, No. 9, (1993), 2380-2392. https://doi.org/10.1557/jmr.1993.2380
9. Arefkhani, M., Razavi, M., Rahimipoor, M. R., Faeghinia, A., "The Effect of Rotation Speed on the Microstructure and Hardness of Synthesized Al-WC Nano-Composite by Centrifugal Casting", ***Advanced Ceramics Progress***, Vol. 2, No. 4, (2016), 1-6. https://doi.org/10.30501/acp.2016.70031
10. Aswad, M. A., Awad, S. H., Kaayem, A. H., "Study on Iraqi Bauxite Ceramic Reinforced Aluminum Metal Matrix Composite Synthesized by Stir Casting", ***International Journal of Engineering***, Vol. 33, No. 7, (2020), 1331-1339. https://doi.org/10.5829/ije.2020.33.07a.20
11. Mitra, R., Fine, M. E., Weertman, J. R., "Chemical reaction strengthening of Al/TiC metal matrix composites by isothermal heat treatment at 913 K", ***Journal of Materials Research***, Vol. 8, No. 9, (1993), 2370-2379. https://doi.org/10.1557/jmr.1993.2370
12. Mahdavi, M., Khayati, G. R., "Artificial Neural Network Based Prediction Hardness of Al2024-Multiwall Carbon Nanotube Composite Prepared by Mechanical Alloying", ***International Journal of Engineering***, Vol. 29, No. 12, (2016), 1726-1733. https://doi.org/10.5829/idosi.ije.2016.29.12c.11
13. Kuldeep, B., Ravikumar, K. P., Pradeep, S., "Effect of Hexagonal Boron Nitrate on Microstructure and Mechanical Behavior of Al7075 Metal Matrix Composite Producing by Stir Casting Technique", ***International Journal of Engineering***, Vol. 32, No. 7, (2019), 1017-1022. https://doi.org/10.5829/ije.2019.32.07a.15
14. Abbasi, N. F., Azari, K. R., Parvini, A. N., "Synthesis of Nanostructure Ti-45Al-5Cr Alloy by Mechanical Alloying and Study the Effect of Cr Addition on Microstructure of TiAl Alloy", ***International Journal of Engineering***, Vol. 24, No. 2, (2011), 123-130. http://www.ije.ir/article_71898_21fccba5f3ee974387c9075597c7cba7.pdf
15. Rahaei, M. B., Yazdani-Rad, R., Kazemzadeh, A., "Synthesis and Characterization of Nanocrystalline Ni_3Al Intermetallic during Mechanical Alloying Process", ***International Journal of Engineering***, Vol. 25, No. 2, (2012), 89-98. https://doi.org/10.5829/idosi.ije.2012.25.02c.01
16. El-Eskandarany, M. S., "***Mechanical Alloying: Nanotechnology: Materials Science and Powder Metallurgy***", 2nd Ed., Elsevier, Oxford, UK, (2015). http://refhub.elsevier.com/S2468-6069(16)30018-1/sref4
17. Akbari, G. H., Taghian Dehghani, M., "Behavior of Cu-Cr Powder Mixtures During Mechanical Alloying", ***International Journal of Engineering***, Vol. 23, No. 1, (2010), 69-76. http://www.ije.ir/article_71834_380c6a8afec5b5dce8b0fb8825ecf6b5.pdf
18. Nikzad, L., Ghofrani, S., Majidian, H., Ebadzadeh, T., "Effect of ball milling on reactive microwave sintering of MgO-TiO_2 System", ***Advanced Ceramics Progress***, Vol. 2, No. 3, (2016), 25-28. https://doi.org/10.30501/acp.2016.70027
19. Akbarpour Arbatan, M. R., Leisi Azar, F., Alipour, S., "Fabrication of Nanostructured Cu matrix Nanocomposites by High Energy Mechanical Milling and Spark Plasma Sintering", ***Advanced Ceramics Progress***, Vol. 1, No. 3, (2015), 39-43. https://doi.org/10.30501/acp.2015.70011
20. Lou, T., Fan, G., Ding, B., Hu, Z., "The synthesis of $NbSi_2$ by mechanical alloying", ***Journal of Materials Research***, Vol. 12, No. 5, (1997), 1172-1175. https://doi.org/10.1557/jmr.1997.0162
21. Golzar Shahri, M., Shafyei, A., Saidi, A., Abtahi, K., "Effect of CaO on the Formation of PSZ and γ-Zirconia Nanoparticles through Ball Milling", ***Advanced Ceramics Progress***, Vol. 1, No. 2, (2015), 40-44. https://doi.org/10.30501/acp.2015.90747
22. Azimi, A., Shokuhfar, A., Nejadseyfi, O., "Mechanically alloyed Al7075–TiC nanocomposite: Powder processing, consolidation and mechanical strength", ***Materials & Design (1980-2015)***, Vol. 66, (2015), 137-141. https://doi.org/10.1016/j.matdes.2014.10.046
23. Feijoo, I., Merino, P., Pena, G., Rey, P. and Cabeza, M., "Microstructure and Mechanical Properties of an Extruded 6005A Al Alloy Composite Reinforced with TiC Nanosized Particles and Strengthened by Precipitation Hardening", ***Metals***, Vol. 10, No.8, (2020), 1050. https://doi.org/10.3390/met10081050
24. Salem, H. G., El-Eskandarany, S., Kandil, A., Abdul Fattah, H., "Bulk Behavior of Ball Milled AA2124 Nanostructured Powders Reinforced with TiC", ***Journal of Nanomaterials***, Vol. 1, (2009), 479185. https://doi.org/10.1155/2009/479185
25. Rezaei, A. R., Mobasherpour, I., Hadavi, M. M., "An Investigation on Milling Method in Reduction of Magnesium Nano-Powder Particles Based on Sustaining Chemical Activity", ***Advanced Ceramics Progress***, Vol. 4, No. 1, (2018), 12-17. https://doi.org/10.30501/acp.2018.90828
26. Pérez-Bustamante, R., Pérez-Bustamante, F., Estrada-Guel, I., Santillán-Rodríguez, C. R., Matutes-Aquino, J. A., Herrera-Ramírez, J. M., Miki-Yoshida, M., Martínez-Sánchez, R., "Characterization of Al2024-CNTs composites produced by mechanical alloying", ***Powder Technology***, Vol. 212, (2011), 390–396. https://doi.org/10.1016/j.powtec.2011.06.007
27. Zuhailawati, H., Mahani, Y., "Effects of milling time on hardness and electrical conductivity of in situ Cu–NbC composite produced by mechanical alloying", ***Journal of Alloys and Compounds***, Vol. 476, No. 1-2, (2009), 142–146. https://doi.org/10.1016/j.jallcom.2008.09.018
28. Barzegar, M., Vishlaghi, A. A., "Investigation on solid solubility and physical properties of Cu–Fe/CNT nano-composite prepared via mechanical alloying route", ***Powder Technology***, Vol. 47, (2014), 37–42. https://doi.org/10.1016/j.powtec.2014.08.010
29. Sorkhe, Y. A., Aghajani, H., Tabrizi, A. T., "Mechanical alloying and sintering of nanostructured TiO_2 reinforced copper composite and its characterization", ***Materials and Design***, Vol. 58, (2014), 168–174. https://doi.org/10.1016/j.matdes.2014.01.040
30. Sahani, P., Mula, S., Roy, P. K., Kang, P. C., Koch, C. C., "Structural investigation of vacuum sintered Cu–Cr and Cu–Cr–4% SiC nanocomposites prepared by mechanical alloying", ***Materials Science and Engineering: A***, Vol. 528, No. 25-26, (2011), 7781– 7789. https://doi.org/10.1016/j.msea.2011.06.086
31. Basariya, M. R., Srivastava, V. C., Mukhopadhyay, N. K., "Microstructural characteristics and mechanical properties of carbon nanotube reinforced aluminum alloy composites produced by ball milling", ***Materials and Design***, Vol. 64, (2014), 542–549. https://doi.org/10.1016/j.matdes.2014.08.019
32. Dekhil, L., Alleg, S., Bououdina, M., Suñol, J. J., Grenèche, J. M., "Phase transformations and magnetic properties of ball-milled Fe-6P-1.7C powders", ***Advanced Powder Technology***, Vol. 26, No. 2, (2015), 519-526. https://doi.org/10.1016/j.apt.2014.12.011

33. Lutterotti, L., Matthies, S., Wenk, H. R., "MAUD: A friendly java program for material analysis using diffraction", ***IUCr: Newsletter of the CPD***, Vol. 21, (1999), 14-15. https://www.iucr.org/__data/assets/pdf_file/0016/21634/cpd21.pdf
34. Kumar, A. A., Patton, M. R., Hennek, J. W., Lee, S. Y. R., Alesio-Spina, G. D., Yang, X., Kanter, J., Shevkoplyas, S. S., Brugnara, C., Whitesides, G. M., "Density-based separation in multiphase systems provides a simple method to identify sickle cell disease", ***Proceedings of the National Academy of Sciences***, Vol. 111, No. 41, (2014), 14864-14869. https://doi.org/10.1073/pnas.1414739111
35. Patankar, S. N., Xiao, S. Q., Lewandowski, J. J., Heuer, A. H., "The mechanism of mechanical alloying of $MoSi_2$", ***Journal of Materials Research***, Vol. 8, No. 6 (1993), 1311-1316. https://doi.org/10.1557/jmr.1993.1311
36. Schoenitz, M., Dreizin, E. L., "Structure and properties of Al-Mg mechanical alloys", ***Journal of Materials Research***, Vol. 18, No. 8, (2003), 1827-1836. https://doi.org/10.1557/jmr.2003.0255
37. Dieter, G. E., Bacon, D. J., "***Mechanical Metallurgy***", Vol. 3, New York: McGraw-Hill, (1986). https://dokumen.tips/documents/mechanical-metallurgy-by-dieterpdf.html
38. Cullity, B. D., Stock, S. R., "***Elements of X-ray Diffraction***", 3rd Eds., Prentice-Hall, New York, (2001). https://www.pearson.com/us/higher-education/program/Cullity-Elements-of-X-Ray-Diffraction-3rd-Edition/PGM113710.html
39. Eckert, J., Holzer, J. C., Krill, C. E., Johnson, W. L., "Structural and thermodynamic properties of nanocrystalline fcc metals prepared by mechanical attrition", ***Journal of Materials Research***, Vol. 7, No. 7, (1992), 1751-1761. https://doi.org/10.1557/jmr.1992.1751
40. Suryanarayana, C., "Mechanical alloying and milling", ***Progress Materials Science***, Vol. 46, No. 1-2, (2001), 1-184. https://doi.org/10.1016/s0079-6425(99)00010-9

Advanced Ceramics Progress: Vol. 7, No. 1, (Winter 2021) 46-51

Advanced Ceramics Progress

Research Article

Journal Homepage: www.acerp.ir

Heat Treatment of Pulsed Electroplated Nickel Deposited on AA2024 Aluminum

A. Khiabani [a], Z. S. Seyedraoufi [a]*, M. Heydarzadeh Sohi [b]

[a] *Department of Metallurgy and Materials Engineering, Karaj Branch, Islamic Azad University, Karaj, Alborz, Iran*
[b] *School of Metallurgy and Materials, College of Engineering, University of Tehran, Tehran, Tehran, Iran*

ARTICLE INFO

Article History:

Received 14 May 2021
Received in revised form 16 June 2021
Accepted 29 June 2021

Keywords:

AA2024 A luminum
Pulse Electroplating
Heat Treatment
Al_3Ni Intermetallic Compound
Corrosion

ABSTRACT

In this study, pure nickel was deposited on AA2024 aluminum via pulsed electrodeposition using two duty cycles (25 % and 50 %) at two different frequencies (50 and 100 Hz). The coated specimens were then heat-treated in an argon atmosphere at 500 °C for one hour. The treated specimens were characterized using Optical Microscope (OM), Scanning Electron Microscope (SEM) equipped with energy dispersive spectrometer (EDS), and X-Ray Diffraction (XRD) analysis. According to the results, the coatings were thickened upon increasing the duty cycle and frequency. Heat treatment of the nickel-coated specimen under the duty cycle of 25 % and frequency of 50 Hz experienced formation of Al_3Ni intermetallic compound at the interface of the nickel coating and aluminum-based substrate. Heat treatment adversely affected the corrosion resistance of the nickel-coated specimens. Nevertheless, the specimens with Al_3Ni intermetallic compound at their interface demonstrated better corrosion resistance among heat-treated materials.

https://doi.org/10.30501/ACP.2021.252211.1048

1. INTRODUCTION

Aluminum alloys have a wide range of applications, especially in automotive and aerospace industries, due to their superior properties such as high strength-to-weight ratio, corrosion resistance, and electrical and thermal conductivities [1]. However, these alloys suffer from poor tribological properties and inadequate corrosion resistance in some applications [2]. Different surface modifications and coating technologies have been assessed and applied on these alloys to overcome the aforementioned deficiencies.

Anodizing [3], electroplating [4], plasma nitriding [5], ion implantation [6], physical vapor deposition [7], diffusional coatings [8], thermal spray coatings [9], and liquid phase surface treatments [10] are among the different surface engineering processes that have been applied on these alloys. Electroplating is among the cheapest coating technologies. A number of metallic elements including cupper, chromium, and nickel have been electrodeposited on aluminum alloys using both direct and pulse currents so far [4,11]. In addition, a number of composite coatings have been deposited on these alloys through electroplating [4,12,13]. Diffusion coatings by means of electroplating followed by heat treatment have also been investigated by a number of researchers. These coatings might enjoy better adhesion to the substrate as well as higher hardness. Therefore, diffusional coatings could affect both corrosion and wear resistances of the treated materials [14-16].

Amadeh [17] and Lee [18] et al. studied the effects of heat treatment on electrodeposited nickel coating on 6061 aluminum alloy and reported the formation of Al_3Ni_2 and Al_3Ni, the intermetallic compounds on the treated layers, which could reduce corrosion resistance. Presd et al. also applied the above process on A352 aluminum and reported similar results [19]. There is little or no information on the application of pulse current for electrodeposition metallic elements prior to heat treatment in diffusional coatings. Therefore, in this study, nickel was pulse-electrodeposited on 2024 aluminum alloy before being heat treated. In addition, the effect of the duty cycle and frequency was evaluated.

* Corresponding Author Email: z.seyedraoufi@kiau.ac.ir (Z. S. Seyedraoufi)
https://www.acerp.ir/article_132766.html

Please cite this article as: Khiabani, A., Seyedraoufi, Z. S., Heydarzadeh Sohi, M., "Heat Treatment of Pulsed Electroplated Nickel Deposited on AA2024 Aluminum", ***Advanced Ceramics Progress***, Vol. 7, No. 1, (2021), 46-51. https://doi.org/10.30501/ACP.2021.252211.1048

2. MATERIALS AND METHODS

In this study, 20×20×4 mm specimens were cut out from AA2024 aluminum alloy (with a composition containing 4.41 wt.% Cu, 1.52 wt.% Mg, 0.50 wt.% Mn, 0.09 wt.% Si, 0.02 wt.% Fe, 0.02 wt.% Cr, and 0.20 wt.% Zn), and they were used as the substrates. Figure 1 shows the microstructure of the received substrate. Based on the studies by Goli et al. and Ghorbanzadeh et al., the precipitates identified by the red circle appear to be copper-rich compounds [20,21].

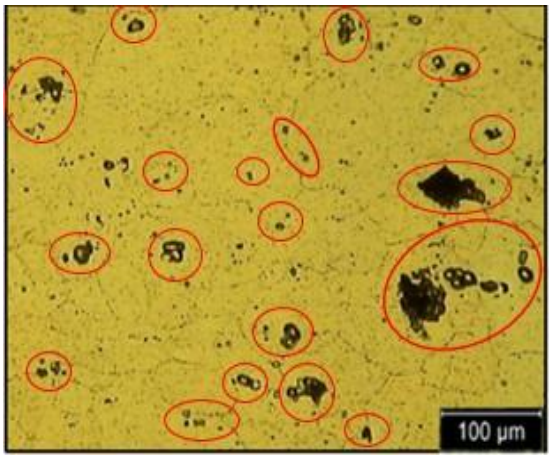

Figure 1. Optical micrograph of the AA2024 aluminum substrate

The specimens were then cleaned and polished with Emery paper up to 1200 grades. After washing the specimens with acetone, they were etched in a solution containing 50 g/L sodium hydroxide at 70 °C for 15 seconds and then washed in water. This step was repeated with a 65 % nitric acid solution for 5 seconds. At the final stage of the substrate preparation, the samples were immersed in zincate solution for 20 seconds (containing 2 g/L $FeCl_2$, 5 g/L $CuSO_4$, 40 g/L $KHC_4H_4O_6$, 10 g/L KCN, 106 g/L NaOH, 40 g/L $ZnSO_4$, and 30 g/L $Ni(SO_4)_2$).

Pulse electroplating was applied to nickel plating using Watts bath. The chemical composition of the bath is given in Table 1. A pure nickel sheet was used as anode, and the distance between AA2024 cathode and anode was fixed at 4 cm. The pH of the bath was 4 and its temperature was kept in the range of 45-55 °C. The current density was 2 A/dm^2 and the plating time was 15 minutes. Electroplating was performed at two pulse frequencies of 50 and 100 Hz and in two duty cycles of 25 and 50 %. After plating, the samples were heat-treated in a furnace under an argon gas atmosphere with a purity of 99.99 % at a temperature of 500 °C for 60 minutes. Table 2 shows the coding of the specimens according to their process conditions.

TABLE 1. Composition of Watts nickel plating bath

Brightener	50 g/L
Nickel sulfate ($NiSO_4·6H_2O$)	400 g/L
Boric acid (H_3BO_3)	50 g/L
Nickel chloride ($NiCl_2·6H_2O$)	100 g/L

TABLE 2. Specimen's coding based on process parameters

Sample's Code	Frequency (Hz)	Duty Cycle (%)	Heat treatment
P1	50	25	None
P2	100	50	None
PH1	50	25	Yes
PH2	100	50	Yes

The surface morphology and cross-sectional area of the electroplated and heat-treated specimens were examined by a VEGA/TESCAN Scanning Electron Microscope (SEM) equipped with Energy Dispersive Spectroscopy (EDS) analyzer. Phase analysis of the specimens was performed by PHILIPS PW1730 X-Ray Diffractometer (XRD) using a Cu K_α with a wave length of 1.54056 angstrom and a scanning speed of 0.05 degrees per second.

Polarization test was used to study the corrosion behavior of the coatings. Corrosion tests were performed in a 3.5 % NaCl solution. All potentials in this study were measured relative to Ag/AgCl. In all experiments, the solution temperature was 25 °C, and the sweeping speed was 1 mV/s. Before starting the test, the samples were immersed in the solutions for 1 hour.

3. RESULTS AND DISCUSSION

SEM images in Figure 2A-D show surface morphologies of the nickel-plated specimens before (P1 and P2) and after heat treatment (PH1 & PH2), respectively. Colonies of deposited nickel are observed in these images. In Figure 2C and D, the distances between the colonies are reduced, which may be due to the growth of the colonies. Heat treatment at high temperature and sufficient time results in a more or less proper diffusion and crystallites growth in the coating that leads to the agglomeration and enlargement of the colonies [22].

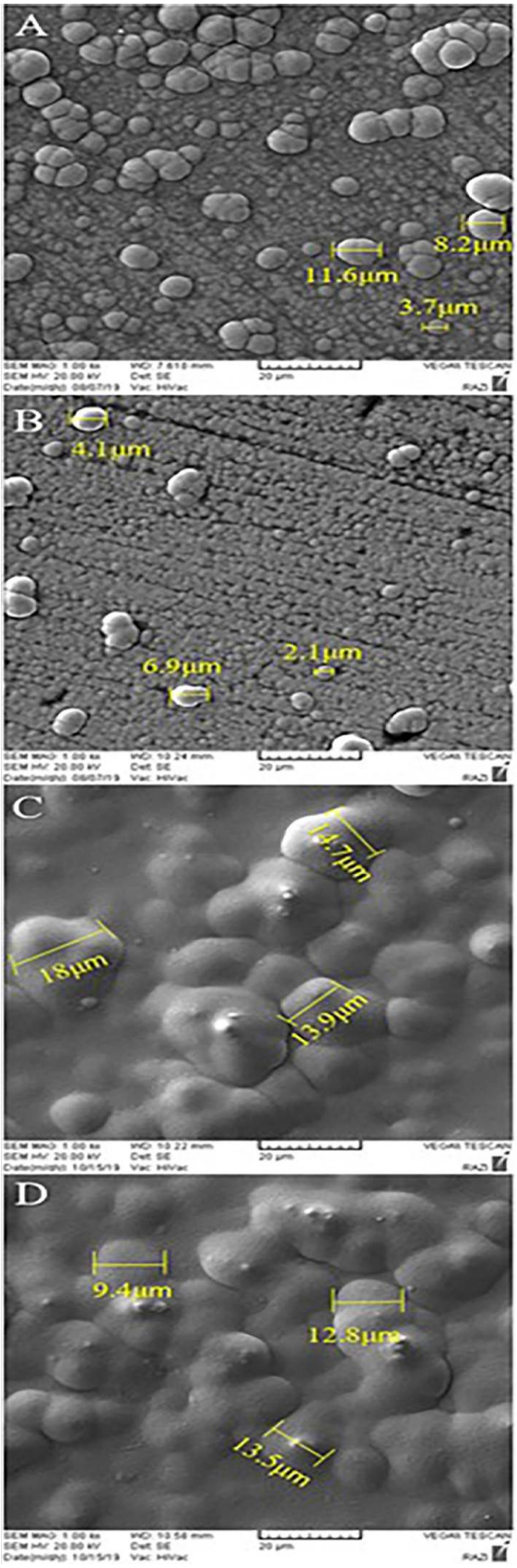

Figure 2. SEM images after electroplating and heat treatment: A) P1, B) P2, C) PH1, and D) PH2

Figure 3A-B shows SEM cross-sectional micrographs of the nickel electrodeposited specimens achieved in two different conditions of P1 and P2, indicating that the coating is thickened by increasing frequency and duty cycle. On the whole, as the duty cycle increases, the current on time increases and the off-time reduces. This situation leads to the formation of a thicker layer. On the other hand, increasing frequency results in a shorter pulse duration that leads to a thinner diffusion layer. Thus, transformation and diffusion of metal ions from the electrolyte to the surface of the cathode become easier. Therefore, increasing the pulse frequency can result in the thickening of the deposited layer [25]. The type of the frequency applied in pulse electrodeposition also affects the thermodynamics and kinetics of electrochemical reactions, consequently influencing the deposit's characteristics and properties such as wear and corrosion resistances [23-24].

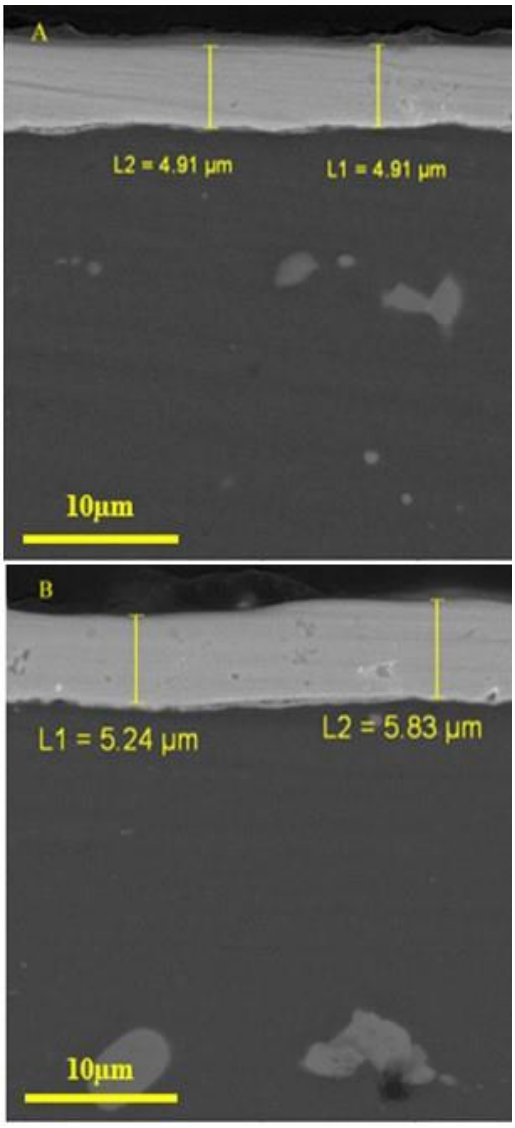

Figure 3. Cross-sectional SEM images of A) P1 and B) P2

Figure 4 illustrates the cross-sectional SEM images of the PH1, PH2 specimens and the result of the EDS analysis at the interface of the heat-treated PH2 specimen. As shown in Figure 4, a relatively thin layer has been formed at the interface between the coating and the substrate in the PH1 specimen, while this layer did not develop in the PH2 specimen. The reason for these structural differences is mainly related to the differences in the process parameters. By reducing the duty cycle, the sizes of the crystallites are reduced, and coating with a fine structure is formed on the substrate [17,27,28]. As the size of the crystallites decreases, the density of the grain boundary increases and, as a result, the paths prone to diffusion increase [17,27,28]. Consequently, diffusion facilitates and happens easier during heat treatment of the specimen which is electroplated in a lower duty cycle. As a result, a thin layer of about 300 nm consisting of intermetallic compounds was formed at the interface of PH1. The EDS results of this layer show that in addition to the nickel and aluminum substrates, magnesium from the substrate, zinc, and sulfur from the zincate layer and oxygen are also present in the EDS analysis. The high input of substrate elements in the EDS result results from the low thickness of the coating. Therefore, to accurately investigate this phase, the XRD test is required.

XRD patterns of the coated specimens before and after heat treatments are given in Figure 5. The main peak for nickel plated specimens (P1 & P2) in the range of 45 to 46 degrees appears to be a little bit broadened that could be an indication of some degrees of amorphism in the coating structure. Numerous studies have suggested that in electroplating and electroless plating, nickel coatings might be amorphous or semi-amorphous [29]. When the plating process is applied at more or less high speeds, the formation of coating in an amorphous manner is possible. Random placement of nickel atoms on the surface of the substrate deprives them of the opportunity to crystallize, and the atoms take a shorter order of domain [30,31]. Nevertheless, when the duty cycle increases, the intensity of the crystalline nickel peak in (111) increases. Similar results were reported by Borkar et al. [32].

After heat treatment, the amorphicity of the coating was entirely vanished and the coating turned to become crystalized. XRD pattern of the PH1 specimen indicates that the Al_3Ni intermetallic compound has been formed in the coating (Figure 5). This peak corresponds to the thin layer identified in the coating-sublayer interface in Figure 4-A. Since the coating was formed with a much smaller grain size in the lower duty cycles, the density of grain boundaries in this case was higher than that in the specimen coated with a higher duty cycle. The grain boundaries are highly suitable pathways for diffusion that is activated at high temperatures with sufficient time. Therefore, diffusion via grain boundaries leads to the formation of a thin Al_3Ni intermetallic layer.

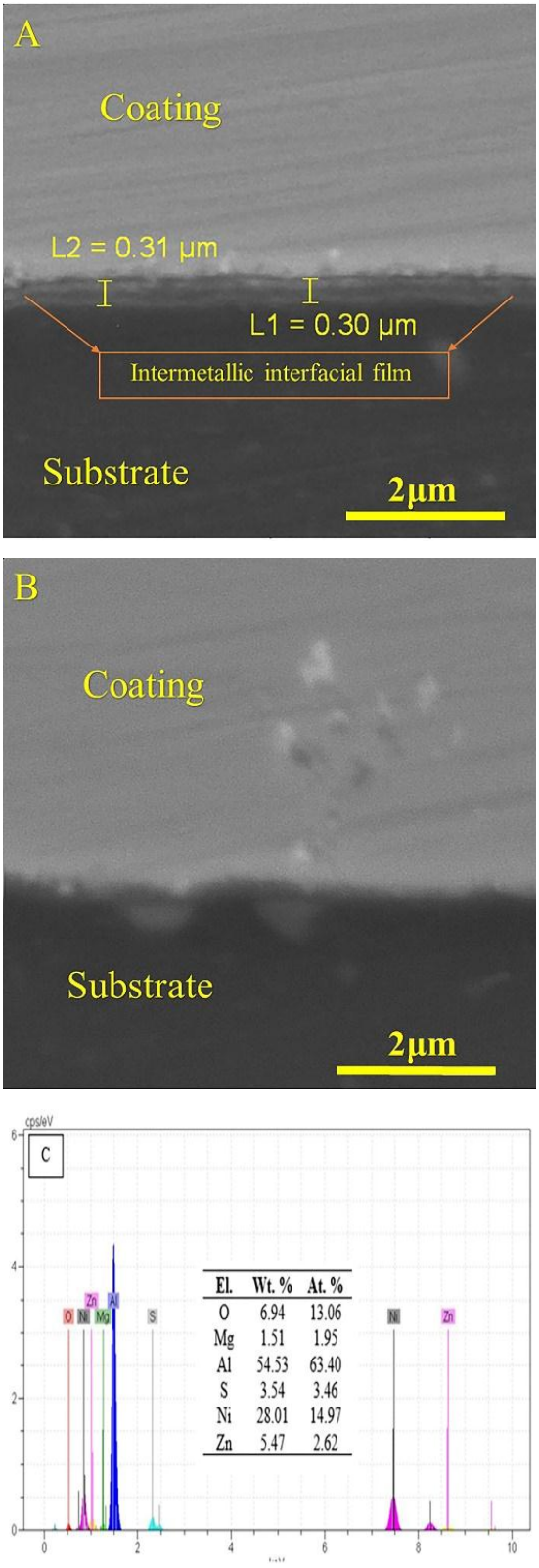

Figure 4. Cross-sectional SEM images of A) PH1, B) PH2, and C) EDS analysis of PH1 near the interface

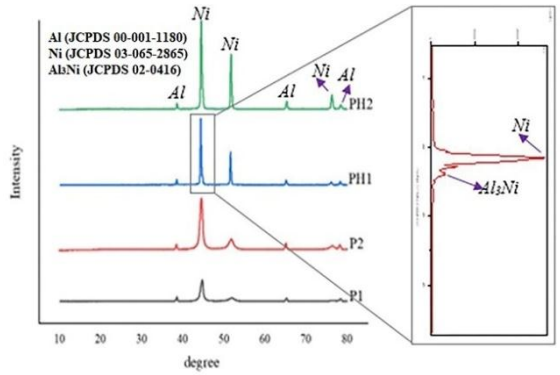

Figure 5. XRD patterns of the electrodeposited nickel before (P1 & P2) and after heat treatment PH1 & PH2)

Figure 6 shows the polarization curves achieved from corrosion tests of the specimens. These results show that the corrosion current density of the coating achieved at higher duty cycle and higher frequency is slightly higher than the one obtained in the lower duty cycle and frequency by around 10 %. In other words, corrosion resistance is slightly reduced when the duty cycle and frequency are doubled. These results also show that heat treatment adversely affects the corrosion resistance of the specimens. This might be related to the amorphicity of the electrodeposited nickel which disappears by heat treatment [33]. As shown in Figure 6, the PH1 specimen has higher corrosion resistance than the PH2 specimen. This might be due to the formation of Al_3Ni thin film that could create a new barrier against the corrosive agent. Previous researches have also shown that Al_3Ni intermetallic compound has high corrosion resistance [34].

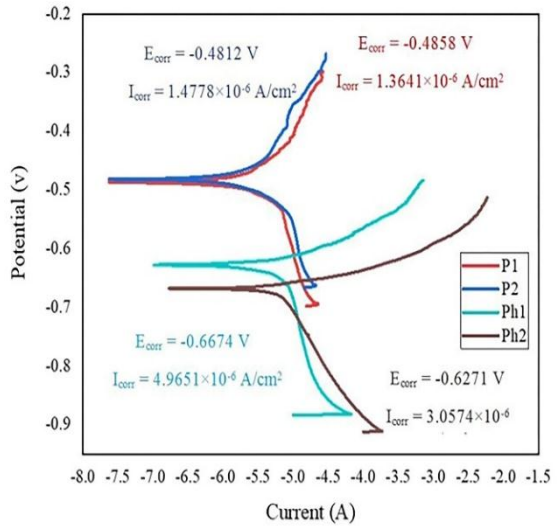

Figure 6. Polarization curves of the electrodeposited nickel before (P1 & P2) and after heat treatment PH1 & PH2)

4. CONCLUSIONS

1- Increase in the frequency and duty cycle resulted in the thickening of the nickel coating achieved from pulsed electrodeposition.
2- Heat treatment improved the crystallinity of the nickel coating.
3- Heat treatment of the nickel coated specimen achieved in the duty cycle of 25 % and frequency of 50 Hz resulted in the formation of thin Al_3Ni intermetallic layer at the interface of the coating and substrate.
4- After heat treatment, the corrosion resistance of the coating deteriorated. Among the heat-treated specimens, the one with the intermetallic compounds at its interface exhibited better corrosion resistance than the specimen without the intermetallic compounds.

5. ACKNOWLEDGMENTS

The authors thank Mr. Yazdan Shajari for his invaluable suggestions during experimental design.

REFERENCES

1. Davis, J. R., Ed., ***Aluminum and Aluminum Alloys, Alloying: Understanding the Basics***, ASM International, (2001), 351-416. https://doi.org/10.31399/asm.tb.aub.t61170351
2. Dorward, R. C., Pritchett, T. R., "Adanced aluminium alloys for aircraft and aerospace applications", ***Materials & Design***, Vol. 9, No. 2, (1988), 63-69. https://doi.org/10.1016/0261-3069(88)90076-3
3. Thompson, G. E., Habazaki, H., Shimizu, K., Sakairi, M., Skeldon, P., Zhou, X., Wood, G. C., "Anodizing of aluminium alloys", ***Aircraft Engineering and Aerospace Technology***, Vol. 71, No. 3, (1999), 228-238. https://doi.org/10.1108/00022669910270709
4. Rashidi, A. M., Amadeh, A., "Effect of Electroplating Parameters on Microstructure of Nanocrystalline Nickel Coatings", ***Journal of Materials Science & Technology***", Vol. 26, No. 1, (2010), 82-86. https://doi.org/10.1016/s1005-0302(10)60013-8
5. Naeem, M., Díaz-Guillén, J. C., Akram, M., Iqbal, J., Naz, M. Y., Shafiq, M., "Novel Active Screen Plasma Nitriding Of Aluminum Using Aluminum Cathodic CAGE", ***Surface Review and Letters***, Vol. 27, No. 09, (2020), 1950205. https://doi.org/10.1142/s0218625x19502056
6. Figueroa, R., Abreu, C. M., Cristóbal, M. J., Pena, G., "Effect of nitrogen and molybdenum ion implantation in the tribological behavior of AA7075 aluminum alloy", ***Wear***, Vol. 276, (2012), 53-60. https://doi.org/10.1016/j.wear.2011.12.005
7. Li, Y., Zhaob, J., Zenga, G., Guana, C., He, X., "Ni/Ni_3Al microlaminate composite produced by EB-PVD and themechanical properties", ***Materials Letters***, Vol. 58, No. 10, (2004), 1629–1633. https://doi.org/10.1016/j.matlet.2003.09.052
8. Rezaei, M., Jeshvaghani, R. A., Shahverdi, H. R., Mojaver, R., Torkamany, M. J., "Formation of Ni-rich aluminide layers on an A356 aluminum alloy by a combined electroplating/laser alloying treatment: Microstructure and tribological characteristics", ***Journal of Manufacturing Processes***, Vol. 29, (2017), 310-319. https://doi.org/10.1016/j.jmapro.2017.07.028

9. Naeimianm, H., Mofid, M. A., "TLP bonding of Ti−6Al−4V to Al 2024 using thermal spray Babbitt alloy interlayer", ***Transactions of Nonferrous Metals Society of China***, Vol. 30, No. 5, (2020), 1267-1276. https://doi.org/10.1016/s1003-6326(20)65294-3
10. Heydarzadeh Sohi, M., Ansari, M., Ghazizadeh, M., Zebardast, H., "Liquid phase surface nitriding of aluminium using TIG process", ***Surface Engineering***, Vol. 31, No. 8, (2015), 598-604. https://doi.org/10.1179/1743294414y.0000000372
11. Carvalho, A. L. M.,Voorwald, H. J. C., "Influence of shot peening and hard chromium electroplating on the fatigue strength of 7050-T7451 aluminum alloy", ***International Journal of Fatigue***, Vol. 29, No. 7, (2007), 1282-1291. https://doi.org/10.1016/j.ijfatigue.2006.10.003
12. Taye, D., Mohanty, S., Das, A. K., Singh, K. N., "Electroless Ni–Al_2O_3–WS_2 Composite Coating on Aluminum Substrate", ***Transactions of the Indian Institute of Metals***, Vol. 72, No. 9, (2019), 2281-2292. https://doi.org/10.1007/s12666-019-01677-1
13. He, L., Tan, Y., Wang, X., Xu, T., Hong, X., "Microstructure and wear properties of Al_2O_3-CeO_2/Ni-base alloy composite coatings on aluminum alloys by plasma spray", ***Applied Surface Science***, Vol. 314, (2014), 760-767. https://doi.org/10.1016/j.apsusc.2014.07.047
14. Hughes, A. E., Parvizi, R., Forsyth, M., "Microstructure and corrosion of AA2024", ***Corrosion Reviews***, Vol. 33, No. 1-2, (2015), 1-30. https://doi.org/10.1515/corrrev-2014-0039
15. Jung, J., Oak, J., Kim, Y. H., Cho, Y. J., Park, Y. H., "Wear behaviors of pure aluminum and extruded aluminum alloy (AA2024-T4) under variable vertical loads and linear speeds", ***Metals and Materials International***, Vol. 23, No. 6, (2017), 1097-1105. https://doi.org/10.1007/s12540-017-7158-y
16. Bahri, H., Danaee, I., Rashed, G. R., Dabiri, A. R., "Scratch and wear resistance of nano-silica-modified silicate conversion coating on aluminium", ***Materials Science and Technology***, Vol. 32, No. 13, (2016), 1346-1353. https://doi.org/10.1080/02670836.2015.1124192
17. Adabi, M., Amadeh, A. A., "Formation mechanisms of Ni–Al intermetallics during heat treatment of Ni coating on 6061 Al substrate", ***Transactions of Nonferrous Metals Society of China***, Vol. 25, No. 12, (2015) 3959-3966. https://doi.org/10.1016/s1003-6326(15)64073-0
18. Li, C., Yuan, Z., Guo, R., Xuan, W., Ren, Z., Zhong, Y., Li, X., Wang, H., Wang, Q., "Reaction diffusion in Ni–Al diffusion couples in steady magnetic fields", ***Journal of Alloys and Compounds***, Vol. 641, (2015), 7-13. https://doi.org/10.1016/j.jallcom.2015.04.061
19. Prasad, D. S., Ebenezer, N. S., Shoba, C., Raju, P., Rao, P. S., "The Effect of T6 Heat Treatment on Corrosion Behavior of Nickel Electroplated Metal Matrix Composites", ***Silicon***, Vol. 11, No. 4, (2019), 2025–2032. https://doi.org/10.1007/s12633-018-0023-x
20. Goli, F., Jamaati, R., "Effect of strain path during cold rolling on the microstructure, texture, and mechanical properties of AA2024 aluminum alloy", ***Materials Research Express***, Vol. 6, No. 6, (2019), 066514. https://doi.org/10.1088/2053-1591/ab0a1f
21. Ghorbanzade, T., Soltanipour, A., Dehghani, K., Chabok, A., "Microstructural evolutions and mechanical properties of friction stir welded AA2024-3", ***Proceedings of the Institution of Mechanical Engineers, Part L: Journal of Materials: Design and Applications***, Vol. 230, No. 1, (2014), 75-87. https://doi.org/10.1177/1464420714545369
22. Hanachi, M., Seyedraoufi, Z. S., Abouei, V., "Investigation of Microstructure, Hardness, and Corrosion Resistance of Ni-P-GO Electroless Nanocomposite Coating on AZ31D Alloy Surface", ***Advanced Ceramics Progress***, Vol. 6, No. 3, (2020), 55-62. https://doi.org/10.30501/ACP.2020.233518.1038
23. Lajevardi, S. A., Shahrabi, T., "Effects of pulse electrodeposition parameters on the properties of Ni–TiO_2 nanocomposite coatings", ***Applied Surface Science***, Vol. 256, No. 22, (2010), 6775-6781. https://doi.org/10.1016/j.apsusc.2010.04.088
24. Kumar, K. A, Kalaignan, G. P., Muralidharan, V. S., "Direct and pulse frequency electrodeposition of Ni–W–TiO_2 nanocomposite coatings", ***Ceramics Internatinal***, Vol. 39, No. 3, (2013), 2827-2834. https://doi.org/10.1016/j.ceramint.2012.09.054
25. Seyedraoufi, Z. S., Mirdamadi, S., "Effects of pulse electrodeposition parameters and alkali treatment on the properties of nano hydroxyapatite coating on porous Mg–Zn scaffold for bone tissue engineering application", ***Materials Chemistry and Physics***, Vol. 148, No. 3, (2014), 519-527. https://doi.org/10.1016/j.matchemphys.2014.06.067
26. Moradi, E. H., Jafarzadeh, K., Borji, S., Abbaszadeh, H., "Pulse electrodeposition as a new approach in electrowinning of high purity cobalt from WC–Co scraps. Part I: The effect of frequency and duty cycle", ***Minerals Engineering***, Vol. 77, (2015), 10-16. https://doi.org/10.1016/j.mineng.2015.02.012
27. Adabi, M., Amadeh, A. A., "Electrodeposition mechanism of Ni–Al composite coating", ***Transactions of Nonferrous Metals Society of China***, Vol. 24, No. 10, (2014), 3189-3195. https://doi.org/10.1016/s1003-6326(14)63459-2
28. Adabi, M., Amadeh, A., "Effect of electrodeposition conditions on properties of Ni–Al composite coatings", ***Surface Engineering***, Vol. 31, No. 9, (2015) 650-658. https://doi.org/10.1179/1743294414y.0000000449
29. Zhang, P., Lv, Z., Liu, X., Xie, G., Zhang, B., "Electroless nickel plating on alumina ceramic activated by metallic nickel as electrocatalyst for oxygen evolution reaction", ***Catalysis Communications***, Vol. 149, (2021), 106238. https://doi.org/10.1016/j.catcom.2020.106238
30. Li, H., He, Y., Fan, Y., Xu, W., Yang, Q., "Pulse electrodeposition and corrosion behavior of Ni–W/MWCNT nanocomposite coatings", ***RSC Advances***, Vol. 5, No. 84, (2015), 68890-68899. https://doi.org/10.1039/c5ra09462c
31. Atarchi, M., Sadrnezhad, S., "Pulse reverse electrodeposition of spherical Ni-MWCNT composite skein", ***International Journal of Engineering, Transactions B: Applications***, Vol. 22, No. 2, (2009), 161-168. https://www.ije.ir/article_71780.html
32. Borkar, T., Harimkar, S. P., "Effect of electrodeposition conditions and reinforcement content on microstructure and tribological properties of nickel composite coatings", ***Surface and Coatings Technology***, Vol. 205, No. 17-18, (2011), 4124–4134. https://doi.org/10.1016/j.surfcoat.2011.02.057
33. Shajari, Y., Porhonar, M., Seyedraoufi, Z. S., Razavi, S. H., Baghdadabad, D. M., Yousefnia, H., Farahani, M., "Improvement of the NiBrAl Casting Alloy Surface Properties by Electroless Ni-B Plating for Dynamic Marine Applications", ***Physical Mesomechanics***, Vol. 23, No. 1, (2020), 81-88. https://doi.org/10.1134/s1029959920010087
34. Mohammed, A., Yaro, S. A., Abdulwahab, M., "Influence of Ni additions and age-hardening treatment on the corrosion resistance of Al-Cu-Si alloy", ***Journal of Materials and Environmental Science***, Vol. 7, No. 5, (2016), 1549-1555. https://www.jmaterenvironsci.com/Document/vol7/vol7_N5/170-JMES-948-Mohammed.pdf

AIMS AND SCOPE

Advanced Ceramics Progress (ACERP) as an ISC international journal is devoted to elucidating the fundamental aspects of chemistry and physics occurring at a wide range of oxide and nonoxide ceramics and composite materials and their processing, microstructure, properties, and applications. The journal provides a unique venue for publishing new exciting research, focusing on dynamic growth areas in this field.

INSTRUCTIONS FOR AUTHORS

Submission of manuscript represents that it has neither been published nor submitted for publication elsewhere and is result of research carried out by author(s).
Authors are required to include a list describing all the symbols and abbreviations in the manuscript. Use of the international system of measurement units is mandatory.

- On-line submission of manuscripts results in faster publication process and is recommended. Instructions are given in the ACERP web site: www.acerp.ir
- References should be numbered in brackets and appear in sequence through the text. List of references should be given at the end of the manuscript.
- Figures' captions are to be indicated under the illustrations. They should sufficiently explain the figures.
- Illustrations should appear in their appropriate places in the text.
- Tables and diagrams should be submitted in a form suitable for reproduction.
- Photographs and figures should be of high quality saved as jpg files (resolution > 600 dpi).
- Tables, illustrations, figures and diagrams will be normally printed in single column width (8 cm). Exceptionally large ones may be printed across two columns (17 cm).

PAGE CHARGES AND REPRINTS

ACERP subscribers do not need to make any payment for publication and reprints.

AUTHORS CHECKLIST

- Author(s), bio-data including affiliation(s) and mail and e-mail addresses.
- Manuscript including abstract, key words, illustrations, tables, figures with figures' captions, and list of references.
- MS Word files of the manuscript in the ACERP template.
- Similarity check of the manuscript, copyright forms, and conflict of interest forms

Advanced **Cer**amics **P**rogress,
P.O. Box 31787-316, Karaj, Alborz, I. R. Iran
Materials and Energy Research Center, Imam Khomeini Blvd, Meshkin Dasht, Karaj, Alborz, I. R. Iran
P.O. Box 14155-4777, Tehran, I. R. Iran
No. 5, Ahuramazda St., Alvand Ave., Argentine Sq., Tehran, I. R. Iran

www.merc.ac.ir - www.icers.ir

Advanced Ceramics Progress

Volume 7, Number 1, Winter 2021

CONTENTS

P. Kameli **H. Vaezi** **M. H. Ehsani** **Bagher Aslibeiki** **H. Salamati**	Structual, Magnetic, and Transport Properties of $LaMn_{1-x}Cu_xO_3$ (x= 0-0.125) Ceramics	1-10
B. Chameh **M. Moradi Alborzi** **S. Hajati** **F. Alikhani Hessari** **M. A. Kiani**	Synthesis and Characterization of Palladium Impregnated MIL-53(Fe) as Cathode Material of Supercapacitor	11-17
S. Hamidi **M. R. Rahimipour** **M. J. Eshraghi** **H. Esfahani**	Optimization of Heat Treatment Cycles in Sub-atmospheric LiF-NaF-KF Based Fluoride Ion Cleaning for Removing Oxide Layers in Cracks of IN738-LC	18-24
S. Manafi **A. Azizi**	Experimental and Numerical Evaluation of Diffusion Welding of 7075 Aluminum and AZ31 Magnesium Alloys	25-34
J. Arasteh	Microhardness Optimization of Al–TiC Nanocomposite Produced by Mechanical Milling and Heat Treatment	35-45
A. Khiabani **Z. S. Seyedraoufi** **M. Heydarzadeh Sohi**	Heat Treatment of Pulsed Electroplated Nickel Deposited on AA2024 Aluminum	46-51

Journal Home Page: www.acerp.ir